

**Development of an Acoustic Array for Wind
Turbine Aeroacoustic Noise Analysis**

by

Eric J. Simley

B.S. Electrical and Computer Engineering, University of Colorado,

2010

A thesis submitted to the

Faculty of the Graduate School of the

University of Colorado in partial fulfillment

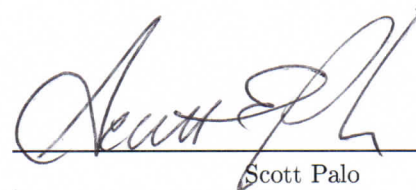
of the requirements for the degree of

Master of Science

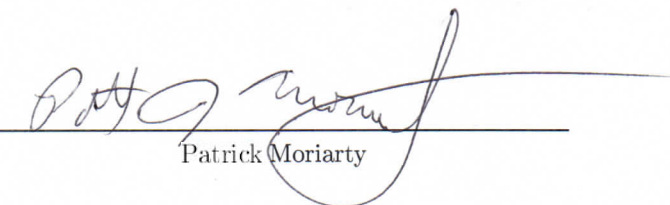
Department of Electrical, Computer, and Energy Engineering

2010

This thesis entitled:
Development of an Acoustic Array for Wind Turbine Aeroacoustic Noise Analysis
written by Eric Simley
has been approved for the Department of Electrical, Computer, and Energy Engineering



Scott Palo



Patrick Moriarty

Date 22-APR-10

The final copy of this thesis has been examined by the signatories, and we find that both the content and the form meet acceptable presentation standards of scholarly work in the above mentioned discipline.

Simley, Eric J. (M.S., Electrical Engineering)

Development of an Acoustic Array for Wind Turbine Aeroacoustic Noise Analysis

Thesis directed by Professor Scott Palo

As wind continues to become a more prevalent source of energy, concerns over the proximity of wind turbines to residential areas will grow. Densely populated Europe has already encountered this problem and the United States is beginning to experience it. One of the main concerns about wind farms is the radiation of acoustic noise. Although some noise is caused by the gearbox and generator, it is the wind turbine blades that produce the strongest sources of noise on modern turbines. To aid in the design of quieter wind turbine blades, diagnostic tools are required to assess the components of wind turbine noise during operation in the field. Single microphone techniques have been employed in the past, but they are unable to distinguish between the potentially large number of sources of noise. Furthermore, very low signal-to-noise ratios can result from single microphones due to wind noise. An array of microphones can be used to provide a high resolution, high signal-to-noise ratio diagnostic tool. Acoustic arrays have been used for decades in the analysis of aeroacoustic noise, mainly on aircraft. Recently, acoustic arrays have been applied to the study of wind turbine noise. This thesis describes research performed on the design of a 32-microphone acoustic array for wind turbine noise analysis. The work is a cooperation between the National Renewable Energy Laboratory (NREL) and the University of Colorado. The array has been successfully tested on a 100 kW wind turbine at NREL in Boulder, Colorado and was used to analyze acoustic noise generated from the blades of a 100 kW turbine in Bushland, Texas in cooperation with Sandia National Laboratories during 2009 and 2010.

Dedication

To my parents, for their encouragement and support throughout my education.

Acknowledgements

This thesis and the research achievements described in it would not have happened without the help of so many people. First, I would like to extend my gratitude to Dr. Scott Palo and Dr. Pat Moriarty for making this research project a reality. I am indebted to my adviser, Professor Palo, not only for the essential technical guidance he provided throughout the project, but also for everything he has taught me about the engineering process and how to conduct a successful research project. Dr. Moriarty's interest in pursuing aeroacoustics research at the National Renewable Energy Laboratory is the reason this project ever occurred at all. His guidance and assistance were paramount to the success of the research and I thank him for all of the time he devoted to making this work possible.

Countless individuals at the National Wind Technology Center assisted me in conducting field experiments and enabled me to perform my research. I thank all of them for their help. In particular, I would like to thank Arlinda Huskey for offering her expertise in acoustics.

I am grateful to Dr. Matt Barone, Josh Paquette, and Wesley Johnson at Sandia National Laboratories for all of their effort working with us on our collaborative field measurement campaign. Dr. Barone's knowledge of aeroacoustics has been a very valuable asset. I thank Wesley Johnson for all of the work he has put into maintaining our array hardware. Adam Holman and Byron Neal, at the Agricultural Research Service, deserve special mention for working closely with me (in a different time zone) to maintain the array and see that we are able to acquire the data we need to make this a successful project.

I am very lucky to have had the insight of two of the world's leading experts in acoustic

arrays, Dr. Stefan Oerlemans and Dr. Robert Dougherty. I have been very enlightened through email correspondence with them.

I would also like to thank Professor Filipovic for serving on my thesis committee.

Contents

Chapter

1	Introduction	1
1.1	Background	4
1.1.1	Wind Turbine Noise	11
2	Array Signal Processing Theory	17
2.1	Delay-and-Sum Beamforming	19
2.1.1	Array Pattern	21
2.2	Frequency Domain Beamforming	23
2.2.1	Linearity of the Conventional Beamformer	25
2.2.2	Beamforming with General Sources	26
2.3	Array Shape Theory	27
2.3.1	Spatial Resolution	31
2.3.2	The Co-Array	33
2.4	Advanced Beamforming Techniques	37
2.4.1	Diagonal Elimination	37
2.4.2	Robust Adaptive Beamforming	38
2.4.3	MUSIC	41
3	Practical Acoustic Array Considerations	46
3.1	Characterization of Corruptive Noise	46

3.1.1	Wind Noise and Array Gain	48
3.1.2	Correlation of Wind Noise	50
3.1.3	The Effect of Atmospheric Turbulence on Signal Estimation	53
3.2	Uncertainty in Beamformer Parameters	61
3.2.1	Sensor Position Uncertainties	61
3.2.2	Uncertainties in y -direction Distance from Array to Source	68
3.2.3	Uncertainty in Source Wavelength	71
3.2.4	Wind Shear Effects	77
3.3	The Effects of Doppler Shifts Due to a Rotating Source	78
3.3.1	A Complete Doppler Error Correction Technique	82
3.3.2	Doppler Error Mitigation by Time Delaying the Data	85
3.3.3	A Doppler Correction Example	87
4	Array Hardware	89
4.1	Microphone Sensors	89
4.2	Microphone Signal Conditioners	91
4.3	Data Acquisition System	92
4.4	Sensor and Signal Conditioner Characteristics	93
4.5	Field Hardware	95
5	Field Experiments	101
5.1	National Wind Technology Center Prototype Array	102
5.1.1	Array Design	102
5.1.2	Field Validation	103
5.2	Bushland, Texas Array	109
5.2.1	Array Design	109
5.2.2	Field Validation	118
5.2.3	Field Testing and Results	121

6 Conclusions and Future Work	131
-------------------------------	-----

Bibliography	136
--------------	-----

Appendix

A MATLAB Code	141
---------------	-----

B Array Sensor Locations	148
--------------------------	-----

List of Tables

Table

3.1	95th Percentile of Beamformer Errors	69
4.1	List of Microphone Sensor Components	99
4.2	List of Array Hardware Components	100

List of Figures

Figure

1.1 A Spherical Reflector Directional Microphone used by Laufer et. al. in 1976 [10]	6
1.2 An End-fire Array Example Showing the Reception Pattern Ambiguity	7
1.3 The Acoustic Telescope Developed by Billingsley and Kinns [12]	8
1.4 Spectrum of A-Weighting Filter	12
2.1 Scan Plane, Array Location, and Coordinate System	18
2.2 Beamforming Output or “Noise Map”	20
2.3 Projection of 250Hz Wave from Scan Plane Center onto Array Plane	29
2.4 X and Y Components of Wavenumber for a 250 Hz Source at Scan Plane Center Projected onto Array Plane	29
2.5 X and Y Components of Wavenumber for a 1 kHz Source Projected onto Array Plane as a Function of Scan Plane Position	31
2.6 Rate of Change of Projected Wavenumbers as a Function of Array Distance from Tower	32
2.7 13 and 14 Sensor Similar Array Shapes	35
2.8 Co-Array Patterns for the 13 and 14 Sensor Array Shapes	36
2.9 Noise maps for the 13 and 14 Sensor Elliptical Arrays	36
2.10 Comparison of Beamforming With and Without the Diagonal	39
2.11 Robust Adaptive Beamforming Examples	41
2.12 MUSIC Example	44

3.1	Acoustic Transmission Model	47
3.2	Wind Noise Spectrum	48
3.3	Histograms of Inter Sensor Phase Differences for Wind Noise	52
3.4	Histograms of Variations in Time-Adjacent Inter-Sensor Phase Differences	52
3.5	Comparison of 732 Samples of 1kHz Wind Noise Magnitude over 60 Seconds with Rayleigh Probability Density Function	53
3.6	Cross Spectral Power Distortion Example	55
3.7	Phase Distortion Example	56
3.8	Phase Statistics as a Function of Inter-sensor Distance	58
3.9	Cross Power Statistics as a Function of Inter-sensor Distance	60
3.10	Sensor Position Error	62
3.11	Beamformer Power Error Statistics as a Function of Sensor Position Errors (Fixed Distance Error)	65
3.12	Beamformer Power Error Statistics as a Function of Sensor Position Errors (Uniformly Distributed Error)	66
3.13	Beamformer Power Error Statistics as a Function of Sensor Position Errors (Gaussian Error)	66
3.14	Beam Position Error Statistics as a Function of Sensor Position Errors (Fixed Distance Error)	66
3.15	Beam Position Error Statistics as a Function of Sensor Position Errors (Uniformly Distributed Error)	67
3.16	Beam Position Error Statistics as a Function of Sensor Position Errors (Gaussian Error)	67
3.17	The Angles Describing Rotor Position	68
3.18	Y-Error Impact on Beamforming	70
3.19	Z-Offsets of Received Source Due to Scan Plane Y-Distance Errors	71
3.20	Magnitude of Unfocused Beamforming Errors	72

3.21 Sidelobe Rejection Due to Unfocused Beamforming	72
3.22 Beamforming Geometry in the yz -Plane	74
3.23 The Effects of Beamforming with Errors in the λ Estimate	76
3.24 Received Source Power Degradation Due to Errors in the λ Estimate	76
3.25 Sidelobe Rejection Due to Errors in the λ Estimate	77
3.26 Wind Shear for an 11 m/s Hub Height Wind Speed	79
3.27 The Effects of Sensor-Dependent Doppler Shifts on Inter-Sensor Phase Differences	84
3.28 Doppler Induced Phase Errors When Data Is Time-Domain Steered to 80% Along the Blade	86
3.29 Doppler Correction Improvements	88
4.1 Array Hardware Flowchart	90
4.2 Signal Conditioning Circuit [2]	92
4.3 Frequency Response of the System without the Microphone	94
4.4 Field Microphone Frequency Response Calibration	95
4.5 Microphone/Signal Conditioner Box [2]	96
4.6 Data Acquisition and Power Supply Enclosure	98
4.7 Array as Deployed in Bushland, TX	98
5.1 32-Sensor Prototype Array Shape	104
5.2 Small Sub-Array Pattern, 3 kHz Tone	105
5.3 Mid Sub-Array Pattern, 1 kHz Tone	106
5.4 Large Sub-Array Pattern, 250 Hz Tone	107
5.5 Large Sub-Array Pattern, 500 Hz Tone	108
5.6 Low SNR, White Gaussian Noise 3 kHz Array Patterns	110
5.7 Projected Spatial Frequencies from 1kHz Source on Scan Plane of Bushland Array	112
5.8 Fourier Transforms of Mid Sub-Array	113
5.9 Final Array Pattern for Mid Sub-Array	115

5.10 Array Shape Configurations	116
5.11 Array Pattern of 26 Sensor Mid Sub-Array	117
5.12 Simulation of Noise Maps Produced by Monotone Sources Located at Hub	119
5.13 Small Sub-Array Patterns, 4 kHz and 7.615 kHz Tones	120
5.14 Mid Sub-Array Patterns, 1 kHz and 2 kHz Tones	122
5.15 Large Sub-Array Patterns, 250 Hz and 500 Hz Tones	123
5.16 45 Second Average Noise Maps, Mid and Large Sub-Arrays	123
5.17 Dependence on Rotor Azimuth Angle, 250 Hz 1/3-Octave Band, 60 Second Avg. .	125
5.18 Rotating Scan Plane, 1.25 kHz 1/3-Octave Band, 56 Second Avg. of All Blades .	125
5.19 Peak Noise Positions, 1.25 kHz 1/3-Octave Band, 56 Second Avg. of Individual Blades	126
5.20 150 degree Azimuth Angle Tip Region Spectrum, Mid Sub-Array	127
5.21 A Comparison of Conventional Beamforming (left) and MUSIC (right) Applied to a Poor Resolution Scenario	130
5.22 Application of Robust Adaptive Beamforming to Poor Resolution Scenario	130

Chapter 1

Introduction

As wind power becomes a larger source of the world's electricity, the close proximity of wind turbines to residential areas will continue to be a major issue due to problems with visual impact and acoustic noise. The close proximity of wind turbines to residential areas is a reality in densely populated Europe and near coastal regions where wind resources are high. Thus as wind energy continues to grow, there will inevitably be concerns over how close to populated areas wind turbines can be placed. While it is difficult to define regulations on visual impact, it is easy to place a limit on the sound levels to which populated areas can be exposed. In fact, there are laws defining the acceptable sound pressure level (SPL) for most areas. Also, while it is impossible to correct for the visual impact of a wind turbine, it is possible to reduce the noise generated by one.

Wind turbine noise can be divided into nacelle noise and aeroacoustic noise. Nacelle noise includes the mechanical noise produced by the drivetrain, gearbox, and generator of the wind turbine. As these noise sources have lessened, because of design improvements, aeroacoustic noise has emerged as the dominant contribution to overall noise levels. Aeroacoustic noise is the result of the interaction between the wind turbine rotor and the local flow field. The power of aeroacoustic sources near the blade tip is a function of the speed at which the tip is travelling, scaling with the fifth power of rotation speed [1]. Tip speed also greatly influences the amount of power that the turbine can generate. If a rotor is allowed to spin faster, more energy can be extracted from the wind. With noise regulations governing the sound levels that a wind turbine

can emit, a wind turbine operator may have to reduce the rotation rate of the turbine from its optimal value, thereby reducing the generated power and increasing the cost of energy.

The measurement of aeroacoustic noise sources on wind turbine blades, both in wind tunnels and during operation in the field, is essential to understanding a solution to the noise emission problem. In order to improve the acoustic properties of a blade, it is vital to understand not only the overall sound level and spectrum, but where the sources of noise are located. Single microphone measurements can provide information about the overall SPL of the noise, but not how much is due to aeroacoustic sources or the locations of those sources.

To provide information about the spatial location of the acoustic sources located on a wind turbine, a highly directional microphone must be used, with the ability to be steered toward different locations on the turbine. It is possible to mechanically orient a highly directional microphone toward different locations, but a much better solution is to use an acoustic array. An acoustic array is an array of microphones that are positioned spatially in such a way that the individual received signals can be combined to determine the direction from which acoustic sources are propagating. The time delays between when acoustic signals reach the microphones are used to determine the direction from which they are propagating. An acoustic array therefore not only has the advantage of being able to locate the position of acoustic sources, but also requires no mechanical movement. An array can also image the entire wind turbine rotor simultaneously while a narrow beam microphone that is scanning the rotor cannot. Once the microphone data are collected, the array can be steered toward any direction through post-processing on a computer.

In response to the growing concern over wind turbine aeroacoustic noise, the National Renewable Energy Laboratory (NREL), in cooperation with the University of Colorado, has developed an acoustic array system specifically designed to locate broadband noise sources on a wind turbine rotor. The array consists of 32 microphones, providing a low cost solution to the analysis of wind turbine noise.

The research described in this thesis was conducted between May 2008 and December

2009 and is a continuation of work conducted between August 2006 and August 2007. The NREL-CU acoustic array project began as a mechanical engineering senior design project in cooperation with NREL during the 2006-2007 academic year [2]. During this phase, a 32-microphone, 12-by-16 foot array was designed and built and a suite of beamforming software was written. The hardware and software components of the system were successfully integrated, but satisfactory field tests were never achieved. A team of two undergraduate interns continued working on the project during summer 2007 [3]. This team found faults in the existing data acquisition (DAQ) system and purchased an improved system for use with the acoustic array. Errors in the original beamforming software were discovered and corrected and simulations of array performance for different array shapes were conducted. The team also made significant progress in the area of microphone frequency response calibration.

This thesis builds on the work described above and is organized into six chapters. The first chapter presents an introduction to the research goals of the project and a background of acoustic array work and wind turbine aeroacoustics. The second chapter presents the underlying mathematical theory behind array signal processing and beamforming. The third chapter discusses the imperfections that are encountered when using an acoustic array in the field. Topics such as unwanted wind noise and atmospheric distortion of signals are discussed. The effects of beamformer uncertainties such as microphone position and speed of sound uncertainties are examined. Finally, an investigation into the consequences of using an array to locate a moving source, producing Doppler shifted signals, is made. The fourth chapter explains the hardware used in the array. The fifth chapter presents the design of the two arrays used for field experiments and discusses the results of initial field tests. Interesting results obtained while using the array to examine a wind turbine in Bushland, Texas during summer 2009 are included. The sixth and final chapter concludes the thesis with a discussion of possible future research work involving the array. For reference, some of the MATLAB code used for beamforming is included in the appendix.

1.1 Background

Several types of directional acoustic listening devices have been developed during the last century. The basic premise of all of them is that they improve the omnidirectional pattern of a microphone to a highly directional pattern. In general, the resolution of a receiver is improved when the antenna spans a larger area. An antenna array makes it possible to create an antenna spanning a very large area by using many small antennas instead of a single very large device. The advantages are that many smaller antennas are less expensive than a single very large antenna and that it is often infeasible to construct and install such a large device. Furthermore, a large highly directional antenna must be mechanically steered whereas an array of microphones can be electronically steered, relieving the system of difficult mechanical control. The main disadvantage of using an acoustic array is that data from multiple microphones must be collected, increasing the complexity of the electronics.

Although phased array technology was not fully explored until World War II, a very early example of an acoustic array was used by the French during World War I [4]. The device consisted of two hexagonal arrays of horns separated by a few meters. The horns making up the hexagonal arrays fed together into a tube that the operator listened to, with each ear listening to the contribution from the corresponding array. This device had to be mechanically steered toward the direction of interest and was used to detect approaching enemy aircraft.

The development of radar technology during World War II initiated the field of phased array theory [5]. Most phased array work during World War II was concerned with radars and electromagnetic antennas, but some acoustic array progress was made in the area of sonar. American submarines used a continuous aperture hydrophone that was mechanically steered with a servo mechanism to direct sonar detection in a particular direction [6]. Germany, however, determined a way to successfully steer the beam of an array of hydrophones in their submarines, thereby developing the first true acoustic array that did not require mechanical steering [6]. Although the hydrophones did not physically change position, the beamformer did contain

moving mechanical parts. The beamformer consisted of a plate that was rotated so that wire brushes moved to different positions along delay lines with the sum of the tapped delay lines acting as the received signal. This type of beamformer is called the “delay-and-sum” beamformer [4]. A wheel was turned that would tap the delay lines of each hydrophone to account for signal time delays corresponding to the direction of interest and then the signals were summed together.

In 1946, the American Navy Underwater Sound Laboratory developed a 979-element vacuum tube that was designed to electronically beamform and steer an array of hydrophones [7]. This device enabled the first acoustic array that was steered electronically without moving mechanical parts. During the late 1950’s, the Marine Physical Laboratory in San Diego developed a beamformer that used digital circuitry. The beamformer did not perform very well because the shift registers used to implement it were only 1 bit and the sampled acoustic signals were clipped to represent either a positive value or a negative value. During the 1970’s, advances in digital circuitry allowed digital beamformers to contain multi-bit memories instead of 1 bit shift registers [6]. Analog-to-digital converters made it possible to sample the acoustic signal with a relatively small amount of distortion. Furthermore, digital circuitry allowed for the efficient implementation of the Fast Fourier Transform, or FFT, which enabled a beamformer to select the frequency of interest in addition to the direction of interest.

Beginning in the 1970s, acoustic arrays were used for scientific purposes, largely to locate and help remove strong acoustic sources on aircraft. Most of the work was performed in wind tunnels on scale models of airframes or on jet engines. Interestingly, during the mid 1970’s, there was still not a general consensus that arrays were the ideal tool for locating and measuring acoustic sources. Grosche et al. [8] at DLR in Germany as well as Schlinker [9] at NASA used acoustic mirrors to create highly directional microphone reception patterns in 1976 and 1977 respectively. These devices consisted of a single microphone and a parabolic reflector and were used in wind tunnel tests (see fig. 1.1). Laufer et al. [10] at NASA, in 1976, used a pair of microphones that were positioned so they would receive different amounts of Doppler shift when observing a jet engine. A correlation of the microphone signals was used to determine which

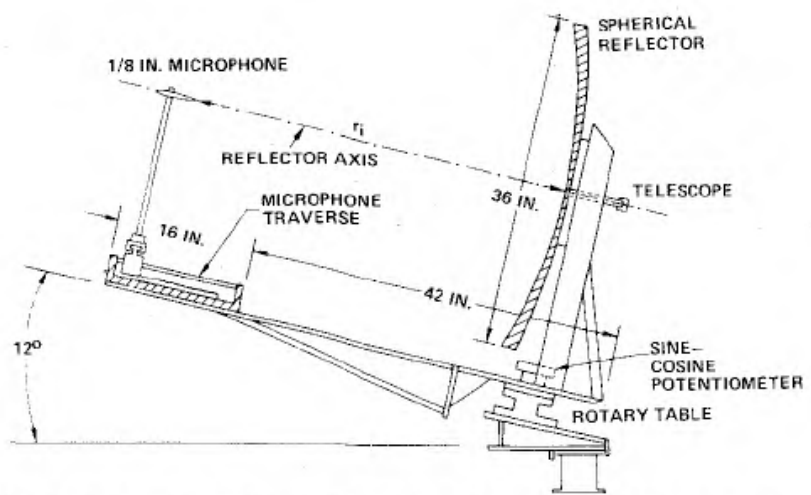


Figure 1.1: A Spherical Reflector Directional Microphone used by Laufer et. al. in 1976 [10]

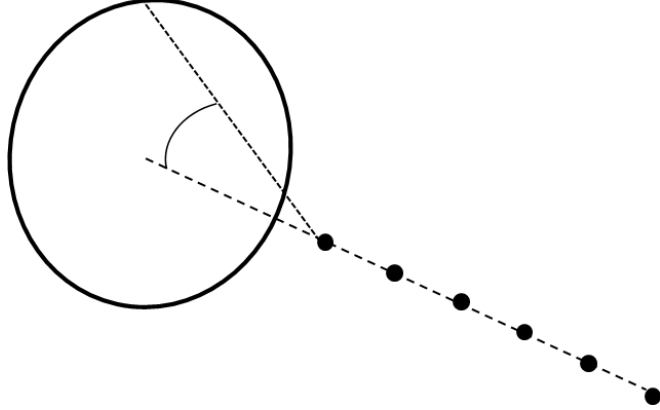


Figure 1.2: An End-fire Array Example Showing the Reception Pattern Ambiguity

location a source was located at given knowledge about the amount of Doppler shift that would be expected at various microphone locations and source positions.

In 1974, Soderman and Noble [11] at NASA Ames used line arrays of microphones to conduct wind tunnel aeroacoustics tests. The arrays were four or eight-element end-fire arrays. An end-fire array is a line array oriented so that the axis containing the microphones is aligned toward the general direction of acoustic interest. Linear arrays of equally spaced sensors were popular because of their simplicity during the early years of aeroacoustics research, but the main disadvantage is that since they are one dimensional, they only have one dimension of selectivity in their reception pattern. An end-fire array is capable of differentiating between different angles off of the end-fire axis, but cannot distinguish which angle around the axis the source is propagating from. Figure 1.2 illustrates the ring of ambiguity in the reception pattern of an end-fire line array.

In 1976, researchers at Cambridge University in England published a landmark paper in acoustic array technology. Billingsley and Kinns [12] developed what they called the “acoustic telescope” to analyze noise sources on the Rolls-Royce/SNECMA Olympus engine for the Concorde aircraft (see fig. 1.3). Their array was yet again a line array, consisting of 14 microphones. The system included the microphones, preamplifiers, analog filters, analog-to-digital converters, and a digital computer along with a color television display to plot the results in real-time.

THE ACOUSTIC TELESCOPE

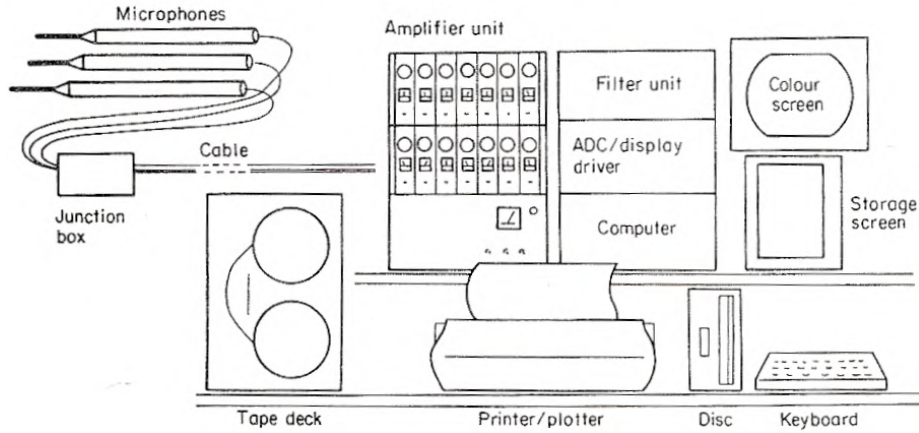


Figure 1.3: The Acoustic Telescope Developed by Billingsley and Kinns [12]

Results could be analyzed by frequency as well as position and the “acoustic telescope” could be easily transported in a vehicle.

Rail noise was another early area of interest for acoustic array applications. DLR used a line array of 15 microphones, oriented either horizontally, in the direction the train is travelling, or vertically, to analyze high speed trains beginning in 1977 [13]. The line array was oriented in the direction of interest for a specific experiment. For example, if researchers wanted to identify the locations of acoustic emissions along the length of the train, then the array was oriented horizontally in the lengthwise direction of the train.

During the 1980’s, activity began in both aircraft flyover testing and helicopter rotor monitoring. Howell et al. [14], at the Institute of Sound and Vibration Research in England, in 1986, used a simple four element line array with 3.8 meter microphone spacing, oriented in the flight direction, to conduct flyover tests of a Lockheed Tristar aircraft. A camera was used to track the aircraft’s position to within 2 meters and the signals were de-Dopplerized before beamforming. Two groups using acoustic arrays published helicopter rotor results in 1987. At NASA Langley, Brooks, Marcoloni, and Pope [15] used a 12 microphone, two-dimensional array to observe the aeroacoustics of a model helicopter. Blacodon, Caplot, and Elias [16], with ONERA in France, used a two-dimensional array to locate sources on a helicopter rotor in a

wind tunnel. These 1987 tests are very important because of their departure from line arrays and their recognition of the benefits of two-dimensional array shapes.

Beginning in the mid 1990's, NASA and Boeing developed sophisticated wind tunnel acoustic array test facilities. NASA Ames [17, 18, 19] and NASA Langley [20, 21, 22] developed two-dimensional arrays with over 40 microphones for wind tunnel tests. Underbrink, Dougherty, and Stoker [23, 24, 25], with The Boeing Company, conducted wind tunnel tests on model aircraft using acoustic arrays and also contributed heavily to the field of acoustic array design and optimization. Researchers at NLR in the Netherlands used a 100-element array to localize noise sources on a model Airbus aircraft in the German Dutch Wind Tunnel (DNW) in 1999 [26]. Ulf Michel [27], a flyover measurement pioneer with DLR, conducted flyover measurements in 1997 and 1998. In 1997, he used a 29-element line array, consisting of several line arrays of different sensor spacings nested together, to observe the acoustics of a Tornado aircraft. Michel [28] later used a 111-element array in 1998 to observe several aircraft landing at the Frankfurt airport. This array was notable because the positions of the microphones were determined by Monte Carlo simulations intended to optimize the sidelobe suppression of the array response.

During the 1990's, researchers knew how to successfully apply arrays to aeroacoustic applications and began developing advanced array signal processing techniques. In 1989, Dougherty [25, 29, 30] created the spiral array shape while working at Boeing. An interesting result in beamforming is that a random array shape tends to produce better sidelobe rejection and sensors placed along a spiral shape produce a very random array. Later in 1994, Underbrink [25, 29], also with Boeing, developed a multi-arm spiral array, which has become somewhat of a standard array shape since. In 1995, Elias [31] published a paper describing optimal beamforming using a cross-shaped array. A cross array is simply two line arrays oriented orthogonally to each other. Elias devised a method that did not use every pair of sensors in the cross array, instead using only pairs formed between the orthogonal line sub-arrays. At the Applied Research Laboratory, University of Texas at Austin, Gramann and Mocio [32] applied a method called adaptive beamforming to wind tunnel measurements in 1995. This method allows for the

steering vectors used in beamforming to adapt to the specific set of signals sampled by the microphones. This group also applied array shading, which applies a different weight to each sensor signal, generally tapering the contribution of the outer microphones to subdue sidelobes. A 1998 paper by Dougherty and Stoker [25] compares many of the advanced beamforming techniques and introduces a technique called CLEAN, borrowed from the radio astronomy and remote sensing communities. CLEAN is an iterative technique that finds the highest power detected in the scanned area, calculates the array pattern that would result from a source at that position, and subtracts the pattern from the image. In theory, the technique can reduce the array response to an impulse at every source.

A growing number of flyover array measurements occurred during the 2000's. In 2002, Sijtsma and Stoker [33], with NLR and Boeing respectively, used a 243-element array at the Amsterdam Schiphol Airport for a campaign to analyze airframe noise on the Boeing 737 and Airbus A340. The Boeing Company, in partnership with Rolls-Royce, initiated the Quiet Technology Demonstrator (QTD) program in 2001 and continued with QTD2 in 2005 [34]. These massive campaigns analyzed noise on Boeing 777 aircraft and QTD2 involved an array positioned before a landing strip, consisting of up to 600 microphones [35].

Wind tunnel and field array experiments involving wind turbines began in the 2000's. Sijtsma, Oerlemans, and Holthusen [36], with NLR, analyzed both a model helicopter and a model wind turbine in a wind tunnel environment in 2001 using an array. In 2004, Oerlemans and Migliore [37], from NREL, performed wind tunnel aeroacoustic tests on several wind turbine airfoils. In 2005, Oerlemans [38] led an array measurement campaign on an operational wind turbine in the field. The tests involved a 58 meter diameter turbine and used an array of 152 microphones. Oerlemans, et al. [39] continued wind turbine field testing in 2008 with a GE 2.3 megawatt, 94 meter diameter wind turbine using an array of 148 sensors. This test campaign compared the effects of various airfoils on noise emissions and showed that the dominant aeroacoustic noise source on a wind turbine is trailing edge noise near the outboard region of the blades. The noise is amplified during the downward travelling part of rotation due

to Doppler amplification. The tests compared an optimized airfoil, an airfoil with a serrated trailing edge, and a baseline blade. In 2008, Sandia National Laboratories conducted wind tunnel aeroacoustic measurements of wind turbine airfoils using arrays [40]. It is also important to note that although relatively little work has been performed using arrays for wind turbine analysis in the field, single microphone measurements have been used extensively to measure overall noise levels. The IEC 61400-11 document published by the International Electrotechnical Commission outlines a standard process by which sound levels can be measured [41].

1.1.1 Wind Turbine Noise

Wind turbine noise, as mentioned earlier, is one of the obstacles preventing universal acceptance of wind energy. There is often a Not In My Backyard (NIMBY) attitude toward large wind farms. The public realizes the advantages of clean wind energy, but often doesn't want to have to live with the sight of wind turbines or the sounds they emit. Usually, people near wind farms describe the noise as an annoyance or "nuisance" [1]. The problem is exacerbated by the periodic nature of wind turbine noise. Rather than blending in with background "white" noise, wind turbines produce periodic "swishing" sounds as the blades pass through the air. Since terms such as "annoyance" are very qualitative and difficult to define, governments enforce noise level restrictions, which wind farms must adhere to. For example, Germany, in 1995, had limits of 55 decibels (dB) during the day and 45 dB during the night for residential areas and 50 dB during the day and 35 dB during the night for rural areas [1]. The Netherlands had stricter guidelines with day and nighttime limits of 45 dB and 35 dB for residential areas and 40 dB and 30 dB for rural areas. Noise of a tonal nature produces even more annoyance than broadband noise, so countries usually impose penalties of 5 dB for tonal characteristics. This means that in the Netherlands, for example, if a rural wind farm produces a pure acoustic tone during nighttime operation, the noise from the wind farm must not exceed 25 dB at any residence instead of the normal 30 dB limit.

In an ideal environment, noise propagates such that for every doubling of distance from

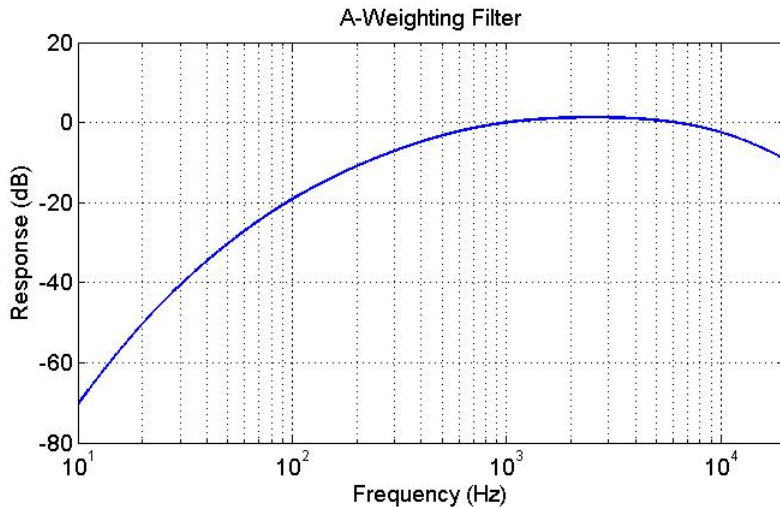


Figure 1.4: Spectrum of A-Weighting Filter

the source, the sound pressure amplitude decreases by a factor of two (and the sound power decreases by a factor of four). By doubling the distance from an acoustic source, the SPL will decrease by 6 dB. To illustrate the importance of the reduction of noise produced by a wind turbine by a seemingly small amount like 6 dB, consider a wind farm that must be located two miles from the nearest residence due to noise regulations. If engineers are able to design an airfoil that is 6 dB quieter than the original model, the wind farm can be located half the original distance from a residence while still adhering to noise laws. The wind farm can then be positioned an entire mile closer to a residential area.

The human ear is not equally sensitive to all frequencies of noise, so a filter known as the "A" weighting filter is applied to the noise levels before determining if the overall sound pressure level exceeds local guidelines [1]. The A-weighted filter lessens the importance of low frequency and high frequency noise while emphasizing the range near 1 kHz to which the human ear is most sensitive. A plot of the filter used to determine A-weighted sound levels is shown in figure 1.4.

Mechanical noise on wind turbines located in the nacelle is primarily due to the gearbox, generator, and cooling fans [1]. Gearbox noise, which is usually dominant, is caused by imperfections in the construction of gear teeth and can be solved by improved manufacturing

techniques and vibration isolation. It is the aeroacoustic noise produced by the passage of the rotor through the air that is currently the focus of many research studies in wind turbine noise. Several sources of acoustic noise exist on wind turbine airfoils. Most of these sources appear to propagate from near the tip of the blade because the sound intensity scales with the 5th or 6th power of speed and the blade tip regions are the fastest travelling portions of the rotor [1]. The strong dependence of sound intensity on speed means that a 15% increase in rotor speed causes a doubling, or 3 dB increase, of the sound intensity.

As the blade travels in front of the tower of the turbine, there is a rapid change in the loading of the blade. This is because the tower disrupts the flow of air in front of and behind it [1]. This unsteady loading causes noise at the blade passing frequency and harmonics thereof. This tonal noise has a very low fundamental frequency because the rotational speeds of wind turbines are relatively low. The harmonics tend to die out quickly as frequency increases. After applying the A-weighted filter, this noise does not have much of an effect on overall SPL. However, some low frequency noise can match the resonant frequencies of buildings or human organs and cause structural stress and discomfort. Modern turbines are designed such that the rotor is upwind of the tower and the effect of unsteady loading noise is much less than for downwind turbines, where the blades pass through the tower wake. Therefore, this noise source is of lower importance.

Inflow turbulence is one of the dominant causes of aeroacoustic noise [1, 42]. As the blade passes through turbulent air, the interaction of the blade with turbulence produces broadband noise. If the length scale of the turbulence is on the order of or larger than the blade length, the blade acts as a dipole source and radiates very low frequency noise. When the length scale of the turbulence is much smaller than the blade, the turbulent eddies scatter off of the leading and trailing edges of the airfoil, producing high frequency noise. Turbulent inflow noise is a significant source of noise below 1 kHz and is perceived as a “swishing” sound.

The dominant source of noise at higher frequencies is airfoil self-noise, radiated at the trailing edge of the blade [1]. Trailing edge self-noise is broadband in nature and is also perceived

as a swishing sound when the blade passes through the air. This broadband noise, referred to as “trailing edge” noise peaks between 500 and 1500 Hz and dominates all frequencies above 1 kHz. A turbulent viscous boundary layer exists near the surface of the airfoil, which creates turbulent eddies. Although these eddies are not efficient radiative sources themselves, when they interact with the sharp trailing edge of the blade, they radiate very efficiently.

Another important noise mechanism is blunt trailing edge noise [1]. If the trailing edge of the blade is blunt instead of sharp, it will shed vortices that emit tonal noise. The noise frequency is inversely proportional to the blunt trailing edge thickness. A typical “sharp” trailing edge with a thickness of a few millimeters will shed vortices that create noise in the ultrasonic range that cannot be perceived by humans. Most literature on the subject suggests sharpening the trailing edge as a way to mitigate this noise source. However, some modern blade designs reduce airfoil chord length to improve structural stability, while using less material, by employing blunt trailing edges on the inboard section of the blade [43]. Analysis of blunt trailing edge noise is an important research area for this reason.

Several other possible sources of noise exist which generally don’t contribute heavily to overall noise levels. It is thought that the interaction of the suction and pressure sides of the airfoil at the blade tip creates vortices that interact with the blade, producing noise [1]. Relatively little is known about this phenomenon known as “tip” noise. When an airfoil enters stall, the turbulent boundary layer near the surface is greatly increased and very loud noise can result. Since most modern turbines are pitch controlled, they will not enter stall enough to cause this to be a source of concern. Airfoil surface roughness adds disturbances to the flow and can contribute to noise too. Examples of this mechanism are dirt and insects stuck on the blades, vortex generators to prevent flow separation, and slits or cavities on the surface of the blades. Because of this noise mechanism, blade designs with ailerons are unfavorable because the slits between the fixed blade and the control surfaces act as loud sources [42]. A final source of noise, called “laminar boundary layer vortex shedding,” can occur on small and medium sized wind turbines [44]. For low Reynolds number flows ($Re < 10^6$), the boundary layer of the

airfoil will remain laminar until near the trailing edge of the blade. An interesting phenomenon occurs whereby a feedback loop is formed between forward propagating trailing edge noise and backward propagating instabilities in the laminar boundary layer. This feedback loop can create very strong sources of noise but is not an issue for modern utility-size wind turbines.

Due to convective amplification and source directivity, aeroacoustic noise is strongest during the downward half cycle of rotation when observed from the ground [38]. This is because trailing edge noise sources have higher directivity in the direction of travel of the blade and are amplified in the direction of travel. Convective amplification is the phenomena of signal amplification due to the Doppler effect and is modeled as an increase in power by a factor of $(1 - M_r)^{-4}$ where M_r is the Mach number of the source relative to an observer [39]. When an observer is below a wind turbine rotor, the downward travelling half of rotation will present the highest relative velocities and the swishing sound will be most apparent. This has been evidenced by the NLR wind turbine acoustics studies [38, 39].

Some work in the area of wind turbine airfoil noise reduction has been performed. Obviously, reducing the rotational rate of a wind turbine will decrease noise levels, but when left as the only source of noise mitigation, is very unfavorable. The optimal power output of a turbine is designed to a certain tip speed ratio (ratio of blade tip speed to wind speed), so an excessive reduction in speed will negatively impact the aerodynamic efficiency [1]. A tip speed reduction of 15% can cause the generated power to decrease by about 6%, depending on the turbine design.

Aside from slowing the rotor, minor blade modifications have been shown to reduce noise levels. Studies in wind tunnel environments have shown that different blade tip shapes can alter the total SPL by a few dB [45]. The most promising area of noise reduction is trailing edge modification. Wind tunnel experiments have shown that a reduction of 6 dB can be achieved by creating a serrated trailing edge near the blade tip [45]. The spacing and length of the serrations effects the noise mitigation. While serrations generally reduce the overall SPL of an airfoil, the ratio of the length of the serrations to the spacing effects what frequency the peak SPL is located at [1]. Work has been done in the area of acoustically optimized airfoil shapes using computer

codes [45]. The acoustically optimized airfoils were only implemented on the outer 20% of the blades. In the wind tunnel, a 3 dB reduction in SPL was shown with an optimized blade shape. The importance of wind turbine measurements is apparent when comparing wind tunnel results to field results. For example, the SIROCCO campaign showed that the acoustically optimized airfoil, causing a 3 dB decrease in the wind tunnel, exhibited only a 0.6 dB decrease in SPL over a baseline blade in the field [45]. The same campaign provided the very promising result that trailing edge serrations can reduce overall sound levels by 3.2 dB, even though this is less than what wind tunnel experiments showed. Also shown by SIROCCO was the effect of blade roughness on noise levels. A cleaned blade and a blade with small trips placed on the surface were compared with a baseline blade. The cleaned blade proved to be slightly quieter than the dirty blade while the tripped blade yielded much higher levels than either of the other two.

Obviously it is very important to examine the aeoacoustics of a wind turbine during operation in the field rather than just in a wind tunnel environment. For this reason, the development of acoustic arrays specifically designed for application in an outdoor wind turbine environment is an important research area. Again, even small reductions in airfoil noise can have dramatic effects and this is driving efforts in wind turbine aeroacoustics research. Even a reduction in SPL as small as 3 dB, can be very beneficial. If a wind farm project has a certain “budget” of noise that is allowed, say 40 dB, and the nearest turbine is restricted to be positioned two miles from a residence because of turbine noise levels, a 3 dB reduction in SPL will allow the turbine to be placed 1,000 yards closer to the residence while adhering to the original noise constraint.

Chapter 2

Array Signal Processing Theory

The advantages of using an array of sensors for noise analysis include the ability of the array to achieve spatial directivity in its signal reception pattern. Beamforming is the name given to the process of algorithmically steering the array's directivity pattern toward a particular direction of arrival (DOA) or a particular point in space. Like any finite size antenna, an array's directivity pattern will have a mainlobe, or beam, and multiple sidelobes, hence the term *beamforming* [4]. In practice, beamforming involves scanning a grid of discrete points in space, usually a rectangular grid with a discrete number of scan points in the x and z directions. For example, if a beamforming algorithm scans a rectangular area in space that is 10 meters-by-10 meters and scans every 25 cm in the x direction and every 10 cm in the z direction, the beamformer will calculate $z(t)$ for $\frac{10}{0.25} \cdot \frac{10}{0.1} = 4000$ discrete points in space. In this research, the scanning plane of interest is a rectangular area that includes the rotor plane of the wind turbine. Figure 2.1 shows the scan plane centered around the rotor plane, the relative positioning of the array, and the x , y , z coordinate system that is used in this research. Note that the origin of the coordinate system is located at the center of the array. The most basic beamforming algorithm is called delay-and-sum beamforming [4] and the beamforming algorithms used in this research are derived from this method.

The collection of results from beamforming over the scanned grid points is referred to as the “noise map” in this thesis. An example of a noise map is shown in figure 2.2 for a beamforming scenario like the one in figure 2.1. For this analysis, the scan grid consists of 100-

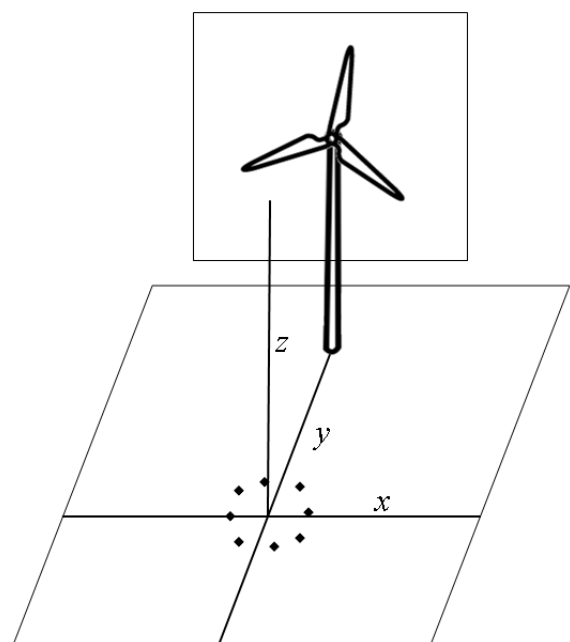


Figure 2.1: Scan Plane, Array Location, and Coordinate System

by-100, or 10,000, discrete grid points over a 30 meter-by-30 meter scan plane centered around the wind turbine hub, which is the center of the figure. The hub height is 22.82 meters and the array is located 22.82 meters upwind from the turbine. For this case, a 1 kHz source was located 5 meters to the right of the hub. Note that the location of the hub as well as the outline of the rotor disc is indicated in the noise map. Displayed on the noise map is the power detected at each grid point in terms of decibels below the peak power, which in this case is the power detected at the source location. An ideal beamformer would return power only when the array is steered directly at a source. Due to the impossibility of creating a perfect beamformer, the noise map contains some residual power detected at other locations due to coincidental phase matching between sensors in the array. The relatively high regions of residual power are called sidelobes.

2.1 Delay-and-Sum Beamforming

Delay-and-sum beamformers [4] introduce a delay to each sensor waveform output equal to the amount of time it takes a signal propagating from the assumed position \vec{x}^0 to travel between that sensor (sensor m) and a reference sensor (sensor 0). The delayed sensor output waveforms are then multiplied by a weight factor, w_m , and summed to produce the beamformer output waveform $z(t)$, [46]

$$z(t) \triangleq \sum_{m=0}^{M-1} w_m y_m(t - \Delta_m), \quad (2.1.0.1)$$

where $y_m(t)$ is the signal from microphone channel m . The time delay, Δ_m , is described by

$$\Delta_m = \frac{r_0 - r_m}{c} \quad (2.1.0.2)$$

where r_m is the distance from the assumed source position and sensor m and c is the speed of propagation. If it is assumed that the source is in the farfield, then Δ_m can be written in the form of

$$\Delta_m = \frac{\vec{x}^0 \cdot \vec{x}_m}{|\vec{x}^0| c} \quad (2.1.0.3)$$

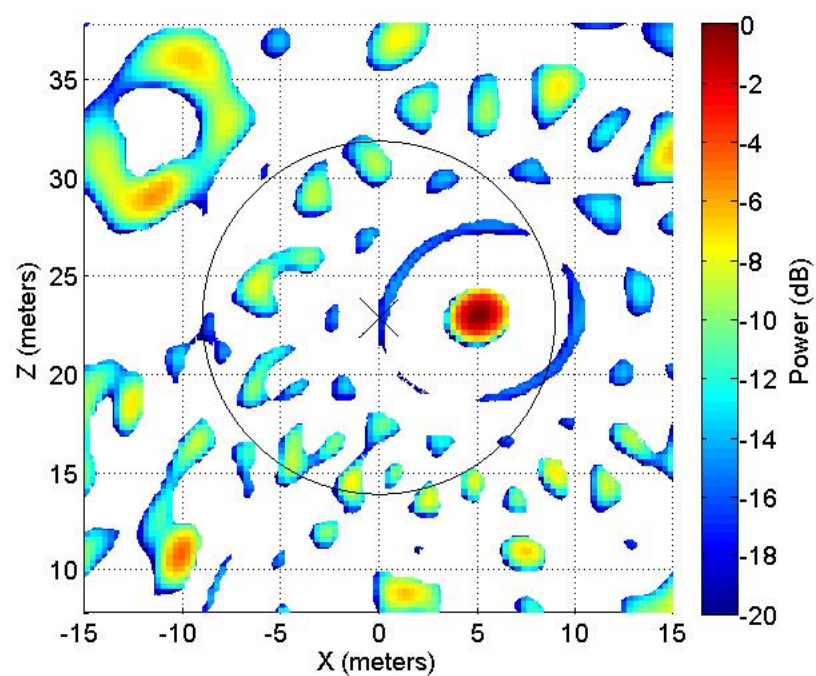


Figure 2.2: Beamforming Output or “Noise Map”

where $\frac{\vec{x}^0}{|\vec{x}^0|}$ is a unit vector in the direction of the assumed propagating signal. The weight factor, w_m , is commonly chosen to normalize the amplitude of $y_m(t)$ to that of $y_0(t)$. The formula for w_m in this case is

$$w_m = \frac{r_m}{r_0}. \quad (2.1.0.4)$$

If the distance from the assumed source to all sensors is approximately equal, then $w_m = 1$ is satisfactory for all sensors. This is not necessarily the case in this research, since some microphones are placed very close to the turbine tower while others are positioned much farther away. The output of the delay-and-sum beamformer when a signal $x(t)$ is propagating from position \vec{x}^0 is

$$z(t) = \left(\sum_{m=0}^{M-1} w_m \right) x(t) = Mx(t) \quad (2.1.0.5)$$

assuming $w_m = 1$.

2.1.1 Array Pattern

An important characteristic of an array is the *point spread function* [47] or *array pattern* [4]. Assuming that there is a monotone point source located at position \vec{x}^0 with a frequency ω^0 , the source will correspond to a spatial frequency projected across the array sensors in the xy plane, $\vec{k}^0 = \left[\pm \frac{2\pi}{\lambda_x}, \pm \frac{2\pi}{\lambda_y}, \pm \frac{2\pi}{\lambda_z} \right]$, where λ_a is the wavelength in meters in the a dimension and the sign of \vec{k}^0 contains information regarding the direction of wave propagation. Equation 2.1.0.5 gives the output when the beamformer is steering the array toward \vec{x}^0 . The array pattern describes what the output of the beamformer will be when the array is instead steered toward a different point in space \vec{x}' . The monotone signal propagating from \vec{x}^0 can be represented as a complex exponential, having the form

$$x(t) = e^{j(\omega^0 t + \vec{k}^0 \cdot \vec{x} + \phi)}. \quad (2.1.1.1)$$

By defining $\vec{\zeta} = \frac{\vec{x}}{|\vec{x}|}$ and using the relation $\vec{k} = \frac{\omega^0 \vec{\zeta}}{c}$, equation 2.1.0.1 for delay-and-sum beamforming results in

$$z(t) = \sum_{m=0}^{M-1} w_m e^{j(\omega^0 t + \vec{k}^0 \cdot \vec{x}_m - \Delta_m + \phi)} \quad (2.1.1.2)$$

$$= \sum_{m=0}^{M-1} w_m e^{j(\omega^0 t + \vec{k}^0 \cdot \vec{x}_m - \frac{\vec{\zeta} \cdot \vec{x}_m}{c} + \phi)} \quad (2.1.1.3)$$

$$= \sum_{m=0}^{M-1} w_m e^{j(\omega^0 ((\frac{\vec{\zeta}^0}{c} - \frac{\vec{\zeta}'}{c}) \cdot \vec{x}_m))} e^{j(\omega^0 t + \phi)} \quad (2.1.1.4)$$

$$= W(\omega^0 (\frac{\vec{\zeta}^0}{c} - \frac{\vec{\zeta}'}{c})) e^{j(\omega^0 t + \phi)} \quad (2.1.1.5)$$

$$= W(\vec{k}^0 - \vec{k}') e^{j(\omega^0 t + \phi)}. \quad (2.1.1.6)$$

The time independent term in 2.1.1.6 is the array pattern evaluated at a specific spatial frequency and is the Fourier transform of the array shape reflected about the origin and shifted in \vec{k} space by $\vec{k}^0 - \vec{k}'$. The Fourier transform of the array shape, the array pattern [4], is formally defined as

$$W(\vec{k}) \triangleq \mathcal{F} \left\{ \sum_{m=0}^{M-1} w_m \vec{x}_m \right\} \quad (2.1.1.7)$$

$$= \sum_{m=0}^{M-1} w_m e^{j(\vec{k} \cdot \vec{x}_m)}. \quad (2.1.1.8)$$

Equation 2.1.1.6 shows that the output of the beamformer steered toward \vec{x}' with a monotone point source at \vec{x}^0 is simply the source signal $x(t)$ multiplied by a factor equal to the Fourier transform of the array shape at the frequency $\vec{k}^0 - \vec{k}'$. This means that the amount of steered error in \vec{k} space that the beamformer assumes determines the amount the beamformer suppresses $z(t)$ at that steering angle. If the beamformer is steered directly towards \vec{x}^0 , then the array factor is simply $W(\vec{0})$ or the DC value of the array shape. The DC value of a function is just the sum of its elements or, in the case of the array shape, $\sum_{m=0}^{M-1} w_m$. This is consistent with equation 2.1.0.5.

2.2 Frequency Domain Beamforming

Conventional beamforming is based on a frequency domain algorithm for delay-and-sum beamforming [48]. The basis for this approach is simply the Fourier transform of equation 2.1.0.1 given by

$$Z(\omega) = \mathcal{F} \left\{ \sum_{m=0}^{M-1} w_m y_m(t - \Delta_m) \right\} = \sum_{m=0}^{M-1} w_m Y_m(\omega) e^{-j\Delta_m \omega}. \quad (2.2.0.1)$$

By defining two vectors, a simple representation of equation 2.2.0.1 can be formed. $Y(\omega_k)$ is defined as an $M \times 1$ column vector representing the amplitude and phase at the frequency ω_k of the signals detected at sensors 1 through M [46]. When $Y_m(\omega)$ is defined as $\mathcal{F}\{y_m(t)\}$, $Y(\omega_k)$ can be written as

$$Y(\omega_k) = \begin{bmatrix} Y_1(\omega_k) \\ \vdots \\ Y_M(\omega_k) \end{bmatrix}. \quad (2.2.0.2)$$

An $M \times 1$ vector called the *steering vector* [4] contains the weight and phase delay information of the sensors for an assumed source at location \bar{x}' . The steering vector is defined as

$$e(\omega_k) = \begin{bmatrix} w_1 e^{j\Delta_1 \omega_k} \\ \vdots \\ w_M e^{j\Delta_M \omega_k} \end{bmatrix}. \quad (2.2.0.3)$$

Using $Y(\omega_k)$ and the steering vector, equation 2.2.0.1 can be written as

$$Z(\omega_k) = e(\omega_k)^\dagger Y(\omega_k) \quad (2.2.0.4)$$

where $[\bullet]^\dagger$ is the Hermitian transpose operator. Since array signal processing is performed digitally, there will only be a finite number of frequency bins that can be detected when the Fast Fourier Transform (FFT) is applied to $y_m(t)$. Therefore, $e(\omega_k)$ can be represented by e_k where k is the k^{th} frequency bin. Now, $Z(\omega_k)$ can be represented by

$$Z_k = e_k^\dagger Y_k. \quad (2.2.0.5)$$

A useful value to calculate is the power detected at the k^{th} frequency bin. This power is equivalent to $P_k = |Z_k|^2$ and Z_k is a complex variable, so $P_k = Z_k Z_k^*$. The power of the

beamformer using steering vector e_k can therefore be written as

$$P_k = Z_k Z_k^* \quad (2.2.0.6)$$

$$= (e_k^\dagger Y_k)(e_k^\dagger Y_k)^*. \quad (2.2.0.7)$$

Using matrix properties, equation 2.2.0.7 can be represented as

$$P_k = (e_k^\dagger Y_k)(e_k^\dagger Y_k)^* \quad (2.2.0.8)$$

$$= (e_k^\dagger Y_k)(Y_k^\dagger e_k) \quad (2.2.0.9)$$

$$= e_k^\dagger (Y_k Y_k^\dagger) e_k. \quad (2.2.0.10)$$

The expression given in 2.2.0.10 is the formula most commonly implemented in conventional frequency domain beamforming algorithms, including the algorithm used in this research. P_k as a function of e_k is known as the *steered power response* [4]. The $M \times M$ matrix $(Y_k Y_k^\dagger)$ is so important that it is given a special name, the *cross spectral matrix*, or *CSM*, represented by the matrix \mathbf{R} , making P_k equivalent to $e_k^\dagger \mathbf{R}_k e_k$ [47]. Part of the beauty of equation 2.2.0.10 is that it allows for the CSM to be determined only once for the entire operation of the beamforming algorithm. When P_k is calculated for a new point on the scanning grid, the only variable that must be recalculated is the steering vector e_k . With this in mind, great care can be taken when estimating the CSM without harming the computational efficiency of the beamforming algorithm. The CSM in its expanded form is represented as

$$\mathbf{R}_k = \begin{bmatrix} Y_{k1} Y_{k1}^* & \cdots & Y_{k1} Y_{kM}^* \\ \vdots & \ddots & \vdots \\ Y_{kM} Y_{k1}^* & \cdots & Y_{kM} Y_{kM}^* \end{bmatrix}. \quad (2.2.0.11)$$

Since the CSM contains information from the sensors containing signal plus noise terms, the CSM must be estimated. In practice, the matrix $\hat{\mathbf{R}}_k$ is used where

$$\hat{\mathbf{R}}_k = \mathbf{E}[Y_k Y_k^\dagger] \quad (2.2.0.12)$$

$$= \frac{1}{N} \sum_{n=1}^N Y_{k,n} Y_{k,n}^\dagger \quad (2.2.0.13)$$

and \mathbf{N} is the number of blocks of sensor data that the FFT is performed on. Although the formula in 2.2.0.13 is used in practice [47], an alternate CSM estimate can be used which will be explained in more detail in section 3.1 on signal estimation.

2.2.1 Linearity of the Conventional Beamformer

A typical wind turbine scan plane will contain many separate acoustic sources, so when analyzing the noise map produced by beamforming, it is important to be able to treat the map as a superposition of the individual source responses. It has been shown that the delay-and-sum beamformer behaves like a linear system. The conventional beamforming method utilized in this research calculates the *power* detected across the scan plane, however. Power is in general not a linear operator, so care must be taken when treating the noise map, $P_k = |Z_k|^2$, produced through conventional beamforming as the superposition of the squared magnitude of multiple array patterns. In order to arrive at the conclusion that the conventional beamformer is linear in power, the nature of the sources must be examined. Two assumptions about the acoustic sources will be made. The first is that the phase of the k^{th} bin of the n^{th} FFT block calculated from a received microphone signal is independent of the phase of the k^{th} bin of the m^{th} FFT block when $m \neq n$. The second assumption is that the phase of the signal produced by the l^{th} acoustic source is independent of the phase of the p^{th} acoustic source for all FFT blocks and bins and for all $p \neq l$. This assumption treats the acoustic sources as independent, “white” random processes. With this information, the elements of the N-block CSM estimate with L sources can be written as

$$\hat{\mathbf{R}}_{k,i,l} = \frac{1}{N} \sum_{n=1}^N \left[\left(\sum_{u=1}^L A_u e^{j\phi_{i,u,n}} \right) \left(\sum_{v=1}^L A_v e^{-j\phi_{l,v,n}} \right) \right] \quad (2.2.1.1)$$

$$= \frac{1}{N} \sum_{n=1}^N \left[\sum_{u=1}^L A_u^2 e^{j(\phi_{i,u,n} - \phi_{l,u,n})} + \sum_{u=1}^L \sum_{v \neq u}^L A_u A_v e^{j(\phi_{i,u,n} - \phi_{l,v,n})} \right]. \quad (2.2.1.2)$$

In the limit as $N \rightarrow \infty$ or $L \rightarrow \infty$, equation 2.2.1.2 reduces to

$$\hat{\mathbf{R}}_{k,i,l} = \sum_{u=1}^L \left(A_u^2 e^{j(\phi_{i,u} - \phi_{l,u})} \right), \quad (2.2.1.3)$$

because the real and imaginary parts of the terms $A_u A_v e^{j(\phi_{i,u,n} - \phi_{l,v,n})}$ are independent and zero-mean for all $u \neq v$ and n , and therefore reduce to zero. The conventional beamformer with equation 2.2.1.3 as the CSM elements can be written as

$$P_k = \sum_{i=1}^M \sum_{l=1}^M w_i e^{-j\Delta_i \omega_k} w_l e^{j\Delta_l \omega_k} \sum_{u=1}^L \left(A_u^2 e^{j(\phi_{i,u} - \phi_{l,u})} \right) \quad (2.2.1.4)$$

$$= \sum_{u=1}^L \left(\sum_{i=1}^M \sum_{l=1}^M w_i e^{-j\Delta_i \omega_k} w_l e^{j\Delta_l \omega_k} A_u^2 e^{j(\phi_{i,u} - \phi_{l,u})} \right). \quad (2.2.1.5)$$

It is equation 2.2.1.5 that reveals that the conventional beamformer output contains the superposition of the squared magnitude array patterns of the L sources:

$$P_k = \sum_{u=1}^L (Z_{k,u} Z_{k,u}^*). \quad (2.2.1.6)$$

2.2.2 Beamforming with General Sources

Now that the frequency domain beamformer has been derived, a general case of the beamformer solution can be shown. Johnson and Dudgeon [4] give an elegant generalization to the beamforming result when the source is no longer constrained to be a point source. The generalization begins by representing the space-time signal incident on sensor m by its inverse space-time Fourier transform as shown in equation 2.2.2.1.

$$s(\vec{x}_m, t) = \frac{1}{(2\pi)^4} \int_{-\infty}^{\infty} \int_{-\infty}^{\infty} S(\vec{k}, \omega) e^{j(\omega t + \vec{k} \cdot \vec{x}_m)} d\vec{k} d\omega \quad (2.2.2.1)$$

Using the equation for frequency domain beamforming given in 2.2.0.1, the beamformer output can be represented as

$$z(t) = \frac{1}{(2\pi)^4} \int_{-\infty}^{\infty} \int_{-\infty}^{\infty} \sum_{m=0}^{M-1} w_m S(\vec{k}, \omega) e^{j(\omega t + \vec{k} \cdot \vec{x}_m)} e^{-j\vec{k}' \cdot \vec{x}_m} d\vec{k} d\omega \quad (2.2.2.2)$$

$$= \frac{1}{(2\pi)^4} \int_{-\infty}^{\infty} \int_{-\infty}^{\infty} S(\vec{k}, \omega) W(\vec{k} - \vec{k}') e^{j\omega t} d\vec{k} d\omega \quad (2.2.2.3)$$

By observing equation 2.2.2.3, the beamforming result $z(t)$ can be thought of as the spatial convolution in the frequency domain between the source waveform and the reflected array pattern. A simpler interpretation of this result is

$$z(\vec{k}', t) = S(\vec{k}, t) * W(\vec{k} - \vec{k}'). \quad (2.2.2.4)$$

Equation 2.2.2.4 illustrates one of the most important features of the conventional beamforming process, that the beamformer is a linear system (even when sources are not constrained to be point sources). Therefore, the beamformer output for an input signal consisting of many point sources will be equivalent to the summation of multiple shifted array patterns. An implication of this is that the average beamformer output for multiple signals is equivalent to the beamformer output for an input signal consisting of the average of the individual signals. This allows faster computation of the time average of acoustic signals because the computationally expensive beamforming process need only be performed once. Another important result of equation 2.2.2.4 is that since the Fourier transform is a linear system as well, the beamformer output is a linear function of the array shape. The latter result is useful in array shape design.

2.3 Array Shape Theory

Section 2.1.1 shows that the result of beamforming over a plane in space with a single point source located in that plane is the Fourier transform of the array shape with the origin centered at the location of the point source. It may be counterintuitive to visualize the Fourier transform being projected onto a plane in space, but the result greatly simplifies designing an array shape. The array pattern (equation 2.1.1.8) is a function of \vec{k} , which is the projection of the spatial wavenumber of the source onto the array. The projection of the wavenumber of a point source onto each sensor will be slightly different due to the different angle formed between the sensor positions, the xy plane, and the source. The wavenumber for the frequency of interest is calculated as $k_l = \frac{2\pi f_l}{c}$, where f_l is the frequency of interest. The projected wavenumber of a source onto a position on the xy array plane is

$$k_{l,p} = k_l \cos(\arctan(\frac{z_s}{\sqrt{(x_s - x_0)^2 + (y_s - (y_0))^2}})) \quad (2.3.0.1)$$

where x_s, y_s, z_s is the position of the source and x_0, y_0 is the position on the xy plane onto which the wavenumber is projected. Further values of interest are the x component of the projected

wavenumber and the y component of the projected wavenumber, $k_{l,p,x}$ and $k_{l,p,y}$.

$$k_{l,p,x} = \text{sgn}(x_s - x_0) \cdot k_{l,p} \cdot \sin(\arctan(\frac{x_s - x_0}{y_s - y_0})) \quad (2.3.0.2)$$

$$k_{l,p,y} = k_{l,p} \cdot \cos(\arctan(\frac{|x_s - x_0|}{y_s - y_0})) \quad (2.3.0.3)$$

The sgn function is defined as

$$\text{sgn}(x) = \begin{cases} -1 & \text{if } x < 0 \\ 0 & \text{if } x = 0 \\ 1 & \text{if } x > 0 \end{cases} \quad (2.3.0.4)$$

The beamforming results will only almost perfectly resemble the shifted array pattern if the array is in the far field of the source. To determine whether or not the array is in the far field, it will be assumed that a point source is located in the center of the scan plane. The center of the scan plane for the prototype array field test with a 100 kW wind turbine at the National Wind Technology Center (NWTC) is the location of the turbine hub, which is at a height of 36.4 meters. The center of the array is located 36.4 meters upwind from the wind turbine (this choice of array position will be explained in section 2.3.1). In reference to figure 2.1, the center of the array would be located at 0,0,0 and the center of the scan plane would be located at 0,36.4,36.4. Figure 2.3 shows the spatial wave of a 250 Hz source located at the scan plane center, or turbine hub, projected onto the xy array plane. Figure 2.4 illustrates the x and y components of the wavenumbers from the same source projected onto the array plane. Note that the wavenumber components vary by as much as 2 radians over the range of the array plane. The array plane size shown is about the same array size that is needed for adequate resolution at 250 Hz, which will be discussed later.

Let the far field be defined as the distance from the source where the phase of the signals received at each sensor differ by no more than $\lambda/16$ or $\pi/8$ radians from the phase detected if the received signal is a perfect plane wave. It is clear from figure 2.3 that the array is not in the far field of the source as defined in this sense. In general, the array pattern will not be equivalent to

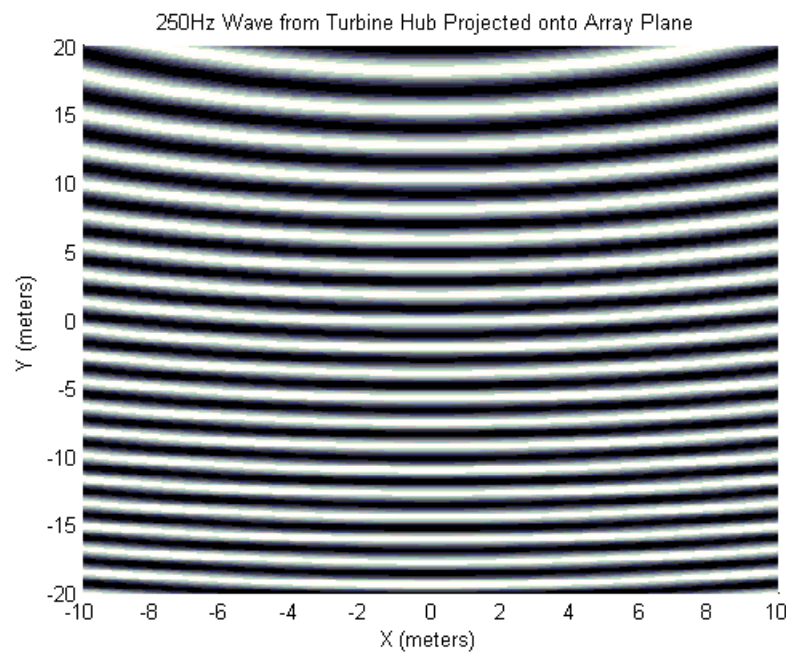


Figure 2.3: Projection of 250Hz Wave from Scan Plane Center onto Array Plane

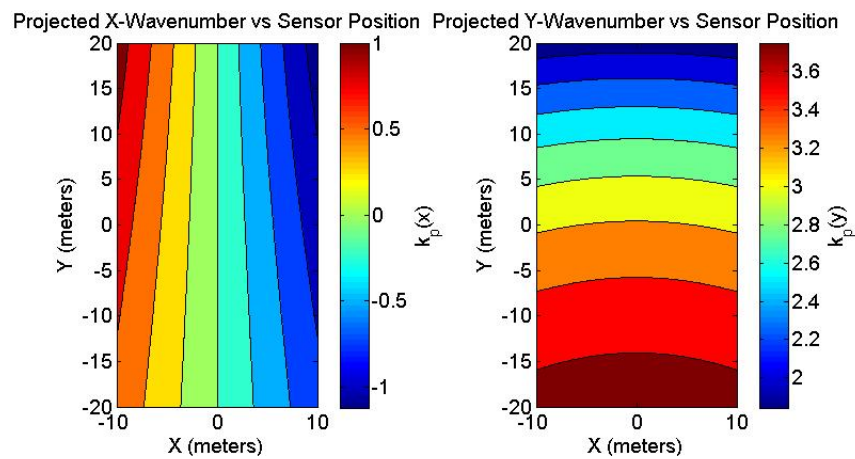


Figure 2.4: X and Y Components of Wavenumber for a 250 Hz Source at Scan Plane Center Projected onto Array Plane

the Fourier transform of the array shape as defined in equation 2.1.1.8. However, in practice, the encountered array pattern is sufficiently close to this definition to make the Fourier transform of the array shape a valuable tool in designing an array.

There are two important characteristics of an array pattern that must be considered: the mainlobe width, or *resolution*, and the relative sidelobe levels. The mainlobe width of the array pattern, which is centered around the origin, is defined as the half power or -3 dB beamwidth [48]. This will be referred to as the *beamwidth*. The *sidelobe rejection* is defined as the ratio between the mainlobe level and the level of the highest sidelobe of interest [25]. Generally, an array designer would like to have an array with a narrow beamwidth and high sidelobe rejection. The array pattern is a function of the wavenumber of a source propagating from a scan location projected onto the array plane. In particular, the x and y components of the wavenumber determine the array response because the array is contained in the xy plane and therefore cannot detect a change of spatial frequency in the z direction. When analyzing the array pattern, the wavenumbers $k_{l,p,x}$ and $k_{l,p,y}$ at the center of the array will be used to represent the wavenumber for all points in the array although this is just an approximation as evidenced by figure 2.4. Figure 2.5 shows the $k_{l,p,x}$ and $k_{l,p,y}$ values that would be caused by 1 kHz point sources at any point on the 30 meter-by-30 meter scan plane centered around the turbine hub. Since $k_{l,p,x}$ and $k_{l,p,y}$ are proportional to f_l , the frequency of the acoustic signal being analyzed, the array pattern at any frequency f_m will be a scaled version of the pattern at f_l if they are located at the same position. The value at any point on the array pattern produced by a tone with frequency f_l will be present on the array pattern from the source with frequency f_m but stretched by a factor of $\frac{f_m}{f_l}$ away from (or towards) the location of the source. If an array is designed for one frequency, then while looking at a source twice that frequency, the resolution will be half of the original value, but all sidelobes will be twice as close to the mainlobe, which may be undesirable. When the source observed is half the frequency of the intended array frequency, then the resolution is twice the original value but sidelobes are twice as far away from the mainlobe. This way there are advantages and disadvantages to observing

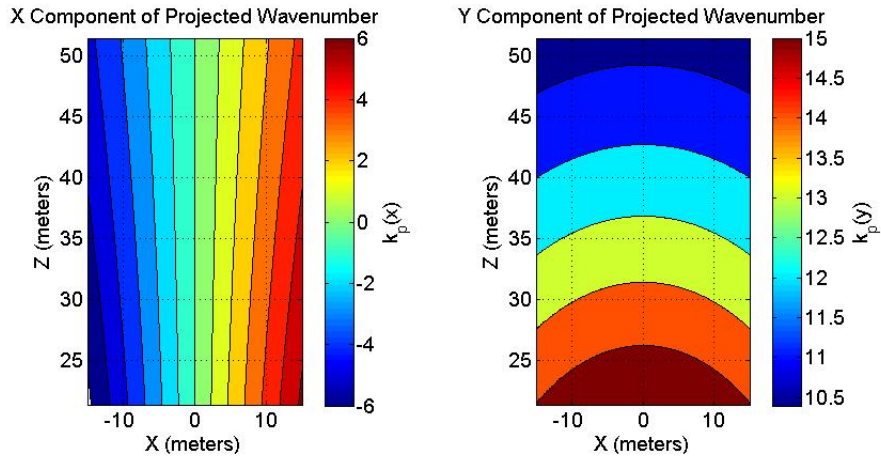


Figure 2.5: X and Y Components of Wavenumber for a 1 kHz Source Projected onto Array Plane as a Function of Scan Plane Position

a frequency other than that for which the array was specifically designed.

2.3.1 Spatial Resolution

The resolution, or beamwidth, of the array is defined as the full width at half power or -3 dB beamwidth. Using this metric, if two sources of equal magnitude are located greater than one beamwidth apart, two peaks will appear in the resulting image. If the sources are located less than one beamwidth apart, then only one peak will appear, directly between the two sources, indicating the presence of only one source.

Rather than measuring the angular resolution, the parameter of interest for this research is the spatial resolution along the x and z dimensions of the scan plane. It is clear from figure 2.5 that to improve x and z resolution, the mainlobe of the array pattern must be made narrower in the k_p domain. In addition, it is clear that to obtain equal x and z resolution along the scan plane, the mainlobe of the array pattern must be narrower in the $k_{p,y}$ dimension than in the $k_{p,x}$ dimension. This is because $k_{p,y}$ changes much more slowly as a function of z than $k_{p,x}$ does as a function of x . In general, to create a narrow mainlobe, the array must be made larger in the dimension of interest. The results in figure 2.5 show that the array length must be greater in the y direction to obtain uniform spatial resolution. The exact ratio, determined by $\frac{|dk_{p,x}/dx|}{|dk_{p,y}/dz|}$

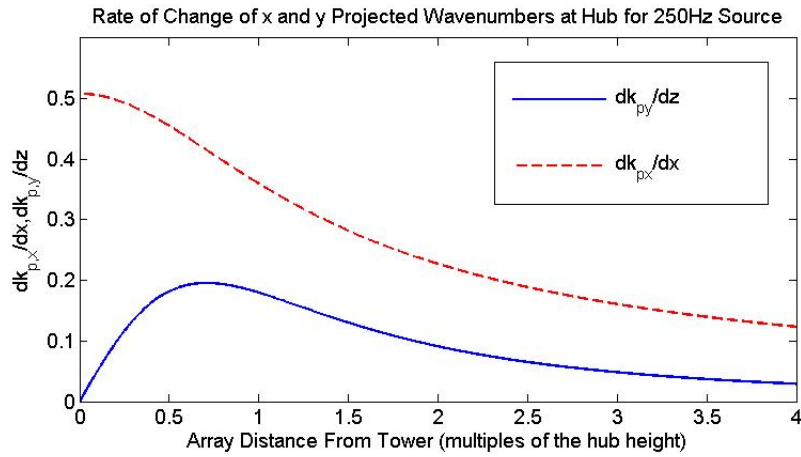


Figure 2.6: Rate of Change of Projected Wavenumbers as a Function of Array Distance from Tower

is approximately 2 for an array located one hub height away from the tower. The extent of the array must be twice as large in the y direction than in the x direction.

A question that may arise is: what is the optimal position of the array along the y axis? In other words, how far away from the scan plane should the array be located? If the objective is to optimize resolution in the x dimension, the best position for the array would be directly beneath the rotor plane. If the objective is to optimize the z dimension resolution, the best position for the array is at a distance of $1/\sqrt{2}$ of the hub height from the rotor plane. Figure 2.6 shows how quickly the projected wavenumbers from a source located at the hub change as a function of the distance between the array center and the base of the tower. The maximum rates of change are clearly illustrated as a factor of 0.7071 of the hub height for the z dimension and 0 for the x dimension. In addition, the ratio $|dk_{p,x}/dx|/|dk_{p,y}/dz|$ can be inferred to be about 2 near the optimal placement point.

The curves shown in Figure 2.6 can be misleading in terms of their direct application to array placement. One reason for this is that the physical extent of the array should remain upwind from the turbine (or downwind depending on the experiment). The directional nature of the acoustic signals drives the requirement for the sensors to all be placed in roughly one direction away from the sources. Also, the tower will block some signals if sensors are placed

on the wrong side of the tower. So placing the array very near the tower would position some sensors on the wrong side of the rotor plane. The optimal x position of the array can therefore never be achieved. Placing the array at the optimal position for the z dimension would appear to be a good trade off. However, to obtain desirable resolution at this location, some sensors could have to be positioned on the wrong side of the rotor plane as well. A good tradeoff is to position the array at a distance of one hub height away from the tower thus forming a 45° angle between the array and the hub. At this position, the z resolution is still 91.8% of the optimal value. The x resolution is 86.6% worse than at the position that is a factor of 0.7071 of the hub height and 70.7% worse than the position directly beneath the rotor. However, since the physical extent of the array should be approximately half the size in the x dimension as the y dimension, the array can easily be made slightly larger to account for the resulting degradation in resolution. Placing the array one hub height away from the tower is also somewhat of a standard as researchers at NLR used this placement in research between 2005 and 2008 [38, 39].

In addition, as will be apparent when array patterns are examined, good resolution often causes unwanted sidelobe positions to be too close to the mainlobe. Often the goal is to find a good tradeoff between resolution and sidelobe positions.

2.3.2 The Co-Array

A popular technique used to understand and reduce the sidelobe levels of an array pattern is the analysis of the *co-array* [4, 29, 49]. The co-array, C , is simply the autocorrelation function of the array shape, $C = R_{AA}(x, y)$, where R is the correlation function and A is the array shape. The array shape, A , is the sum of weighted and shifted impulse functions,

$$A = \sum_{m=0}^{M-1} w_m \delta(x - x_m, y - y_m), \quad (2.3.2.1)$$

so its autocorrelation will be the sum of M^2 shifted impulse functions. At least M of the M^2 impulse functions will be located at the origin because $R_{AA}(0, 0)$ is just the sum of the squared array shape. Therefore the co-array can consist of a maximum of $M^2 - M + 1$ unique impulse

functions. One reason that the co-array is so important is that the Fourier transform of the co-array is equal to the squared magnitude of the Fourier transform of the array shape:

$$\mathcal{F}\{C\} = \mathcal{F}\{R_{AA}(x, y)\} \quad (2.3.2.2)$$

$$= \mathcal{F}\{A(x, y) \star A(x, y)\} \quad (2.3.2.3)$$

$$= W(\vec{k})^* W(\vec{k}) \quad (2.3.2.4)$$

$$= |W(\vec{k})|^2, \quad (2.3.2.5)$$

where \star is the correlation function. The Fourier transform of the co-array will therefore be equivalent to the power of the array pattern, which is the output of the conventional beamformer.

By observing the co-array directly, some insight can be made into the efficiency of the array shape. Assuming all sensor weights, w_m , are 1, the “height” of each shifted impulse function in the co-array represents the number of sensor pairs that are the same distance and direction from each other. Co-array values with a height of more than one represent redundancies in the vectors formed between sensor pairs. The downside to this is that if a specific sensor pair happens to contribute a large amount to the beamformer output when the array is not steered toward a source, every other sensor pair separated by the same distance and direction will also contribute to the misleading beamformer output. Redundancies in the co-array can then contribute to very high sidelobe levels in the array pattern. A figure of merit for an array is the number of unique points present in the co-array, with a maximum value of $M^2 - M + 1$.

A classic example of the effect of co-array redundancies is an array consisting of a circle of evenly spaced sensors. If the number of sensors is even, almost every sensor pair will match another sensor pair that is separated by the same vector. When the number of sensors is odd, no two sensor pairs will be separated by the same distance and direction and smaller sidelobes will result. This behavior extends to evenly spaced ellipses of sensors as well. The array shapes used in this research are based on concentric ellipses. Consider the two array shapes shown in figure 2.7. They are both elliptical arrays but one has an odd number of sensors (13) while the other has an even number (14). Initially, one might predict that the array with more sensors

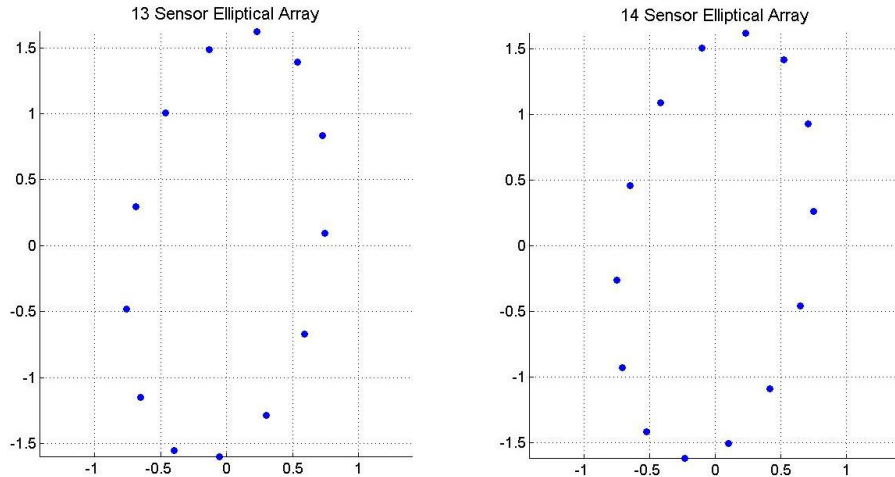


Figure 2.7: 13 and 14 Sensor Similar Array Shapes

would provide slightly better sidelobe levels until the co-arrays are examined.

A plot of the corresponding co-arrays is shown in figure 2.8. The co-arrays confirm the expected behavior for evenly spaced circular or elliptical array shapes. Most of the points in the co-array for the array with an even number of sensors have a redundancy of two, while the odd-number array's co-array has no redundancies at all. The number of unique points for the 13-sensor array is 157 out of 157 and the number of points for the 14-sensor array is only 99 out of 183. To reveal the effect of this phenomenon on the array shapes' sidelobe levels, figure 2.9 shows the results of beamforming over a scan plane centered at hub height for a 22.82 meter hub height wind turbine with a 4 kHz source at the hub. Rather than improving the array pattern, the 14 sensor array actually increases sidelobe levels over the 13 sensor array, confirming the results of the co-array analysis. Looking at the first significant “ring” of sidelobes around the mainlobe reveals that the 13-sensor array produces sidelobes that are 4.178 dB below the mainlobe. The similar ring around the mainlobe for the 14-sensor array reveals sidelobes as high as 1.899 dB below the mainlobe! Adding one additional sensor to the array harmed sidelobe rejection by a factor of 2.

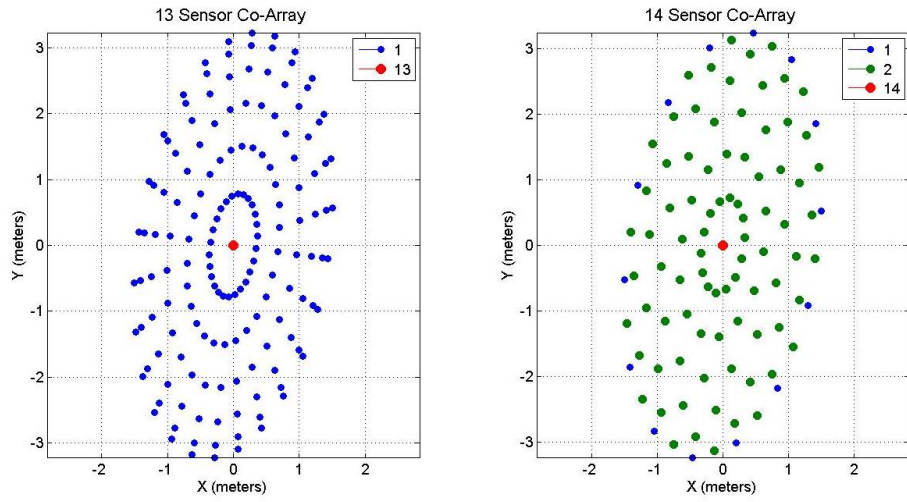


Figure 2.8: Co-Array Patterns for the 13 and 14 Sensor Array Shapes

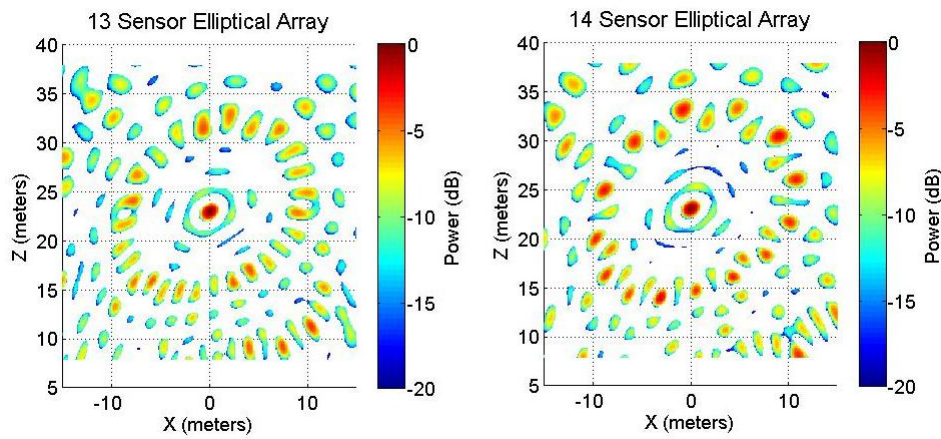


Figure 2.9: Noise maps for the 13 and 14 Sensor Elliptical Arrays

2.4 Advanced Beamforming Techniques

So far, the conventional beamformer has been introduced. This algorithm has very attractive features. It is a linear system, the array pattern is based on the Fourier transform of the array shape, and it is very predictable. A number of more advanced beamforming techniques exist that can provide better resolution and lower sidelobe values. The disadvantages of them are that they no longer behave as a linear system and in some cases can be very sensitive to array uncertainties. The “diagonal elimination” method is the simplest modification to the beamformer and is actually the standard method used throughout this research [47]. “Robust Adaptive Beamforming” is a method that adapts to the specific CSM by using the CSM information to determine the steering vector [32, 50]. Finally, the “MUSIC” algorithm proves to be a very powerful algorithm that is based on the eigen decomposition of the CSM [4, 51].

2.4.1 Diagonal Elimination

The most basic advanced beamforming technique is the diagonal elimination method. This method eliminates the diagonal of the CSM before beamforming [47]. There are two reasons for doing this. First, it will be shown in section 3.1.1 that as multiple looks at an acoustic scene get averaged together, noise is reduced on the off-diagonal CSM terms but remains unchanged on the diagonal. As will be made clear in equation 3.1.1.11, in the limit as an infinite number of looks are averaged, all noise resides on the diagonal. By eliminating the diagonal, the signal-to-noise ratio (SNR) of the beamformer can be made arbitrarily large. The second reason for eliminating the diagonal is that it does not contribute to the spatial selectivity of the beamformer. It simply adds an offset of $\frac{1}{M}$ to the normalized array pattern. This can be seen by examining the beamformer equation as the sum of “steered” CSM terms,

$$P_{k,norm} = \left(\sum_{i=1}^M A^2 + \sum_{i=1}^M \sum_{l \neq i}^M w_i e^{-j\Delta_i \omega_k} w_l e^{j\Delta_l \omega_k} A^2 e^{j\phi_i} e^{-j\phi_l} \right) / M^2. \quad (2.4.1.1)$$

The diagonal contribution, $\left(\sum_{i=1}^M A^2 \right) / M^2$, is a constant which is present at all steering locations. Eliminating this not only solves the noise problem, but also reduces sidelobe levels by

increasing the ratio of the mainlobe to a sidelobe of lesser height. When the diagonal terms are eliminated, the points on the original array pattern that were at least $10 \log(M)$ decibels below the mainlobe will be negative. Since a negative power is not physical, these points can be ignored or set to an arbitrarily low level. Diagonal elimination is implemented by applying the following mask to the CSM:

$$mask = \begin{bmatrix} 0 & 1 & 1 & \cdots & 1 \\ 1 & 0 & 1 & \cdots & 1 \\ 1 & 1 & 0 & \ddots & \vdots \\ \vdots & \vdots & \ddots & \ddots & 1 \\ 1 & 1 & \cdots & 1 & 0 \end{bmatrix}. \quad (2.4.1.2)$$

The downside to the diagonal elimination method is that the beamformer is no longer a linear system because the operation of assigning negative values to an arbitrarily low level is not a linear operator. In most cases, however, the effects this will have on the total power detected on the acoustic map will be very small. A comparison of beamforming with and without the CSM diagonal is shown in figure 2.10. The data from this experiment was collected in the field at the NWTC with a prototype array and a 1 kHz pure tone broadcast from a speaker near the hub of the 36.4 meter hub height turbine used for development. As expected, the array pattern remains roughly the same, but the sidelobes are all reduced while the mainlobe stays the same, with slightly better resolution. The dominant sidelobe near $x = 2.5$, $z = 43$ has been reduced by 0.89 dB by using diagonal elimination.

2.4.2 Robust Adaptive Beamforming

The method known as Robust Adaptive Beamforming is based on Adaptive Beamforming. Adaptive Beamforming treats beamforming as a technique where the CSM is provided and the steering vector is the variable to be chosen to provide the best output. A minimization problem is set up where the beamformer output is to be minimized with the constraint that if the array is steered directly toward a source, the output will be equal to the source's power [32, 50]. The

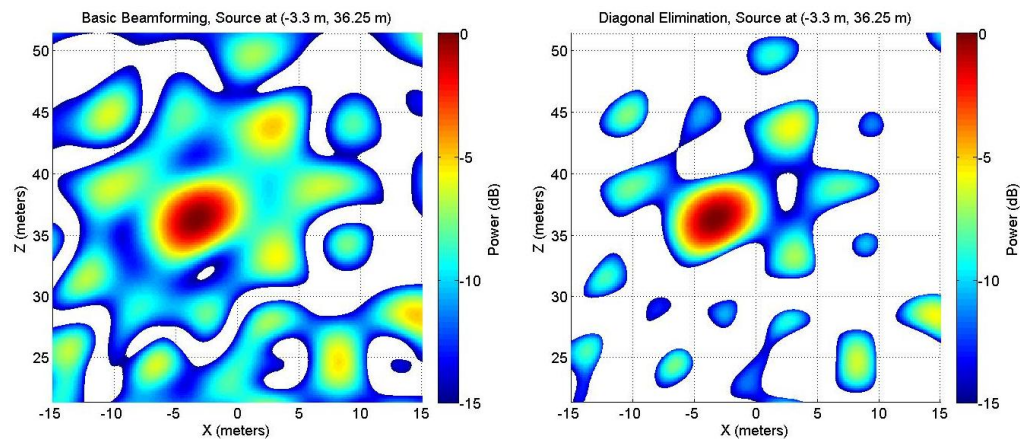


Figure 2.10: Comparison of Beamforming With and Without the Diagonal

mathematical description of this problem is

$$\min \left(w_k^\dagger \mathbf{R}_k w_k \right), \quad w_k^\dagger e_k = 1. \quad (2.4.2.1)$$

Here, w_k is the new steering vector to be chosen and e_k is the original steering vector. The new steering vector is simply used with the CSM and the constraint is that if the array is steered at the correct direction vector, the output will be unity, so that the output will be proportional to the source's power. Equation 2.4.2.1 is a classic optimization problem [4] with a solution of

$$w_k = \frac{\mathbf{R}_k^{-1} e_k}{e_k^\dagger \mathbf{R}_k^{-1} e_k}. \quad (2.4.2.2)$$

This solution is the new steering vector used in Adaptive Beamforming. This method can become unrealistic because minor errors in array sensor position assumptions or other beamforming variables (see section 3.2) result in poor Adaptive Beamforming results. Furthermore, when the CSM has a very high SNR, it becomes ill-conditioned, resulting in a poor matrix inversion operation. A way to make the technique more robust is to add a white noise term to the diagonal of the CSM. The solution in equation 2.4.2.2 becomes

$$w_k = \frac{(\mathbf{R}_k + \varepsilon \mathbf{I})^{-1} e_k}{e_k^\dagger (\mathbf{R}_k + \varepsilon \mathbf{I})^{-1} e_k}. \quad (2.4.2.3)$$

When the white noise term, ε , is very high, then $w_k \rightarrow e_k$ and the beamformer returns to the conventional beamformer. If ε is near zero, the beamformer behaves like the Adaptive Beamformer. When the steering vector in equation 2.4.2.3 is used, the beamformer is called the Robust Adaptive Beamformer, or RABF, and it is up to the signal processor to choose the value of ε that will provide the best results, since a closed form solution for ε that solves the minimization problem does not exist.

Noise maps produced by using Robust Adaptive Beamforming on the same data used in the previous section in figure 2.10 are shown in figure 2.11 for several values of ε . At very high values of ε for this problem, illustrated by the plot with $\varepsilon = 0.01$, the Robust Adaptive Beamformer produces results identical to the standard beamformer. On the other end of the range of values, when $\varepsilon = 0$, the Adaptive Beamformer produces very sloppy results. Resolution

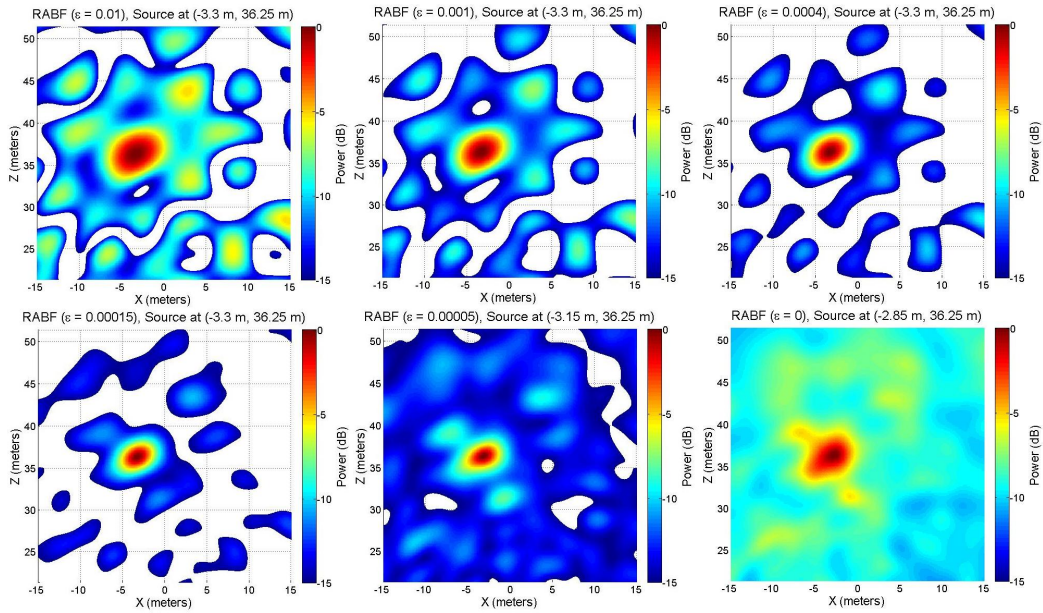


Figure 2.11: Robust Adaptive Beamforming Examples

is improved, but the location of the mainlobe has actually moved by about half of a meter and the noise floor of the image is very high. The value of ε that produces the best beamformer for this case is 0.00015. At this value, the sidelobes in the noise map have been reduced very significantly and the resolution has improved by roughly two-fold. The 4.5 meter x resolution has been reduced to 2.35 meters. This is consistent with most of the field data processed with RABF. A general rule of thumb seems to be that RABF will decrease resolution by a factor of two.

2.4.3 MUSIC

A very powerful beamforming technique that has been popular in the radio astronomy community is an algorithm called MUSIC, or MULTiple SIgnal Classification [4, 51]. This technique utilizes the eigen decomposition of the CSM into its noise and signal-plus-noise subspaces to obtain very clean looking beamforming results with sharp peaks at source locations. The method is based on the concept that the correct steering vector is very nearly an eigenvector of the CSM. In fact, when only one source exists and the CSM does not contain any noise terms,

the correct steering vector is exactly an eigenvector of the CSM. Looking back at the matrix form of the conventional beamformer, equation 2.2.0.10, it is clear that in this ideal case with one source and zero noise, the following relationship is formed when the steering vector matches the direction of propagation for a source with amplitude A :

$$e_k^\dagger (\mathbf{R}_k e_k) = e_k^\dagger (A^2 e_k) \quad (2.4.3.1)$$

$$\mathbf{R}_k e_k = A^2 e_k. \quad (2.4.3.2)$$

When the CSM contains noise or other sources are present in the scene, equation 2.4.3.2 becomes

$$\mathbf{R}_k e_k = A^2 e_k + \epsilon, \quad (2.4.3.3)$$

where ϵ is a relatively small error term. From equation 2.4.3.3, approximated by equation 2.4.3.2, it can be seen that the correct steering vector, e_k , is an eigenvector of the CSM, \mathbf{R}_k , with an eigenvalue equal to the signal power, A^2 . In general, the CSM will contain some eigenvector/eigenvalue pairs corresponding to the signals with the remaining eigenvector/eigenvalue pairs belonging to the noise subspace. In actuality, the signal eigenvector/eigenvalue pairs contain signal plus noise terms.

The MUSIC algorithm surprisingly does not use the signal plus noise subspace of the CSM but instead relies completely on the noise subspace. The idea is that if there are L sources, then there will be L eigenvectors corresponding to the signal-plus-noise subspace and $M - L$ eigenvectors corresponding to the pure noise subspace, where M is the number of sensors. A new CSM is formed, consisting of only the noise eigenvectors. Since eigenvectors are orthogonal vectors, this new CSM should give very small outputs at the actual source locations when used in the beamformer. Since the output of the beamformer with the new CSM will yield the inverse of the desired power, its inverse is simply used when plotting the noise map. The very low values corresponding to source locations will then become manifest as peaks in the noise map. Since a CSM is a Hermitian, positive-definite matrix, its inverse will have the same eigenvectors as the original with eigenvalues that are inverses of the original values. Since the eigenvalues will be

the same, the new CSM generated from the noise subspace is referred to as the inverse of the CSM: $\mathbf{R}_{k,MUSIC}^{-1}$.

$\mathbf{R}_{k,MUSIC}^{-1}$ is formed by first ordering the eigenvector/eigenvalue pairs of the CSM by increasing eigenvalue. The signal terms will have large eigenvalues and the noise terms will have very small eigenvalues. A threshold value must be decided upon that will determine which eigenvalues correspond to sources. The eigenvectors that belong to the L sources decided upon will not be included in $\mathbf{R}_{k,MUSIC}^{-1}$ but the rest will. The new CSM is calculated as

$$\mathbf{R}_{k,MUSIC}^{-1} = \sum_{i=1}^{M-L} v_i v_i^\dagger, \quad (2.4.3.4)$$

where v_i is the i^{th} eigenvector. Note that in this definition of the inverse matrix, all noise terms are given eigenvalues of 1, thereby “whitening” the noise [4]. This tends to give the noise maps a constant noise floor level from which the source locations are lifted. The final step in calculating the output of the MUSIC beamformer is to multiply $\mathbf{R}_{k,MUSIC}^{-1}$ with the steering vector in quadratic form and take the inverse:

$$P_{k,MUSIC} = \left(e_k^\dagger \mathbf{R}_{k,MUSIC}^{-1} e_k \right)^{-1}. \quad (2.4.3.5)$$

An example of the beamformer output when using the MUSIC algorithm is provided in figure 2.12. For a good comparison, this example uses the same data collected in the field that the diagonal elimination and Robust Adaptive beamforming examples used. For this example, it was assumed that only one source existed, which is approximately true because the dominant source was the speaker positioned near the turbine hub. As a result, the MUSIC algorithm used $M-1$ or 15 noise eigenvectors to form $\mathbf{R}_{k,MUSIC}^{-1}$. It is apparent that the MUSIC algorithm tends to lift the source positions up from a relatively constant noise floor, although the faint array pattern can seen.

MUSIC works best if there are fewer point sources in the scene than sensors in the array. This way, the noise subspace will not be empty. Initial simulations of MUSIC involved a number of point sources less than the number of sensors, so MUSIC worked exactly as it should in theory. In an experimental setting, the acoustic scene can be modeled as many point

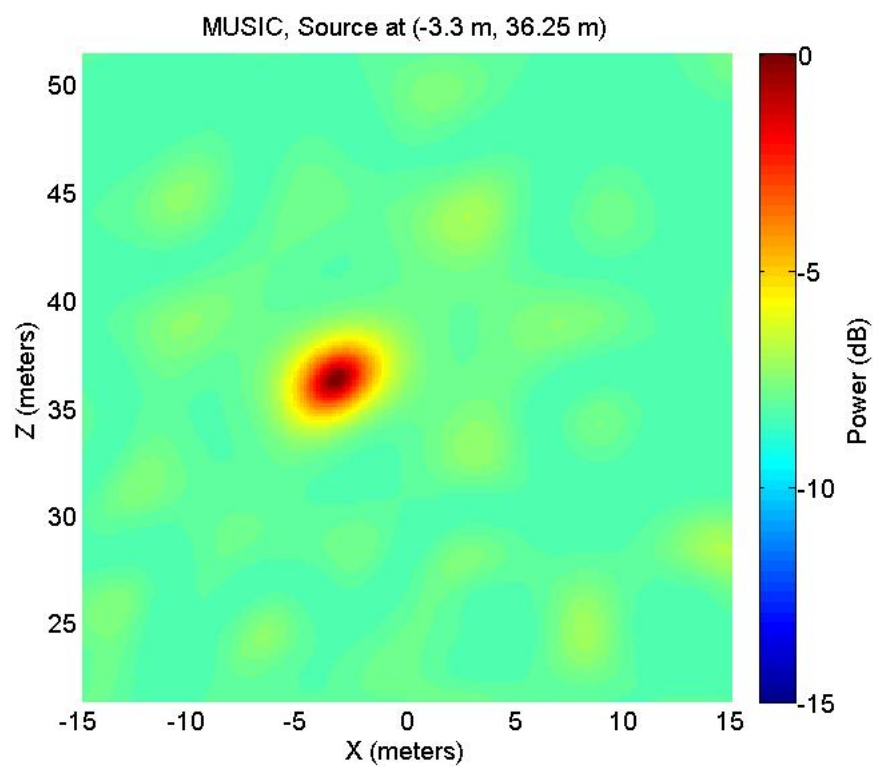


Figure 2.12: MUSIC Example

sources. The number of point sources could be greater than the number of sensors in the array, in which case each eigenvector no longer corresponds to a steering vector for exactly one point source. In this case, the physical meaning of the eigenvectors becomes more complicated and the effectiveness of MUSIC is unknown.

The diagonal elimination technique is part of the standard beamforming algorithm used in this research. The failures and successes of applying RABF and MUSIC to aeroacoustic observations in the field will be discussed more in section 5.2.3.1.

Chapter 3

Practical Acoustic Array Considerations

When using an array in the field, several sources of error can exist. Wind noise as well as electronic noise inherent to the system can corrupt measurements. Atmospheric turbulence can distort the wavefronts differently for each signal path. Of course, sensor positions in the field cannot be measured perfectly and these uncertainties will harm the beamformer performance. The distance between the array and the plane containing the sources is not always known perfectly. For example, blade tip deflection could cause blade sources to move out of the rotor plane or gearbox noise several meters behind the rotor could be detected. Furthermore, uncertainties in the speed of sound, or equivalently, the signal wavelengths can cause beamforming errors. A related concern is that the speed of sound will change depending on both the wind speed and which direction the sound is travelling compared to the wind direction. In addition, wind shear will affect the way acoustic signals travel through the atmosphere. Finally, Doppler shifts, due to the rotating nature of the blade sources, change the phase relationships between sensor pairs. This chapter explains all of the major sources of error and includes a discussion of the effects they have on beamformer performance. Reasonable bounds on how much uncertainty can exist are provided for most of the error sources.

3.1 Characterization of Corruptive Noise

The array microphone signals are subject to corruptive noise from several sources. The primary source is unwanted wind noise, which tends to dominate thermal noise from the data

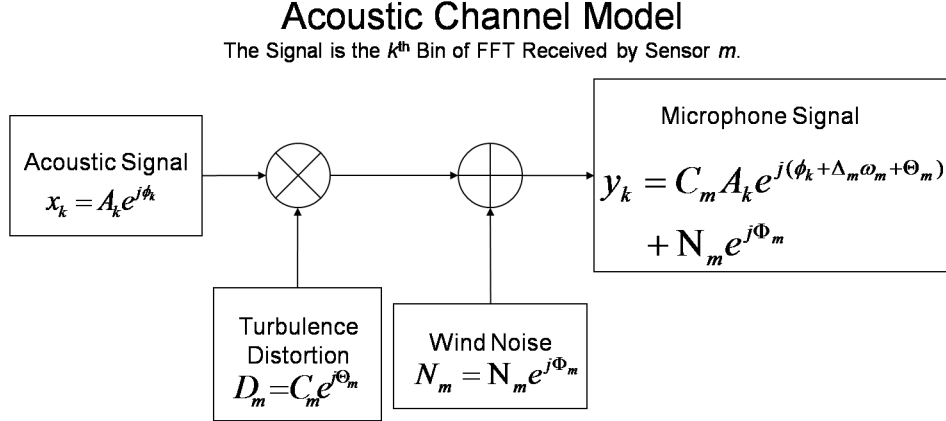


Figure 3.1: Acoustic Transmission Model

acquisition system. Wind noise can be modeled as additive white Gaussian noise when received by the system. Another source of corruption is atmospheric turbulence which varies the local refractive indices of paths between sources and sensors. The turbulence varies greatly between a source and the different paths to the sensors. Turbulence can have the effect of increasing or decreasing both the speed of an acoustic signal or its amplitude received at the sensor.

As discussed in section 2.2, the desired “signal” used in beamforming is the CSM which contains information about the phase difference between each pair of sensors at a given frequency as well as the cross powers of the signals in that frequency bin. The different turbulent distortions of the signals between the source and the sensors can cause phase distortion and amplitude distortion. This phase and amplitude distortion is not a white noise and therefore should be treated differently than the additive wind noise. Assuming that the signal of interest is the k^{th} bin of the FFT performed on the microphone signal, the desired signal is a complex number containing amplitude and phase information. A discrete frequency domain model of the channel through which this signal propagates is shown in figure 3.1. This channel models the transmission of the k^{th} frequency bin from the source to microphone m . The uncorrupted received signal would be $A_k e^{j(\phi_k + \Delta_m \omega_m)}$, after normalization for propagation loss.

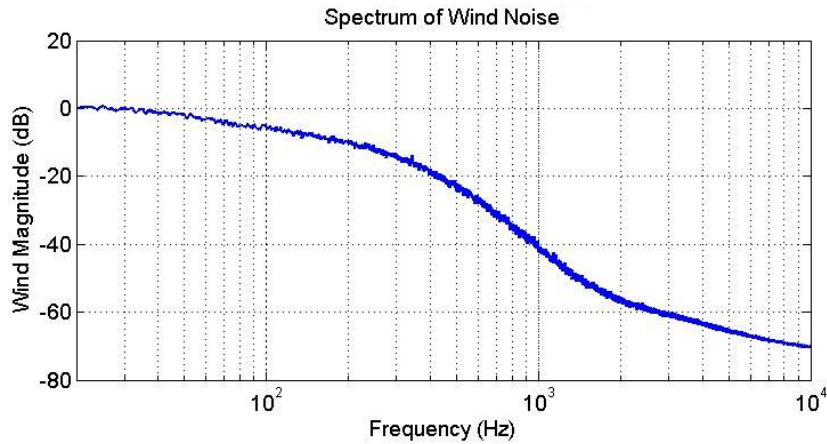


Figure 3.2: Wind Noise Spectrum

3.1.1 Wind Noise and Array Gain

Additive wind noise received by the sensors has a spectral shape with higher energy density in the lower frequencies. A plot showing the spectral shape of wind noise, estimated from two minutes of wind data, is provided in figure 3.2. The spectrum can be divided into three different regions. For frequencies less than 350 Hz, the spectrum decays at about 10 dB/decade. For frequencies between 350 Hz and 1.5 kHz, the noise decays at 60 dB/decade. For higher frequencies, the slope is about 20 dB/decade. The noise has been shown to be uncorrelated between sensors and an analysis is given in section 3.1.2. If the only source of noise is wind noise that is uncorrelated between sensors, it can be shown that an array of M sensors, with uniform array shading will increase the signal-to-noise ratio (SNR) of the system by a factor of M . The factor by which SNR is improved is known as *array gain* or G [4].

The power determined by the conventional beamformer given in eq. 2.2.0.10 with a

signal-plus-noise input can be expanded as

$$P_k = \sum_{i=1}^M \sum_{l=1}^M w_i e^{-j\Delta_i \omega_k} w_l e^{j\Delta_l \omega_k} (A e^{j\Delta_i \omega_k} + N_i e^{j\Phi_i}) (A e^{-j\Delta_l \omega_k} + N_l e^{-j\Phi_l}) \quad (3.1.1.1)$$

$$= \sum_{i=1}^M \sum_{l=1}^M w_i w_l A^2 + \quad (3.1.1.2)$$

$$\begin{aligned} & \sum_{i=1}^M \sum_{l=1}^M w_i e^{-j\Delta_i \omega_k} w_l e^{j\Delta_l \omega_k} (A N_l e^{j(\Delta_i \omega_k - \Phi_l)} + A N_i e^{j(\Phi_i - \Delta_l \omega_k)} + N_i N_l e^{j(\Phi_i - \Phi_l)}) \\ &= \sum_{i=1}^M \sum_{l=1}^M w_i w_l A^2 + \sum_{i=1}^M w_i^2 (A N_i \cos(\Delta_i \omega_k - \Phi_i) + N_i^2) + \quad (3.1.1.3) \\ & \sum_{i=1}^M \sum_{l \neq i}^M w_i e^{-j\Delta_i \omega_k} w_l e^{j\Delta_l \omega_k} (A N_l e^{j(\Delta_i \omega_k - \Phi_l)} + A N_i e^{j(\Phi_i - \Delta_l \omega_k)} + N_i N_l e^{j(\Phi_i - \Phi_l)}). \end{aligned}$$

The SNR of the beamformer from equation 3.1.1.3 is

$$\begin{aligned} SNR_{P_k} &= \frac{E \left[\sum_{i=1}^M \sum_{l=1}^M w_i w_l A^2 \right]}{E \left[\sum_{i=1}^M w_i^2 (A N_i \cos(\Delta_i \omega_k - \Phi_i) + N_i^2) + \sum_{i=1}^M \sum_{l \neq i}^M w_i e^{-j\Delta_i \omega_k} w_l e^{j\Delta_l \omega_k} \right] \cdots} \\ &\cdots \cdot \frac{\cdots}{(A N_l e^{j(\Delta_i \omega_k - \Phi_l)} + A N_i e^{j(\Phi_i - \Delta_l \omega_k)} + N_i N_l e^{j(\Phi_i - \Phi_l)})}. \quad (3.1.1.4) \end{aligned}$$

Since the cross terms are uncorrelated and zero-mean and $\cos(\Delta_i \omega_k - \Phi_i)$ is uncorrelated for all i and zero-mean, the summation of these terms tends toward zero and the SNR becomes

$$SNR_{P_k} = \frac{E \left[\sum_{i=1}^M \sum_{l=1}^M w_i w_l A^2 \right]}{E \left[\sum_{i=1}^M w_i^2 N_i^2 \right]}, \quad (3.1.1.5)$$

$$= \frac{A^2 \left(\sum_{i=1}^M w_i \right)^2}{E [N^2] \sum_{i=1}^M w_i^2}. \quad (3.1.1.6)$$

Since the single sensor SNR is given as $SNR_{Sensor} = \frac{A^2}{E[N^2]}$, the array gain, G, is

$$G = \frac{SNR_{P_k}}{SNR_{Sensor}} = \frac{\left(\sum_{i=1}^M w_i \right)^2}{\sum_{i=1}^M w_i^2}. \quad (3.1.1.7)$$

If all sensor weights are chosen to be equal, then the array gain is M.

When beamforming in practice, the SNR is usually higher than $M \cdot SNR_{Sensor}$. The reason for this is that instead of simply beamforming with the CSM \mathbf{R}_k obtained from one FFT block, the CSM $\hat{\mathbf{R}}_k$, introduced in section 2.2, is used, which is an estimation of the mean values of the CSM from N blocks of data. To realize how the estimate $\hat{\mathbf{R}}_k$ improves SNR, the single block ($N = 1$) $\hat{\mathbf{R}}_k$ will be analyzed. An arbitrary element of the CSM, $\hat{\mathbf{R}}_{k,i,l,N=1}$, with signal

plus additive wind noise can be represented as

$$\hat{\mathbf{R}}_{k,i,l,N=1} = (Ae^{j\Delta_i\omega_k} + N_i e^{j\Phi_i}) (Ae^{-j\Delta_l\omega_k} + N_l e^{-j\Phi_l}) \quad (3.1.1.8)$$

$$= A^2 e^{j(\Delta_i\omega_k - \Delta_l\omega_k)} + AN_l e^{j(\Delta_i\omega_k - \Phi_l)} + AN_i e^{j(\Phi_i - \Delta_l\omega_k)} \dots$$

$$\dots + N_i N_l e^{j(\Phi_i - \Phi_l)}. \quad (3.1.1.9)$$

For the case where $i \neq l$, the noise terms, $AN_l e^{j(\Delta_i\omega_k - \Phi_l)} + AN_i e^{j(\Phi_i - \Delta_l\omega_k)} + N_i N_l e^{j(\Phi_i - \Phi_l)}$,

incoherently add in the CSM element estimate

$$\hat{\mathbf{R}}_{k,i,l} = \frac{1}{N} \sum_{n=1}^N (A^2 e^{j(\Delta_i\omega_k - \Delta_l\omega_k)} + AN_l e^{j(\Delta_i\omega_k - \Phi_l)} + AN_i e^{j(\Phi_i - \Delta_l\omega_k)} + N_i N_l e^{j(\Phi_i - \Phi_l)}), \quad (3.1.1.10)$$

increasing the SNR of the CSM element to $SNR_{i,l,N} = N \cdot SNR_{i,l}$.

For the case where $i = l$, the noise term in equation 3.1.1.9 reduces to $2AN_i e^{j(\Delta_i\omega_k - \Phi_i)} + N_i^2$. For multiple blocks of data, the $2AN_i e^{j(\Delta_i\omega_k - \Phi_i)}$ terms will incoherently add, reducing their contribution to noise by N . The term N_i^2 will converge to $E[N^2]$ however. The result is that the noise terms in

$$\lim_{N \rightarrow \infty} \frac{1}{N} \sum_{n=1}^N \mathbf{R}_{k,n} = \begin{bmatrix} A^2 + E[N^2] & A^2 e^{j\omega_k(\Delta_1 - \Delta_2)} & \dots & A^2 e^{j\omega_k(\Delta_1 - \Delta_M)} \\ A^2 e^{j\omega_k(\Delta_2 - \Delta_1)} & A^2 + E[N^2] & \dots & A^2 e^{j\omega_k(\Delta_2 - \Delta_M)} \\ \vdots & \vdots & \ddots & \vdots \\ A^2 e^{j\omega_k(\Delta_M - \Delta_1)} & A^2 e^{j\omega_k(\Delta_M - \Delta_2)} & \dots & A^2 + E[N^2] \end{bmatrix} \quad (3.1.1.11)$$

all reside on the diagonal. Thus the best that can be accomplished through conventional beamforming is the isolation of noise to M out of the M^2 CSM elements. The SNR of the beamformer is therefore limited to $M \cdot SNR_{Sensor}$. If the diagonal is eliminated, though, SNR can in theory be infinite. This technique was investigated in section 2.4.

3.1.2 Correlation of Wind Noise

As mentioned previously, the complex additive wind noise term in the acoustic channel model is treated as being uncorrelated between microphones. In addition, this noise is treated as being spectrally white, having no correlation in the time domain. To analyze the validity

of these assumptions, a 60 second dataset was taken with the array set up in the field in a 6 m/s wind with the turbine stopped. The correlation of noise was analyzed at four inter-sensor distances: 0.5 m, 2.5 m, 9.5 m, and 38 m. The line formed between the chosen sensor pairs was parallel to the local wind direction to increase the chances of noticing any correlation. To look at frequency dependencies possible correlations might have, five frequencies were analyzed at each inter-sensor distance: 50 Hz, 100 Hz, 500 Hz, 1 kHz, and 5 kHz, indicative of the range of frequencies that is observed in field testing.

The method used to detect any correlation between the sensor pairs was to create a histogram of the phase differences of the received signals between sensors i and l , modeled as $\angle\{N_i N_l e^{j(\Phi_l - \Phi_i)}\}$. Any strong deviation from a uniform distribution of phases would imply a correlation of the wind noise, violating the assumptions made in 3.1.1 and degrading the derived array factor. The histograms contain 732 FFT blocks of 2048 samples (0.082 seconds) with a Hanning window applied. Results of the analysis are shown in figure 3.3. Note that the distributions are relatively uniform for all inter-sensor distances and frequencies with a possible exception at 0.5m at 500Hz. Such a small microphone separation would never be used at frequencies as low as 500Hz however. The additive wind noise term can therefore be treated as a circularly symmetric complex Gaussian random variable (independent real and imaginary parts).

To determine whether there is any significant correlation between time-adjacent phase differences between sensors, the n^{th} phase difference is compared to the $n-1^{th}$ phase difference, where n refers to the n^{th} FFT block from 1 to 732. This method detects if there are any significant low frequency contributions to the spectrum $\Phi_{il}(f) = \mathcal{F}\{\Phi_l(t) - \Phi_i(t)\}$. Histograms of the 731 phase differences for all inter-sensor spacings and frequencies are shown in figure 3.4. The relatively uniform distribution of time-domain differences in phases suggests that the magnitude of $\Phi_{il}(f)$ is reasonably white. Therefore $\Phi_l(t_1) - \Phi_i(t_1)$ and $\Phi_l(t_2) - \Phi_i(t_2)$ will be treated as independent for all t_1 and t_2 . To verify that the k^{th} FFT bin of a sample of wind noise is indeed a circularly symmetric complex Gaussian, the phase must be uniformly distributed and

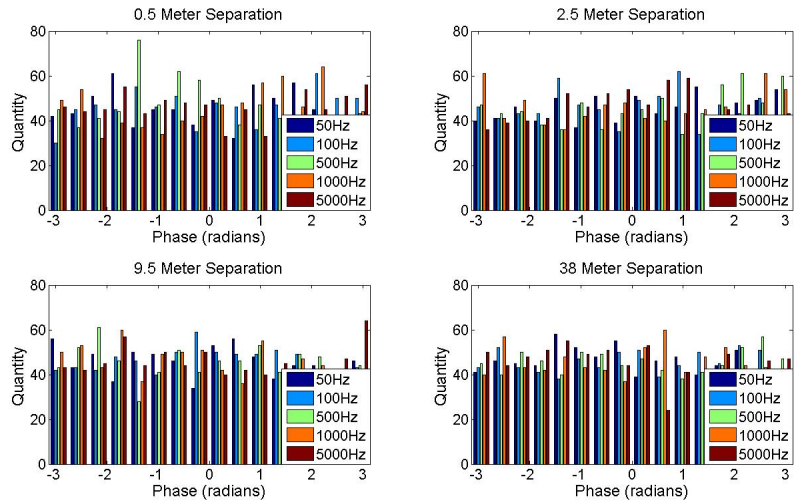


Figure 3.3: Histograms of Inter Sensor Phase Differences for Wind Noise

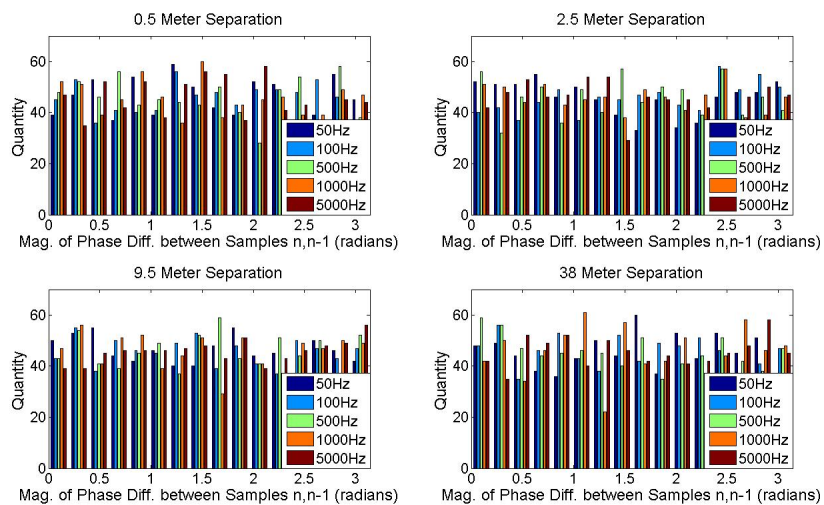


Figure 3.4: Histograms of Variations in Time-Adjacent Inter-Sensor Phase Differences

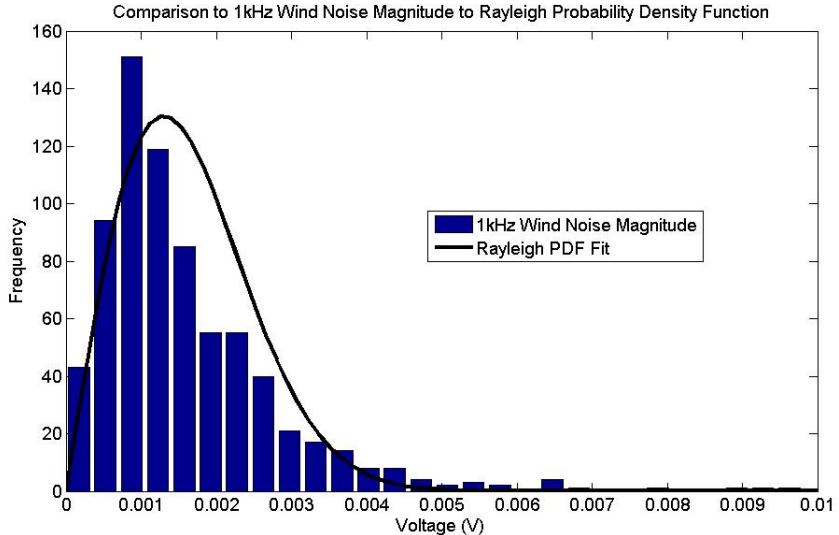


Figure 3.5: Comparison of 732 Samples of 1kHz Wind Noise Magnitude over 60 Seconds with Rayleigh Probability Density Function

the magnitude must be distributed as a Rayleigh random variable [52]. The uniform phase has already been suggested. To reveal that the magnitude is approximately Rayleigh distributed, a comparison of the histogram of the magnitude of 1 kHz wind noise with a Rayleigh probability density function of the same mean is shown in figure 3.5.

3.1.3 The Effect of Atmospheric Turbulence on Signal Estimation

Observations have shown that the multiplicative noise term in figure 3.1 distorts the CSM elements so that they no longer contain circularly symmetric noise with a mean value corresponding to the correct phase and magnitude. Instead, it appears that the distortion caused by this term tends to effect the phase of the estimate more than the magnitude. This stretching of the phase can be seen in figure 3.6 for the cross power of the FFT bin corresponding to 3 kHz for two sensors. The plot shows individual complex frequency domain cross powers for each 41 millisecond block of data in a four minute period. The experiment involved placing the two sensors 5 meters apart from each other and positioning a speaker on a step ladder over 25 meters away, in the direction perpendicular to the sensor separation. A very strong 3 kHz pure

tone was broadcast so that the speaker signal would be dominant over any wind noise that may occur.

The data in figure 3.6 is plotted as a function of the real and imaginary parts of the cross spectral powers and the mean value of the phase is illustrated by the angle formed between the positive real axis and the black line. Two different estimates of the magnitude of the CSM element are shown on the line. The yellow point represents the magnitude that would result from using the traditional CSM estimate from equation 2.2.0.13: $\hat{\mathbf{R}}_k = \frac{1}{N} \sum_{n=1}^N Y_{k,n} Y_{k,n}^\dagger$. This estimate results in the correct phase estimate but with a magnitude estimate that is less than the actual mean value of the magnitude. The underestimated magnitude results because the estimate is using the center of mass of all of the data points as the estimate. The curved shape of the CSM elements leads to a center of mass that is too close to the origin. A better estimator would result in the magnitude estimate represented by the green point, which is the actual mean value of the magnitude. The improved CSM estimator estimates the phase and magnitude separately and is given by

$$\hat{\mathbf{R}}'_k = \left(\frac{1}{N} \sum_{n=1}^N |Y_{k,n} Y_{k,n}^\dagger| \right) \exp \left(j \left(\frac{1}{N} \sum_{n=1}^N \angle(Y_{k,n} Y_{k,n}^\dagger) \right) \right). \quad (3.1.3.1)$$

A potential problem with trying to obtain a good estimate of the CSM in the presence of atmospheric turbulence is that the phase corruption is not a white noise [53, 54, 55]. Each estimate of the phase distortion is not independent from the other estimates. A qualitative example of this behavior is presented in figure 3.7, where the phase difference between two sensors with the mean value removed is plotted against time using a strong tonal signal at 250 Hz for 4 minutes and 30 seconds. The sensors are separated by a very large amount to stress the behavior and the phase curve has been low-pass filtered to eliminate the high frequency variation, yielding only the slowly changing turbulent distortion. Obviously, the phase noise is very correlated with itself. For this reason, it becomes very important to collect data for a long time when forming a CSM estimate. For example, if only data collected between 40 and 70 seconds were used from figure 3.7, the phase estimate would be somewhere between 0.5

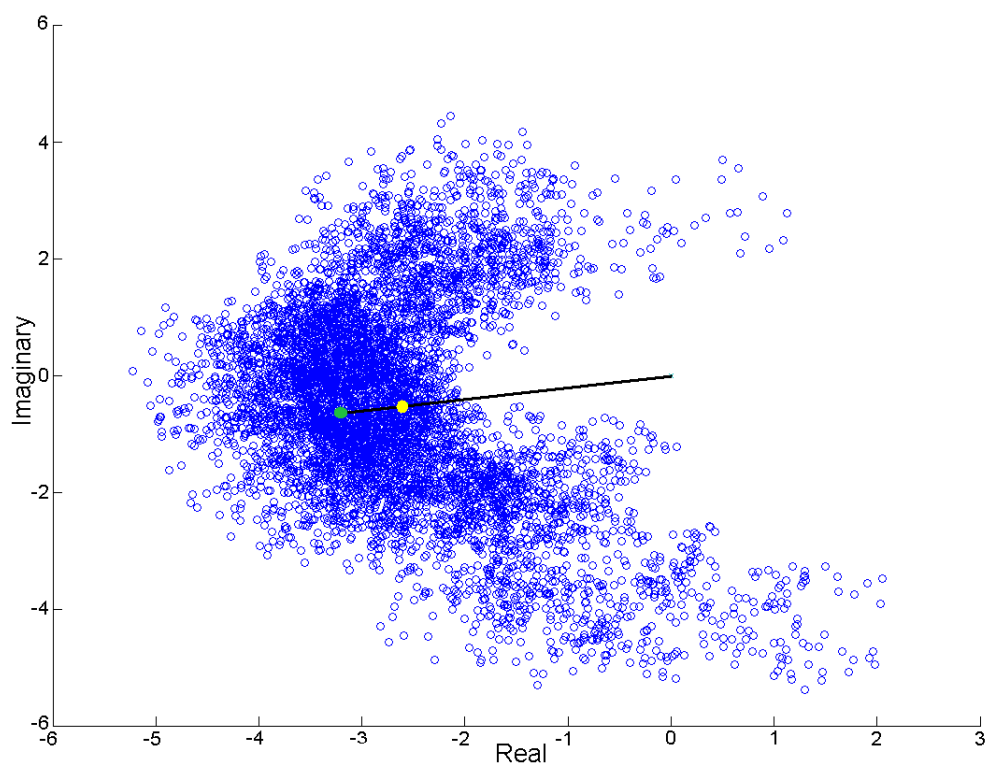


Figure 3.6: Cross Spectral Power Distortion Example

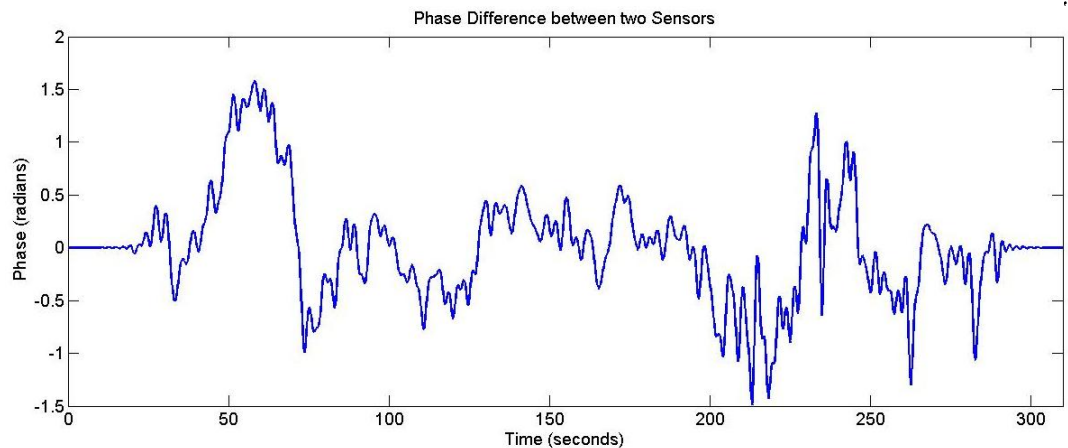


Figure 3.7: Phase Distortion Example

radians and 1 radian too high. This kind of error could become unacceptable, especially when compounded with sensor position and other errors.

Evidence that the non-white phase distortion is due to turbulent atmospheric effects is seen when observing the statistics of the phase distortion as a function of how far apart the sensors are located. To examine this dependence, a test was set up using an aerial lift to position a speaker near the hub of the 36.4 meter hub height turbine used for array prototyping at the NWTC. A prototype array was set up on the ground centered 36.4 meters away from the tower base. The array consisted of 24 microphones spanning an area of 18 meters-by-36 meters. Rather than examining the statistics as a function of the sensor separation on the ground, the angle formed between the source and the sensor pair was used. The idea is that the angle formed between the source and sensors would be more indicative of how different the atmospheric conditions are between the signal paths. Four minutes and 30 seconds of data were used for the experiment and once again a very strong tonal signal at 250 Hz was used to attempt to dominate the wind noise. Two statistics are examined for the phase distortion. First, the standard deviation of the phase from its mean value is plotted against angular sensor separation. This gives a general idea of the amount of distortion that occurs. Second, the *e*-folding time of the decorrelation of the low-pass filtered phase curves are examined. This statistic measures

the amount of time it takes for the autocorrelation of each phase curve to become reduced by a factor of e from its value at $t = 0$. This statistic can give a good feel for how long it takes for CSM estimates to become probabilistically independent. Both of these statistics are shown in figure 3.8.

Interestingly, there are apparent trends in both standard deviation of phase error and decorrelation time. The farther apart any two sensors are, the higher the magnitude of the phase error will be and the errors will become correlated for longer periods of time. A very linear trend is present in the plot of the standard deviation. Here, the slope of the trend line is roughly 0.014 radians (or 0.8 degrees) of average phase error per degree of angular separation between sensors from the source. Although a trend is clearly visible for the decorrelation times, it is unknown whether the trend is linear or logarithmic in shape. A conjecture is that once the paths travelled from the source to the sensors are far enough apart, the atmospheric turbulence becomes completely independent and the decorrelation time will plateau at a certain value. In this experiment, it is possible that the asymptotic decorrelation time is around 11 seconds. Whatever the trend of the correlation is, it is clear that when using an acoustic array in the field, it is reasonable to expect to have to wait close to 10 seconds before treating the noise terms in microphone samples as independent.

It should be mentioned that the frequency of the acoustic signal used to generate the trends in figure 3.8 is somewhat arbitrary. If the frequency is changed, the decorrelation times will remain unchanged. If the frequency is doubled, the standard deviation of the phase errors will double. Likewise, a lower frequency would produce even lower phase errors. A signal at 250 Hz was chosen for this experiment because the atmospheric phase distortion dominated over the wind noise but the distortion was low enough that it was still easy to unwrap the phase to produce a clean looking plot without discontinuities.

The atmospheric turbulence does not directly distort the phase of the acoustic signals but rather alters the local speed of sound, c , differently for each signal path. The phase difference between sensors is the difference between the number of wavelengths separating each sensor and

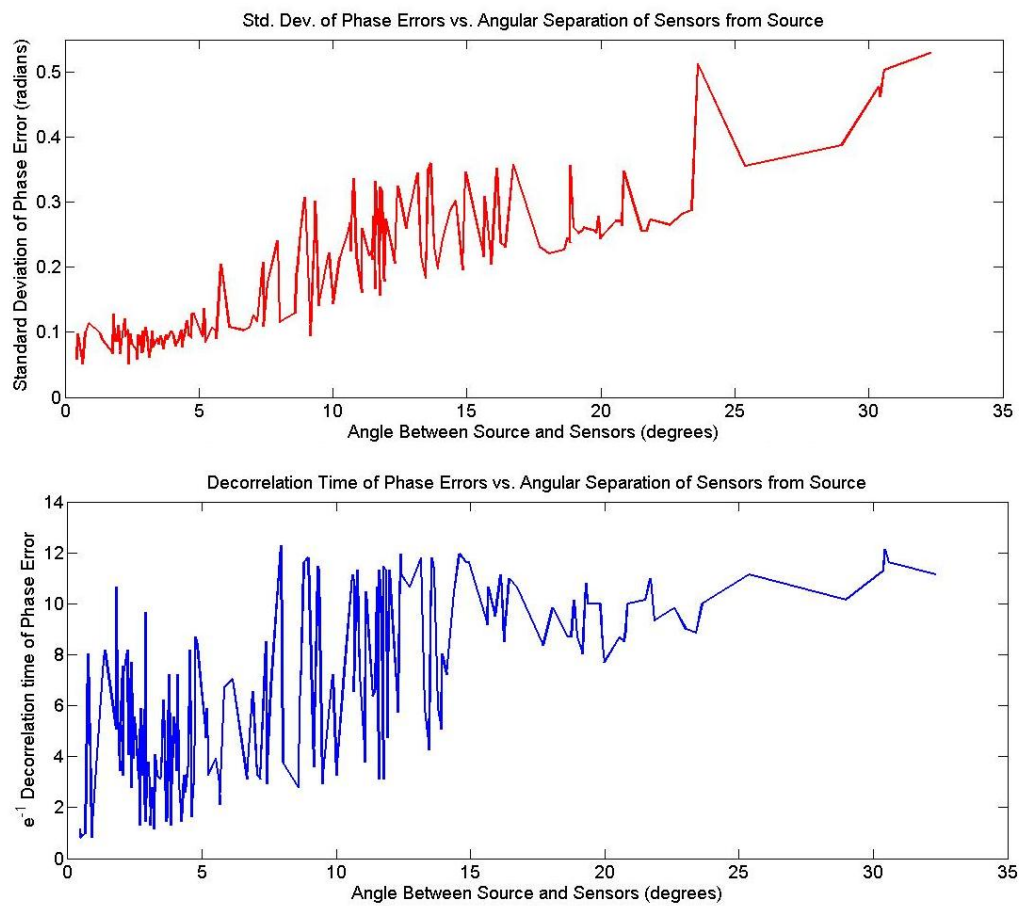


Figure 3.8: Phase Statistics as a Function of Inter-sensor Distance

the source. The number of wavelengths is given by $distance/\lambda = distance \cdot f/c$. So it is really c that becomes distorted due to turbulence and the phase distortion scales linearly with f . The actual number of wavelengths travelled by the signal from source to sensor is given by

$$\#\lambda = f \left| \int_{\vec{x}(source)}^{\vec{x}(sensor)} \frac{1}{c(\vec{x})} d\vec{x} \right|. \quad (3.1.3.2)$$

When the atmosphere is completely stable, c is just a constant value and equation 3.1.3.2 reduces to $distance \cdot f/c$. When a turbulent atmosphere exists, it is the integral over the path from source to sensor of $\frac{1}{c}$ that results in the phase distortion.

The CSM estimate consists of a phase and a magnitude, so the next logical step is to investigate the trends of the magnitude distortion as a function of inter-sensor spacing. Is there any correlation between magnitude error and signal path separation? The standard deviation (in dB) and e -folding time trends for the magnitude term in the cross powers are plotted in figure 3.9. No clear trends result from these analyses although one could argue that a somewhat upward trend exists for the decorrelation time. Since no trends are observed, it can be concluded that magnitude distortion is not a concern when deciding how far apart sensors can be placed in the field.

More data is needed to investigate the dependence of the phase distortion statistics on atmospheric conditions. This experiment was conducted at 11:40 AM in May, with a temperature of about 21° C (70° F), an average wind speed of 3.8 m/s at a height of 10 m, and an average turbulence intensity of 0.2. It should be noted that although the five-minute average turbulence intensity was 0.2, one-minute turbulence intensity averages during the experiment ranged from 0.1 to 0.34. The average wind direction during the test was from the south, so the wind was transverse to the sound propagation direction. Because the experiment was performed during the day, the atmospheric boundary layer can be treated as unstable. If the array were to be used after sunset, the boundary layer would be more stable and the turbulent distortion effects would probably be less severe. This is something to consider when very large array shapes are necessary to obtain enough resolution but phase distortion becomes too much of a problem

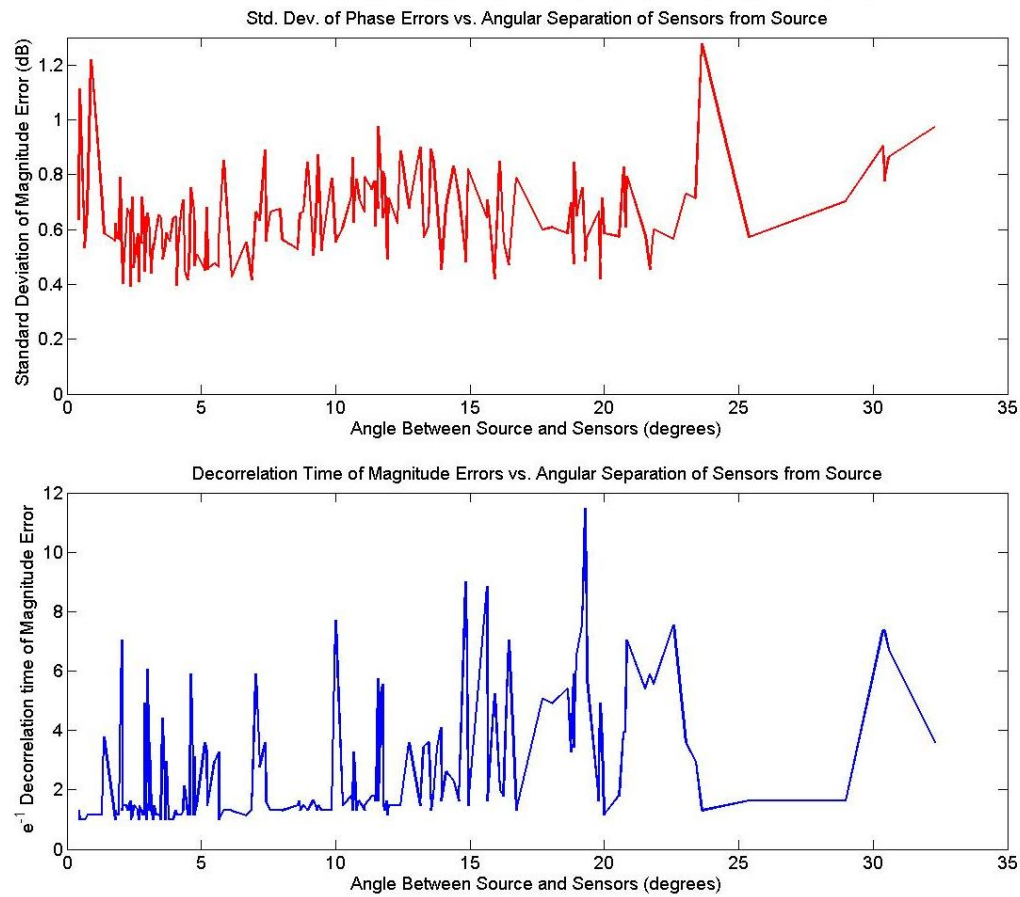


Figure 3.9: Cross Power Statistics as a Function of Inter-sensor Distance

during the day.

3.2 Uncertainty in Beamformer Parameters

In order to bound the uncertainty in the sound pressure levels (SPLs) determined by beamforming, it is important to understand the uncertainties in the beamformer parameters, bound the input uncertainties, then determine the bounds on the output uncertainties such as SPL and source location [56]. The primary input parameters to the beamformer are the microphone positions, the y distance from the array to the scan plane (see fig. 2.1), the speed of sound, which depends on temperature, and the frequency of the signal under investigation. These four uncertainties will be investigated and their effects on beamformer output values will be determined. First, the effects of sensor position uncertainties will be analyzed and appropriate bounds on placement uncertainties will be formed.

3.2.1 Sensor Position Uncertainties

Once again, the power detected by the beamformer will be written as the sum of the M^2 cross powers. This time, a phase error, ϵ_i , is introduced at each sensor due to sensor placement errors:

$$P_k = \sum_{i=1}^M \sum_{l=1}^M w_i e^{-j\Delta_i \omega_k} w_l e^{j\Delta_l \omega_k} A^2 e^{j\phi_i + \epsilon_i} e^{-j\phi_l + \epsilon_l}. \quad (3.2.1.1)$$

A look at the beamformer output when the array is correctly steered toward a source will be taken. In this case, $\phi_i = \Delta_i \omega_k$ and the output power equation reduces to

$$P_k = A^2 \sum_{i=1}^M \sum_{l=1}^M e^{j(\epsilon_i - \epsilon_l)}. \quad (3.2.1.2)$$

This can be reduced further using the Hermitian properties of the CSM and the fact that the trace reduces to MA^2 . The correctly steered output can be written as the sum of the trace and the real components of the lower triangle:

$$P_k = MA^2 + 2A^2 \sum_{i=2}^M \sum_{l=1}^{i-1} \cos(\epsilon_i - \epsilon_l). \quad (3.2.1.3)$$

Direction of Arrival, Wavelength = λ_p

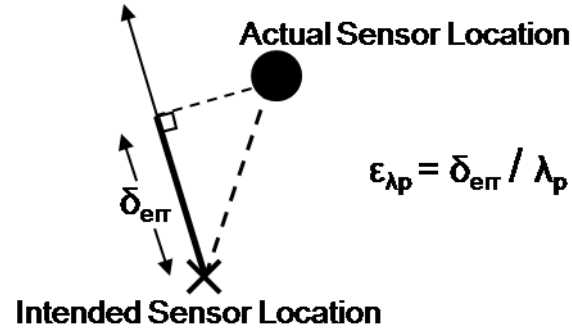


Figure 3.10: Sensor Position Error

It is much more useful to transform the error variables into a percentage of the source wavelength projected onto the xy array plane. More specifically, the new error variable $\varepsilon_{\lambda_p,i}$ is the percentage of a wavelength the sensor location is in err by in the direction of arrival of the source. A positive value indicates an offset toward the source while a negative value refers to a placement farther away from the source than the intended position. This way the error represents a physical offset of the sensor from its intended position (see figure 3.10). Equation 3.2.1.3 then becomes

$$P_k = MA^2 + 2A^2 \sum_{i=2}^M \sum_{l=1}^{i-1} \cos(2\pi(\varepsilon_{\lambda_p,i} - \varepsilon_{\lambda_p,l})). \quad (3.2.1.4)$$

Statistics on the error in the estimate of the absolute SPL can be based on equation 3.2.1.4. A simple yet extremely useful upper bound on the error in SPL can be derived by assuming that the error in sensor placement is no more than $\lambda_p/16$ where λ_p is the projected wavelength of the source onto the array plane. In this case, if the magnitudes of $\varepsilon_{\lambda_p,i}$ and $\varepsilon_{\lambda_p,l}$ are $1/16$ for all sensor pairs, the total error in phase difference could be $1/8$ of a projected wavelength. An upper bound on the SPL error at the source location can then be calculated. The squared

amplitude of the SPL becomes

$$P_{k,err} \geq MA^2 + 2A^2 \sum_{i=2}^M \sum_{l=1}^{i-1} \cos(2\pi(\frac{1}{16} + \frac{1}{16})) \quad (3.2.1.5)$$

$$= MA^2 + 2A^2 \sum_{i=2}^M \sum_{l=1}^{i-1} \cos(\frac{\pi}{4}) \quad (3.2.1.6)$$

$$= MA^2 + 2A^2 \left(\frac{M^2 - M}{2} \right) \frac{\sqrt{2}}{2} \quad (3.2.1.7)$$

$$= A^2 \left(M + M(M-1) \frac{\sqrt{2}}{2} \right) \quad (3.2.1.8)$$

$$> \frac{\sqrt{2}}{2} A^2 M^2 \quad (3.2.1.9)$$

$$\approx A^2 M^2 - 1.5 \text{ dB}. \quad (3.2.1.10)$$

Equation 3.2.1.10 reveals that if sensors are positioned to within 1/16 of the source's projected wavelength, then the most that the SPL calculation can be off by is 1.5 dB! When the source is located at the turbine hub, $\lambda_p = \sqrt{2}\lambda$. The allowable error can then be written as $\varepsilon_{\lambda_p} \leq .0884\lambda$. In order for SPL estimate errors to be considered negligible, the microphones must be positioned to within 8.84% of the wavelength observed. A general rule of thumb is to position microphones to within 10% of a wavelength. Using this rule of thumb, the upper bound on SPL error using the previous derivation is 2 dB. At 250 Hz, 1 kHz, and 4 kHz, the allowable errors using this rule of thumb are 13.7 cm, 3.43 cm, and 8.58 mm respectively. An upper bound on power error as a function of sensor position uncertainty, based on equation 3.2.1.3, for a source at the hub causing $\lambda_p = \sqrt{2}\lambda$ is

$$err(P_k) \leq \cos(2\pi\sqrt{2}(\% \lambda)), \quad (3.2.1.11)$$

where $\% \lambda$ is the wavelength percentage error bound.

Another consideration is that even though the true location of the source might reveal an SPL 1.5 dB less than the actual value, other locations might produce SPL estimates that are greater than that value. If this is the case, the position of the mainlobe peak would be at a different location than the actual source. A statistical analysis of the location offsets and detected power errors is presented in the next section.

3.2.1.1 Sensor Position Uncertainty Statistics

Due to the difficulty in deriving an analytic solution to the statistics of detected power levels and beam position errors from sensor position uncertainties, Monte Carlo simulations are used here to show the trends. The simulations consider a 1 kHz point source located at the wind turbine hub ($x = 0$ m, $z = 22.8156$ m) for the Bushland, TX configuration using the mid sub-array, optimized for 1 kHz (see section 5.2). Statistics are derived for the loss in detected power due to sensor position errors as well as the error in the main beam location in terms of absolute offset for 100 random sets of position errors for each degree of uncertainty.

Three types of sensor location perturbations are considered. A sensor position error equal to the level of uncertainty is introduced. This is the error type that is used in the derivation of the upper bound on beamformer error. Each sensor is randomly positioned along the circle of radius equal to the error parameter from its desired location. The second type of error is a uniform sensor position error where the radial error in position is chosen uniformly between 0 and the error parameter. The third type of error is a Gaussian random error where the radial error in position is chosen as the absolute value of a zero-mean Gaussian random variable with variance equal to the error parameter. The angles of all position errors are chosen uniformly in the xy plane. The error parameter used is the distance in terms of percentage of a wavelength at 1 kHz. It is unknown which method of error modeling is more representative of actual placement errors in the field. The fixed distance and uniform random variable methods eliminate the possibility of distant outliers, which is realistic, but the Gaussian method adds shape to the error distribution, realistically adding more weight to smaller location errors.

Simulation results for power error for the three cases are shown in figures 3.11, 3.12, and 3.13 along with the upper bound derived in the previous section. The upper bound, from equation 3.2.1.11, is only shown until 15.5% λ because the bound approaches infinity at a 17.7% wavelength error and an analytical upper bound does not exist for larger errors. Results are provided for wavelength errors between 1% and 40%. These plots show the median value, lower

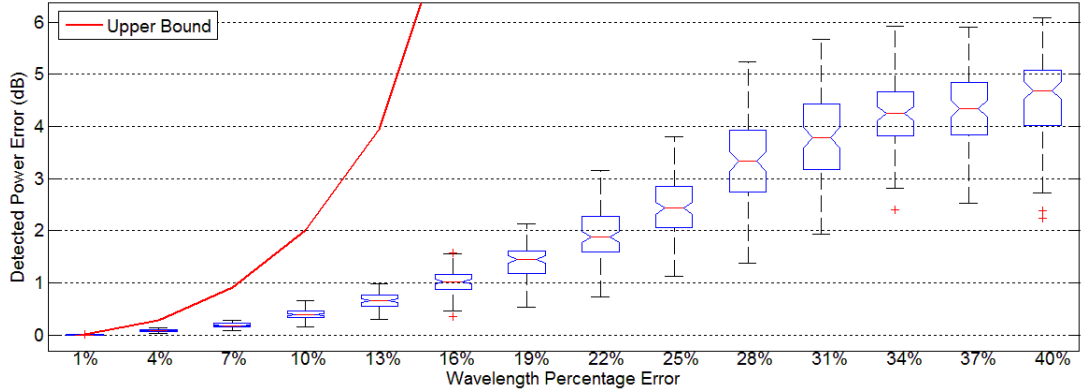


Figure 3.11: Beamformer Power Error Statistics as a Function of Sensor Position Errors (Fixed Distance Error)

and upper quartiles, 1.5 interquartile range values, and outliers. Clearly, the upper bound is not a good indicator of the typical error values experienced, since no outliers reach anywhere near the bound.

Analyses of the beam location error statistics for the three cases are presented in figures 3.14, 3.15, and 3.16. For position errors up to 25% of a wavelength for the fixed error model and 22% of a wavelength for the Gaussian model the beam position errors are negligible, rarely exceeding 0.5 meters. The plots are slightly confusing above these values because the position errors jump to very large values and spreads. Here, the mainlobe height has decreased so much and sidelobes have increased by enough for the sidelobes to become stronger than the mainlobe. At this point, the mainlobe location could appear at any point on the beamformer scan plane and the beamformer becomes useless. For the uniformly distributed case, the mainlobe remains very close to the source location except for the outliers at wavelength errors of 37% and 40%.

A summary of the beamformer errors for the wavelength percentage errors analyzed is provided in table 3.1 by analyzing the 95th percentile of the errors for all cases. These values provide a more reasonable indicator of expected beamformer error than the analytically derived bound. The 95th percentile power errors at 10% λ are 0.5424 dB for the fixed error model, 0.2383 dB for the uniform model, and 0.6647 dB for the Gaussian model, which are far better than the 2 dB analytic bound. In fact, the 2 dB upper bound is not likely to be reached until

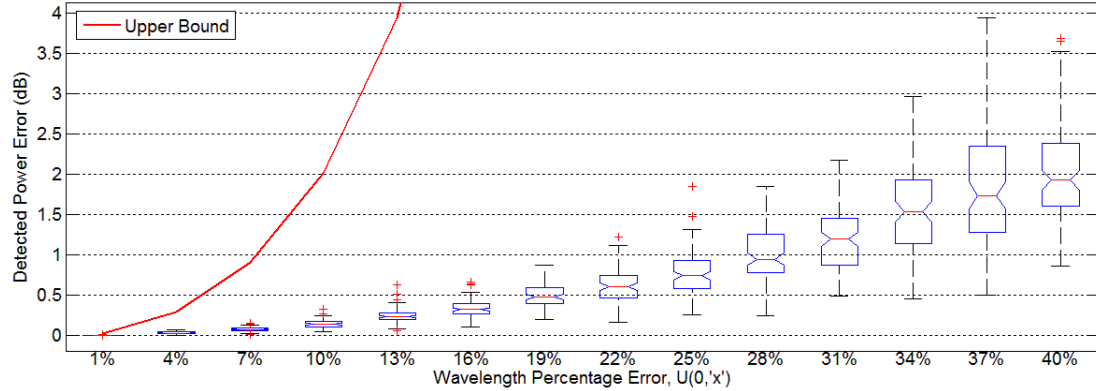


Figure 3.12: Beamformer Power Error Statistics as a Function of Sensor Position Errors (Uniformly Distributed Error)

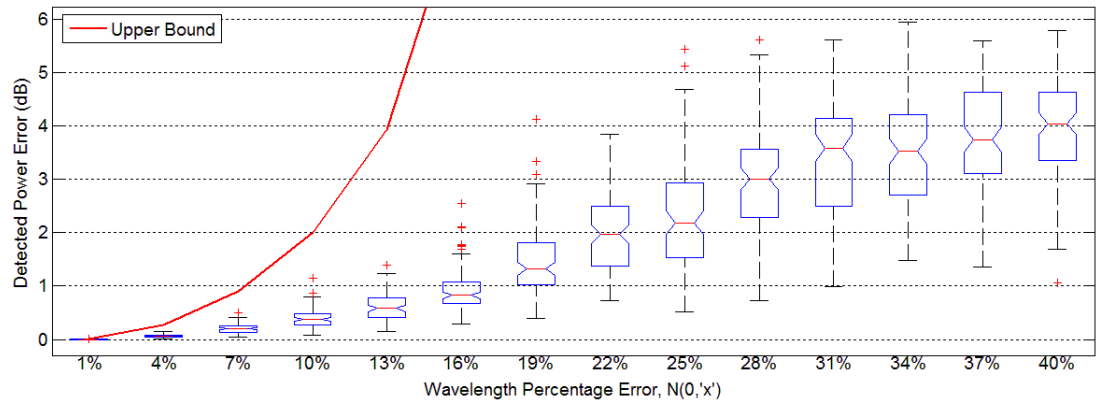


Figure 3.13: Beamformer Power Error Statistics as a Function of Sensor Position Errors (Gaussian Error)

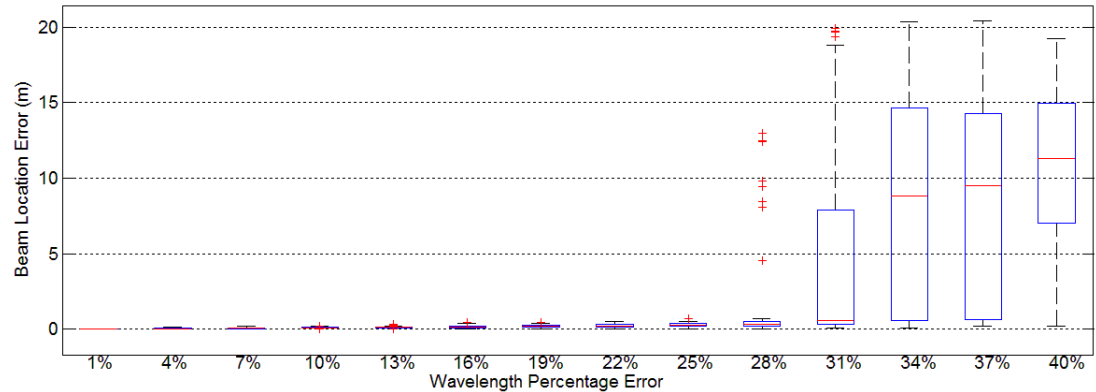


Figure 3.14: Beam Position Error Statistics as a Function of Sensor Position Errors (Fixed Distance Error)

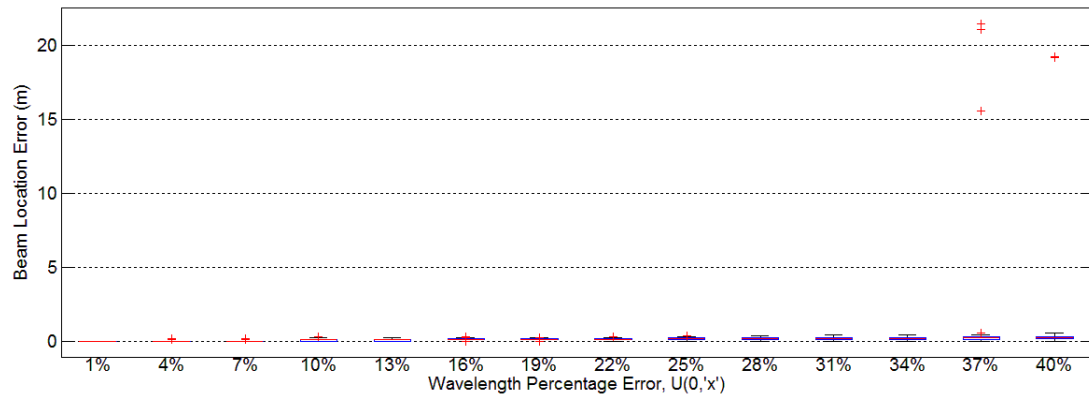


Figure 3.15: Beam Position Error Statistics as a Function of Sensor Position Errors (Uniformly Distributed Error)

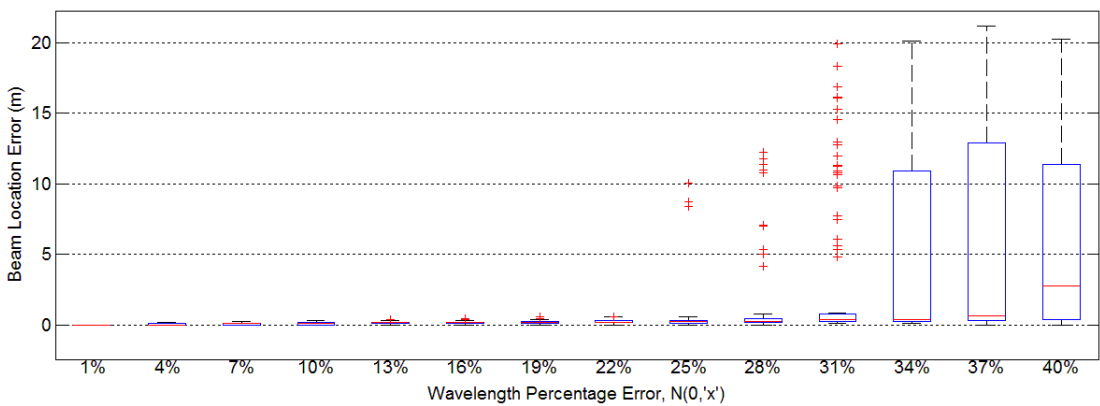


Figure 3.16: Beam Position Error Statistics as a Function of Sensor Position Errors (Gaussian Error)

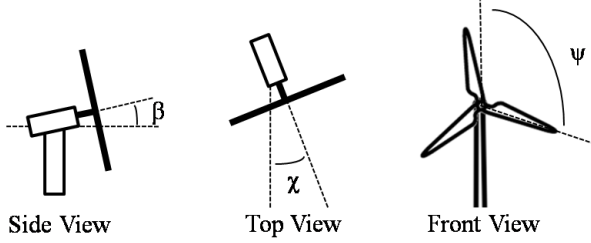


Figure 3.17: The Angles Describing Rotor Position

the position errors exceed $19\% \lambda$. These Monte Carlo simulations show that for up to 22% wavelength sensor position errors, the beamformer mainlobe is likely to be within 40 cm of the true location with up to 3 dB of power error. Above $22\% \lambda$ error, the beamformer map is likely to fall apart, with spurious sidelobes becoming stronger than the mainlobe, with up to 5.5 dB of power error.

3.2.2 Uncertainties in y -direction Distance from Array to Source

A common scenario encountered in wind turbine beamforming applications is when an acoustic source is not located directly on the plane that is being scanned. Turbine rotors usually have a tilt angle, β , which causes the blades to no longer travel purely in the xz -plane. Therefore, a beamformer scanning the xz -plane can have some y -distance errors introduced. Another scenario is when the rotor yaw angle, χ , offset from the direction the array is located, is large enough and not corrected for completely. In this case, the scan plane might have an angular offset from the rotor plane and sources may be located behind or in front of the scan plane. Figure 3.17 shows angles χ and β as well as the rotor azimuth angle, ψ , which will be used later. Another classic case of source distance error is gearbox and generator noise, which is produced in the nacelle, located several meters behind the rotor. Finally, the true y -distance from the array to the rotor may not be known perfectly.

When the array is not properly focused onto the plane where an acoustic source is located, the source tends to appear in the location where the line formed between array center and source intersects the scan plane. This way, the array pattern caused by that point source is just shifted

Sensor Position Error (%λ) / Distance at 1 kHz	95th Percentile, Power Error, Fixed (%λ)	95th Percentile, Power Error, U(0,%λ)	95th Percentile, Power Error, N(0,%λ)	95th Percentile, Beam Location Error, Fixed (%λ)	95th Percentile, Beam Location Error, U(0,%λ)	95th Percentile, Beam Location Error, N(0,%λ)
1% / 3.4 mm	0.006 dB	0.003 dB	0.008 dB	0 m	0 m	0 m
4% / 1.4 cm	0.12 dB	0.055 dB	0.11 dB	0.14 m	0.10 m	0.10 m
7% / 2.4 cm	0.27 dB	0.13 dB	0.39 dB	0.14 m	0.10 m	0.14 m
10% / 3.4 cm	0.54 dB	0.24 dB	0.66 dB	0.22 m	0.14 m	0.22 m
13% / 4.5 cm	0.93 dB	0.36 dB	1.13 dB	0.22 m	0.14 m	0.22 m
16% / 5.5 cm	1.40 dB	0.50 dB	1.75 dB	0.30 m	0.22 m	0.32 m
19% / 6.5 cm	1.94 dB	0.72 dB	2.74 dB	0.40 m	0.22 m	0.36 m
22% / 7.6 cm	2.62 dB	0.98 dB	3.38 dB	0.42 m	0.22 m	0.42 m
25% / 8.6 cm	3.39 dB	1.19 dB	4.12 dB	0.45 m	0.23 m	0.57 m
28% / 9.6 cm	4.64 dB	1.63 dB	4.94 dB	8.44 m	0.32 m	7.06 m
31% / 10.6 cm	5.34 dB	1.89 dB	5.02 dB	17.56 m	0.32 m	15.31 m
34% / 11.7 cm	5.44 dB	2.47 dB	5.05 dB	17.34 m	0.41 m	15.19 m
37% / 12.7 cm	5.39 dB	3.32 dB	5.29 dB	16.64 m	0.42 m	17.47 m
40% / 13.7 cm	5.65 dB	3.41 dB	5.21 dB	17.29 m	0.51 m	17.45 m

Table 3.1: 95th Percentile of Beamformer Errors

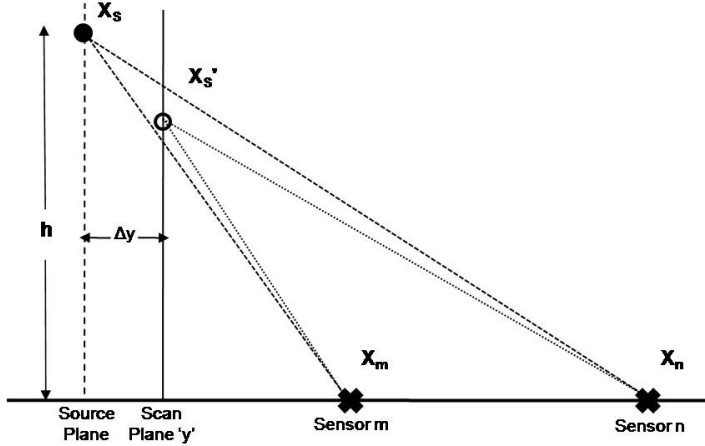


Figure 3.18: Y-Error Impact on Beamforming

either up or down on the noise map. Figure 3.18 illustrates this phenomenon. The z location of the source with a scan plane error of Δy , using similar triangles, can be approximated as $h' = \frac{y}{y+\Delta y}h$. A qualitative look at the trend caused by y distance errors is shown in figure 3.19. From the plots it can be seen that the z dimension offsets of the source location are shifted as expected for y errors in the scan plane. The array patterns become very distorted, however, and the source power errors are not trivial. For higher frequencies, using the smaller sub-arrays, the errors are less drastic however.

Using an unfocused beamformer, errors in the received magnitude of the signal are due to discrepancies in the phase difference between sensor pairs. The phase difference between sensors m and n is $\frac{|X_s - X_n| - |X_s - X_m|}{\lambda}$. As long as the value $\frac{|X'_s - X_n| - |X'_s - X_m|}{\lambda}$ is not significantly different from the actual phase delay, then the unfocused beamformer will give an accurate re-creation of the source, aside from the shifted source location. In general, the errors caused by an unfocused array will scale with the solid angle formed by the source and the array shape. When the angle $\angle X_m X_S X_n$ is small, the angle $\angle X_m X'_S X_n$ will be very close to it and the difference between the actual phase delay and the assumed, unfocused phase delay will be very small. This error increases as the angle $\angle X_m X_S X_n$ widens. As an illustration of this trend and to show how insignificant minor scan plane errors are when the array is small, figure 3.20 is shown. This plot

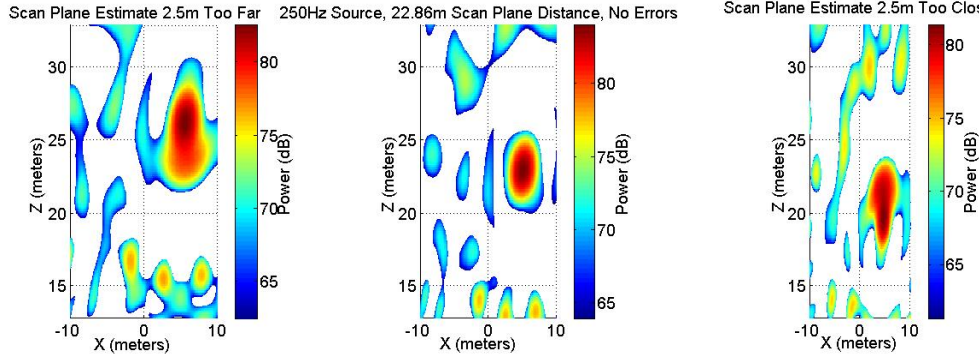


Figure 3.19: Z-Offsets of Received Source Due to Scan Plane Y-Distance Errors

demonstrates how the errors will increase with frequency observed and how a larger array shape will err more than small array shapes. All sources used in the simulations are located at hub height. The array and turbine model used are from the Bushland, TX field experiment, which will be described later.

Figure 3.20 reveals that the mid-size array will still operate very well when unfocused up to ± 5 meters. Problems may arise, however, when the large, low frequency array is used. As an example, if gearbox noise is generated 4 meters behind the rotor, a beamformer focused on the rotor plane will estimate that noise at 500 Hz to be more than 2 dB less than its true strength. Although the beamforming power error is a good metric for gauging the y offset errors, another interesting indicator is the sidelobe rejection. Figure 3.21 shows the sidelobe rejection compared to the mainlobe for the scan plane distance errors present in figure 3.20. Only sidelobes within one rotor radius of the mainlobe are considered here. The array pattern clearly becomes very distorted for extreme y errors. At errors of 4 and 5 meters, the low frequency, 250 Hz and 500 Hz and mid frequency, 2 kHz array patterns contain sidelobes that are roughly as strong as the mainlobe.

3.2.3 Uncertainty in Source Wavelength

The last input parameter uncertainty to be analyzed is the source wavelength, which is used to determine the phase delays in the beamformer. There are two ways that errors in the

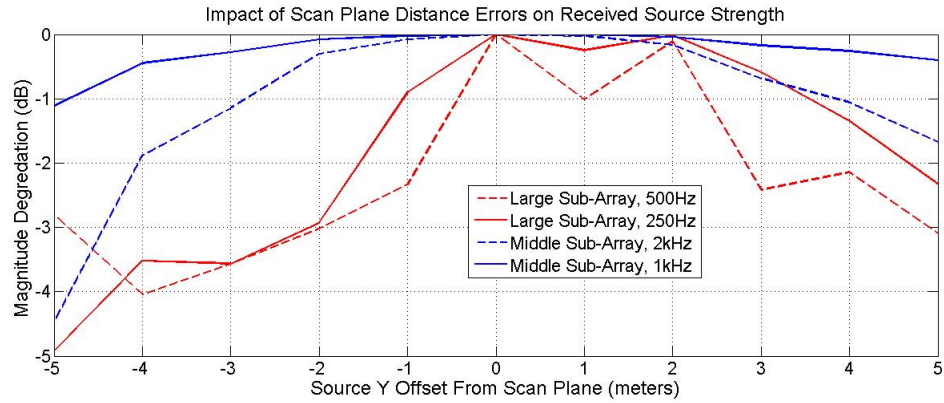


Figure 3.20: Magnitude of Unfocused Beamforming Errors

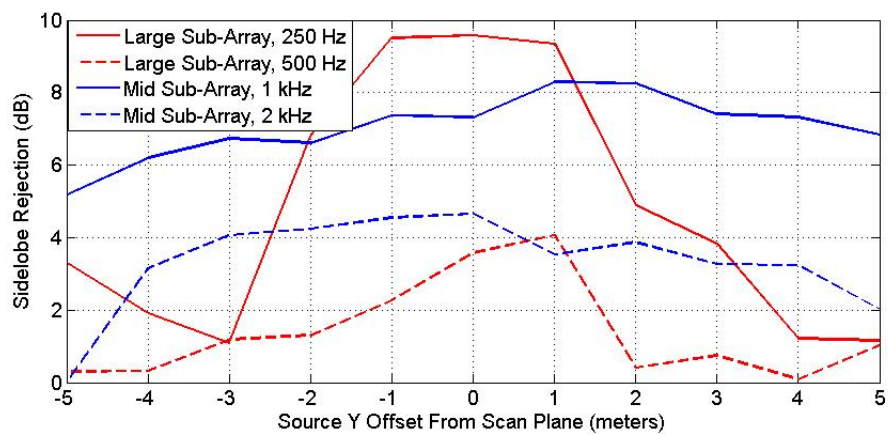


Figure 3.21: Sidelobe Rejection Due to Unfocused Beamforming

wavelength can be introduced. Since wavelength is equivalent to $\lambda = \frac{c}{f}$, one way of introducing error is through imperfect knowledge of the speed of sound, c . The most common way of incorrectly calculating c is by imperfect knowledge of the air temperature. The dependence of c on temperature is shown in equation 3.2.3.1 where R is the universal gas constant, γ is the adiabatic constant, M is the molecular weight of the gas, and T is the temperature in K [57].

$$c = \sqrt{\frac{\gamma RT}{M}} \quad (3.2.3.1)$$

For dry air, this reduces to

$$c = 20.05\sqrt{T} \quad (3.2.3.2)$$

$$c = 20.05\sqrt{273.15 + T_C} \quad (3.2.3.3)$$

where T_C is the temperature in degrees Celsius. When the air temperature is 19.5° C, c is 343 m/s. If the temperature is actually 10 degrees higher than this, c is 348.8° C; if it is 10 degrees lower, c becomes 337.1° C.

The other way of causing wavelength error is by incorrectly guessing the frequency of the source analyzed. This may seem like a moot source of error because the beamformer only analyzes the frequency of interest and knows what that frequency is. In practice, the beamformer analyzes short time periods of data on which the FFT is performed. The FFT bins contain a frequency band as wide as the inverse of the length of time of the block of data on which the FFT is performed. For an FFT block length of K samples and a sampling rate of S samples/second, the bin width is $\Delta f = \frac{S}{K}$ Hz. The data in this research is sampled at $S = 25 kS/s$ and most of the analyses use a block length of $K = 1024$ samples, or 41 milliseconds. In this case, $\Delta f = 24.41$ Hz. Since the beamformer uses the center frequency of each bin as the assumed frequency, the largest frequency error possible is $\frac{\Delta f}{2}$ or 12.21 Hz.

The effects of an error in the speed of sound can be understood by observing the beamforming geometry in figure 3.22. This figure is similar to figure 3.18 in that it illustrates a source in the $x = 0$, yz plane. The distances $R1$, $R2$, and $R3$ are the distances waves propagating from the corresponding sources travel between sensors m and n . These distances can be interpreted

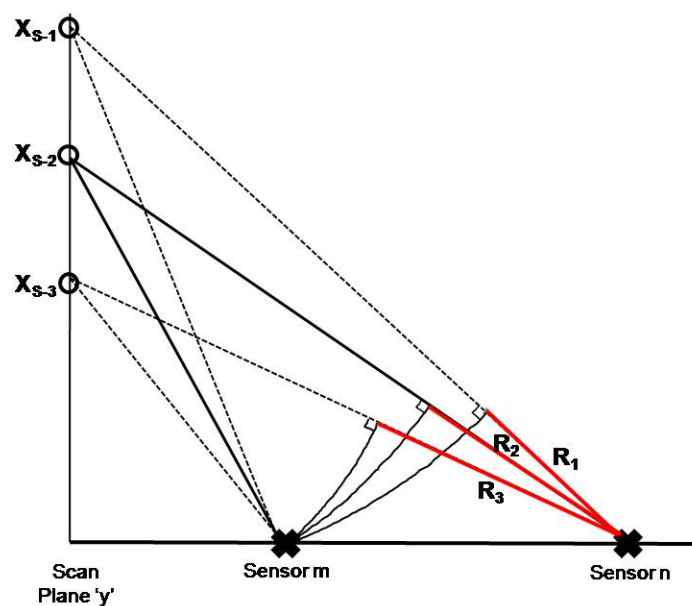


Figure 3.22: Beamforming Geometry in the yz -Plane

as the number of wavelengths separating the sensors when written as $R = (\#\lambda) \cdot \lambda$. Assume that a source is present at X_{S-2} and propagates at a speed c . The number of wavelengths separating sensors m and n is R_2/λ , meaning that there is a phase shift of $2\pi R_2/\lambda$ between the sensors. If the beamforming calculations use a wavelength of λ' instead of λ due to errors in frequency and/or the speed of sound, the beamformer will calculate the phase delay between sensors m and n for the source to be $2\pi R_2/\lambda'$. If λ' is less than λ , when beamforming to position X_{S-2} the predicted phase shift between sensors m and n will be greater than the actual value. However, with a value of λ' that is too low, a location in the same scan plane but above X_{S-2} would result in a phase shift that would match the measured phase shift because the higher a supposed source is on the scan plane, the less phase shift it will produce between sensors m and n . The opposite is true for $\lambda' > \lambda$. In this case, the measured phase shift will correspond to a source position that is below the actual source. The beamforming operation will result in an underestimated phase shift and the measured value will correspond to a lower source position that would produce a greater phase shift. The effects of this are that since $\lambda = \frac{c}{f}$, an error causing an increase in c or a decrease in f will cause the source to appear lower than it actually is and a decrease in c or an increase in f will cause the source to appear higher than it actually is. These trends can be observed in the plots of figure 3.23, which show the beamforming results for a 250 Hz source with no errors, with a λ estimate that is too high (temperature is estimated too high or frequency is estimated too low), and with a λ estimate that is too low (temperature is estimated too low or frequency is estimated too high). The errors correspond to frequencies that are estimated with an error of $\frac{\Delta f}{2}$, or 12.21Hz.

Figure 3.24 shows the negative effects of wavelength errors in the form of degradation to the received power at the received shifted source location. Three different parameters are investigated: the location of the source (at the hub, to the right of the hub, and below the hub), the frequency of the source (at the sub-array's intended frequency and at twice that frequency), and the sub-array. The trends in this plot show that power errors are negligible for temperature errors that are less than 10 degrees and that the largest errors are caused when the frequency

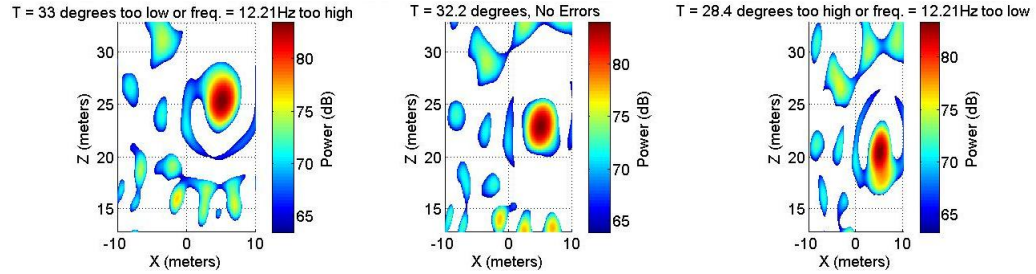


Figure 3.23: The Effects of Beamforming with Errors in the λ Estimate

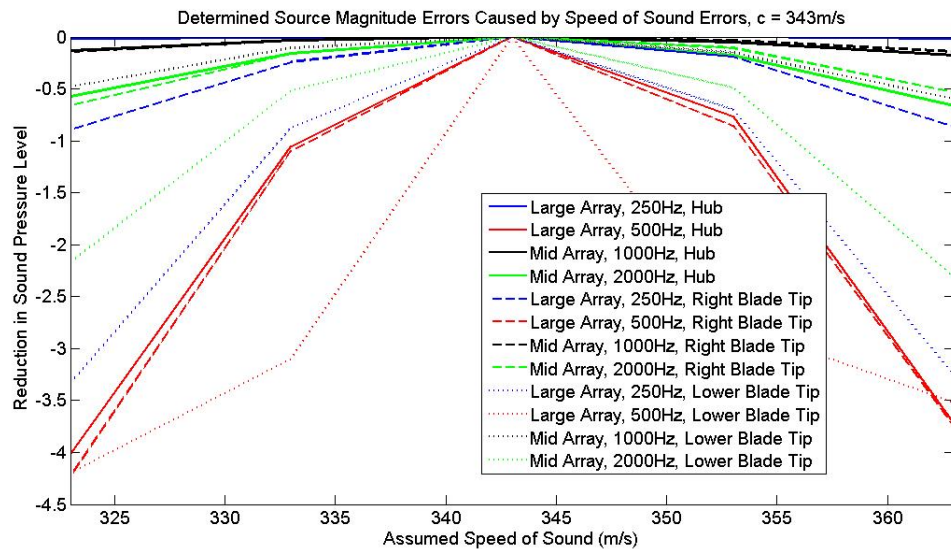


Figure 3.24: Received Source Power Degradation Due to Errors in the λ Estimate

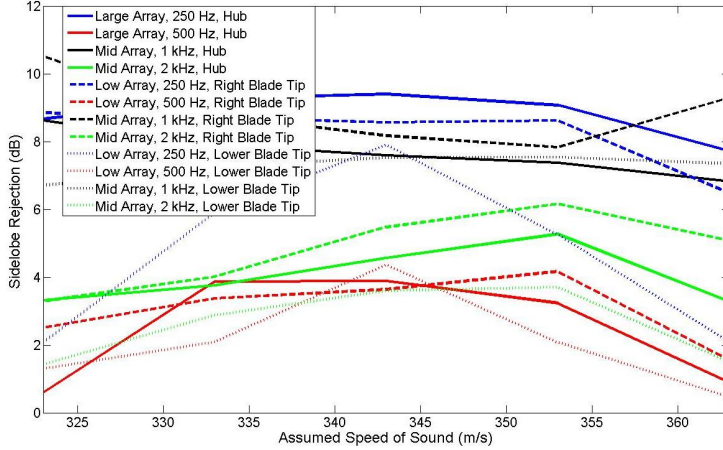


Figure 3.25: Sidelobe Rejection Due to Errors in the λ Estimate

analyzed is greater than the intended frequency of operation for a sub-array. Also, errors for the smaller or higher frequency sub-arrays are negligible. Caution must therefore be taken when beamforming at the lower frequencies because the 12.21 Hz errors cause the wavelength errors to be off by a relatively large fraction of the original frequency. The effects of the wavelength errors on the sidelobe rejection of the array patterns for the beamforming cases of figure 3.24 are presented in figure 3.25. The distortion of the array pattern is most prominent when a sub-array is used to observe the higher frequencies it is designed for. When the source is positioned low on the scan plane, the wavelength errors have a more dramatic impact on the sidelobe levels of the array patterns as well.

3.2.4 Wind Shear Effects

Even if the speed of sound is known perfectly when beamforming, the presence of wind will affect the speed at which an acoustic signal will travel to the microphones. In the scenario where wind speed remains constant with height, the speed at which a signal propagates from a source to a microphone will vary depending on the source and sensor positions. This modification of the speed at which an acoustic signal travels is caused by the wind either acting against the signal's direction of travel and decreasing the speed of propagation or acting with the direction of

travel and increasing the speed. The resulting sensor specific effective sound propagation speeds likely degrade the array's performance beyond the effects of a constant speed of sound error across all sensors described in the previous section. Further simulations need to be performed to determine the exact effects.

A formula for determining the effective speed of sound for a source propagating against the wind is provided in equation 3.2.4.1 where c_e is the effective speed of sound, c is the actual speed of sound, U is the wind speed, x_s, y_s, z_s are the coordinates of the source, and $x_m, y_m, 0$ are the coordinates of the sensor. This formula uses the same coordinate system that is shown in figure 2.1 and assumes that the wind is in the positive y direction with zero x and z component.

$$c_e = \frac{c \left(1 - \left(\frac{U}{c}\right)^2\right) (z_s^2 + (x_s - x_m)^2 + (y_s - y_m)^2)}{\frac{U(y_s - y_m)}{c} + \sqrt{\left(\frac{U(y_s - y_m)}{c}\right)^2 + \left(1 - \left(\frac{U}{c}\right)^2\right) (z_s^2 + (x_s - x_m)^2 + (y_s - y_m)^2)}} \quad (3.2.4.1)$$

Adjusting the beamformer to account for the scenario where wind speed is constant with height is not an easy task but unfortunately wind speed is not even constant with height. In practice, a vertical wind shear is present in the boundary layer of the atmosphere where wind turbines are located. The wind shear is modeled as the scaled logarithm of height relative to some reference height. The wind shear for a reference height characteristic of agricultural land is shown in figure 3.26 for an 11 m/s hub height (22.8156 meters) wind speed [41]. Wind shear causes a gradient in the effective speed of sound for a signal propagating toward a sensor and therefore acts as a lens that bends a propagating ray of sound. When a source is propagating in the general upwind direction, the lens effect causes a ray of sound to bend downward [42]. It is currently unknown how wind shear effects can be corrected for in the beamforming operation and the study of its effects will be a focus of this research in the future.

3.3 The Effects of Doppler Shifts Due to a Rotating Source

Complications arise when the acoustic source analyzed through beamforming is not stationary. A source in motion, like a wind turbine blade, will cause a Doppler shift to be present in the received signals at each microphone. If all microphones were to experience the same Doppler

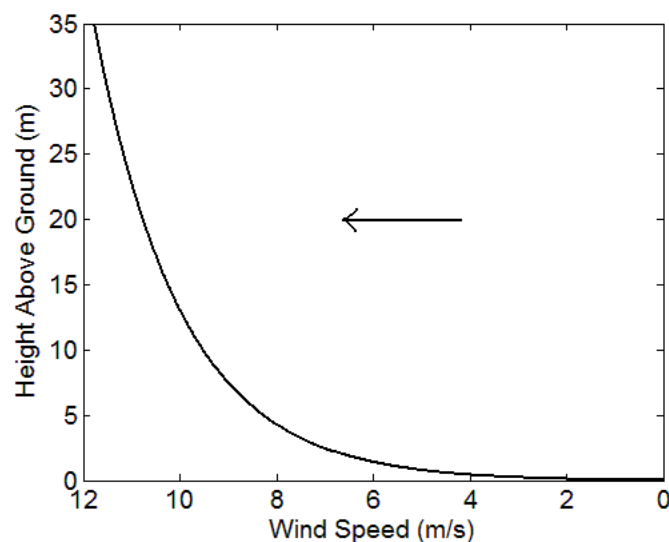


Figure 3.26: Wind Shear for an 11 m/s Hub Height Wind Speed

shift, the beamforming algorithm would be unaffected and the only correction that would remain would be to assign the output of the beamformer at each frequency to the correct non-Doppler shifted frequency. Since no two sensors receive signals with the same Doppler shift, the phase delays of the signals received at each location will differ from the case when each signal has the same Doppler shift. These phase delay errors will harm the beamformer performance and must be taken into account [36, 38, 39]. If the paths from the source to all of the microphones form a relatively small solid angle, the phase delay errors will not be as drastic as when the sensors are very spread out relative to the source. In order to capture the necessary resolution for the Bushland, TX tests, the array takes up a very large solid angle of a source's radiation pattern. Each microphone experiences a Doppler shift of

$$f_{obs} = \frac{c}{c + v_r} f_0, \quad (3.3.0.1)$$

where f_{obs} is the observed frequency, f_0 is the emitted frequency, and v_r is the radial velocity of the source towards the receiver (positive when moving away from the receiver, negative when moving towards).

A formula for the radial velocity is

$$v_r = \frac{(\vec{x}^0 - \vec{x}_m) \cdot \vec{v}^0}{|\vec{x}^0 - \vec{x}_m|}, \quad (3.3.0.2)$$

where, as introduced previously, \vec{x}^0 is the assumed vector position of the source, \vec{x}_m is the vector position of sensor m , and \vec{v}^0 is the velocity of the source. The radial velocity of the source is the projection of the source velocity onto the line between the source and sensor. A major detriment to the speed of a beamforming algorithm that accounts for these radial velocities is that \vec{v}^0 must be calculated at each scan grid location. A source on the rotor plane will have a different velocity at each position. To calculate this velocity, the azimuth angle of the blade under investigation, the tilt angle of the rotor, the yaw angle of the turbine, and the rotational speed of the turbine must be known. The rotor tilt angle, β , is the angle that the rotor axis is tilted, offset from being parallel with the xy plane. For the research conducted in Bushland, TX the offset is 4° . The yaw angle of the turbine, χ , is the angular offset of the rotor axis from

the yz plane defined by the array coordinate system. The rotor azimuth, ψ , is the angle of the blade under investigation relative to directly upward. A visualization of these angles is shown in figure 3.17.

It is useful to treat a point on the rotor scan plane as a polar coordinate, where r^0 is the distance from the rotor axis to the scan point and the rotor azimuth angle is the offset from the upward position. Accounting for these three angles and transforming points on the rotor scan plane into polar coordinates, the x , y , and z components of the source velocity can be written as

$$v_x^0 = \frac{2\pi r^0}{T_r} (\cos(\chi) \cos(\psi) + \sin(\chi) \sin(\beta) \sin(\psi)), \quad (3.3.0.3)$$

$$v_y^0 = \frac{2\pi r^0}{T_r} (\sin(\chi) \cos(\psi) - \cos(\chi) \sin(\beta) \sin(\psi)), \quad (3.3.0.4)$$

and

$$v_z^0 = -\frac{2\pi r^0}{T_r} \cos(\beta) \sin(\psi), \quad (3.3.0.5)$$

where T_r is the rotational period of the turbine rotor.

Two ways of correcting for the Doppler induced errors are proposed. The first approach is to mix the time signals up or down to counter the Doppler shifts and then to shift the phases of the signals to simulate inter-sensor signal propagation at the original frequency. A second technique is to time shift the signals to steer the array towards a central location in the scan plane and then use frequency based beamforming to fine tune the beamformer towards the specific grid locations. The former technique will perfectly counter all Doppler errors assuming perfect knowledge of the rotor position and velocity but is extremely computationally inefficient. The latter technique still requires the time signals to be mixed to correct for Doppler shifts, but relies on the additional phase shifts required after time shifting the signals to be relatively minor and therefore subject to insignificant phase errors.

3.3.1 A Complete Doppler Error Correction Technique

Two stages are involved in the Doppler correction for the microphone signals. The first step is to mix each microphone signal up or down to correct for the Doppler shift imposed on it. To find the amount by which to shift each signal, f_{obs} is solved for using equation 3.3.0.1 where f_0 is the original emitted frequency of interest, usually the center frequency of a particular FFT bin. The signal at microphone m is then mixed in the time domain by the amount $f_0 - f_{obs}$, becoming

$$e^{j2\pi(f_0-f_{obs})} s(t). \quad (3.3.1.1)$$

The frequency domain equivalent is

$$S_{m,mixed}(f) = S_m(f - (f_0 - f_{obs})). \quad (3.3.1.2)$$

Correcting for the frequency shift imposed by the Doppler shift is not enough to make the signals suitable for beamforming. The phase of the signals at each microphone must be adjusted to behave as if the original signals received were all at the original frequency. A reference point, which will usually be the origin of the array, must be defined. The phase related problem that arises due to the Doppler effect is that even after mixing the signals to the original frequency the difference in phase between sensor m and the reference point will not reflect the number of wavelengths the source would have travelled between the reference point and the sensor had the signal propagated with the original frequency in all directions. Because a narrowband signal received at each sensor and the reference point have different wavelengths due to the Doppler effect, the phase difference will not reflect a physical number of wavelengths separating the sensor and reference point. The frequency mixing used to correct the frequencies of each signal does not alter the central phase of each signal so further correction is needed. The number of wavelengths the source travels between microphone m and the reference point, θ , at the Doppler shifted frequency is $(r_m - r_0) \frac{f_0}{c}$, while at the frequency of interest the number of wavelengths is $(r_m - r_0) \frac{f_{obs}}{c}$. The difference between these two values is the amount by which the phase of each microphone signal must be adjusted to simulate a Doppler-free medium. The frequency domain

representation of the resulting signal after both Doppler correction steps have been taken is

$$S_{m,final}(f) = e^{j\frac{2\pi}{c}(r_m - r_0)[f_{obs} - f_0]} S_m(f - (f_0 - f_{obs})). \quad (3.3.1.3)$$

The signals now simulate the signals that would be received if the source were propagating through a Doppler-free medium. Unfortunately, the processing performed in equation 3.3.1.3 alters the beamforming process and alters the array pattern. The beamformer can no longer be assumed to be a linear system. The range of Doppler shifts that occur from a source over the span of the array is enough to justify the modifications however.

The reason that the error correction method described here is so computationally inefficient is that the CSM can no longer be calculated once prior to the multi-grid point beamforming operations. Each of the N length K blocks of sampled time data that are averaged together to calculate the CSM must be mixed in the time domain, phase shifted in the frequency domain, and then averaged together to form the corrected CSM. The problem is that since there is a different set of Doppler shifts and phase errors for each location on the scan grid, the CSM must be recalculated for each grid point. It is not uncommon for the scan plane to consist of $G = 10,000$ grid points. Therefore, if the beamformer is analyzing N blocks of data at G scan plane locations at K_S FFT bins, the Doppler correction routine will need to be applied to a length K time series $N \cdot G \cdot K_S$ times. A typical value of this product would be 2,000,000. One way to reduce the number of times the Doppler correction routine must be executed is to correct the signals at fewer grid points than G . An example would be to correct the signals every 1 meter by 1 meter along the scan grid and then use that CSM estimates for 10 or so finer grid points within that $1m^2$ area.

To illustrate the significance of inter-sensor phase errors when the Doppler effect is not corrected for, figure 3.27 is provided. The plots show the effects of sensor position dependent Doppler shifts for a source at the blade tip over all azimuth angles for the Bushland, TX array experiment. The plot of Doppler shift differences shows the average as well as the maximum magnitude of the difference in received frequencies for all sensor pairs. The plot of phase errors

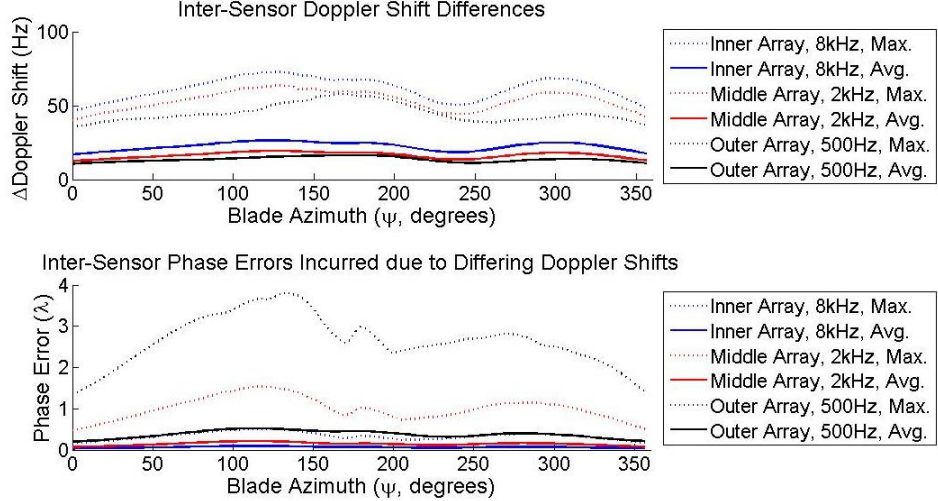


Figure 3.27: The Effects of Sensor-Dependent Doppler Shifts on Inter-Sensor Phase Differences

shows the difference in number of wavelengths a source travels between sensor pairs when sensor dependent Doppler Shifts are accounted for or ignored ($| \frac{(r_m - r_0)(f_{obs} - f_0)}{c} |$). Shown in the plots are the curves for the inner, or high frequency array, the middle, or mid frequency array, and the outer, or low frequency array at the highest frequencies they will observe (an octave above their intended frequencies). For the high frequency array, the maximum phase error is about 50% of a wavelength, while the average is never more than 10%. Using the 10% wavelength rule of thumb, these errors could be allowable (although they would compound with position errors). For the mid frequency array, the average phase errors are between 10% and 20% of a wavelength over all azimuth angles with a maximum error of 1.5 wavelengths. Caution should obviously be taken in this regime. The problem becomes drastic during low frequency beamforming where the average phase errors can be as high as half of a wavelength. Note that the maximum phase error is close to four wavelengths! Clearly, corrections must be made to avoid major beamforming errors. A property of the Doppler induced phase errors is that all of the curves in figure 3.27 will scale with the frequencies analyzed. At the intended observation frequencies for the sub-arrays, the levels of the curves are half of what they are as shown.

3.3.2 Doppler Error Mitigation by Time Delaying the Data

As mentioned earlier, a second way of countering phase errors due to Doppler effects is to time shift the data to steer the array towards a central location in the scan plane before using frequency domain techniques to fine tune the beamformer toward specific grid points. A major contributor to the large phase errors between sensors shown in figure 3.27 is that the phase must be adjusted between sensor pairs to steer the array in the general direction of the rotor plane then shifted by a smaller amount to steer towards specific grid points. Since the phase errors are proportional to the phase of the signal that separates any two sensors, this phase can be made drastically smaller by using a time shift instead of a frequency shift to correct for the majority of that phase. Time shifts do not accrue any of the phase mismatch errors that frequency based phase shifts do. When phase shifts are used to beamform, the data is all from the same moment in time and if the beamformer is adjusting the phase of each sensor's signal to look ahead or behind in time, the assumption that the nature of the signal does not change much over time is used and a time delay is translated to a phase shift.

If the signal of interest is Doppler shifted to a higher or lower frequency at one sensor relative to the other sensor in the pair, the phase shift technique does not work. The reason for this is that the wavelength, λ , of the signal, which is used when relating a time delay to a phase shift, is not the same at both sensor pairs. When shifting the data in the time domain, the wavelength or frequency of the signal is not used, so the time delay method will perfectly combine all of the signals. The caveat is that the signals must still be mixed to the intended frequency from their Doppler shifted frequencies.

The method can be thought of as time-domain beamforming to a central location and frequency-domain beamforming to finer specific grid points. The distance that the phase shift must account for is no longer the distance the signal travels from the source to a sensor subtracted from the distance it travels from the source to the array center, $r_m - r_0$. Instead, the phase shift corresponds to the difference between that distance and the distance a signal would travel

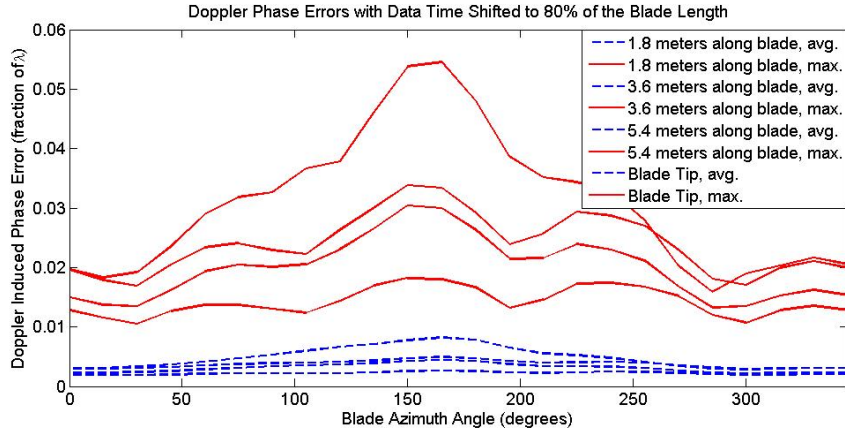


Figure 3.28: Doppler Induced Phase Errors When Data Is Time-Domain Steered to 80% Along the Blade

between the central scan plane location and a sensor subtracted from the distance a signal would travel between the scan plane center and the center of the array, $(r_m - r_0) - (r_{m,center} - r_{0,center})$. The phase shift this distance requires is much smaller than before the central time shift was used. The phase error due to Doppler effects reduces to $\frac{2\pi}{c}((r_m - r_0) - (r_{m,center} - r_{0,center})) [f_{obs} - f_0]$ from $\frac{2\pi}{c}(r_m - r_0) [f_{obs} - f_0]$. To illustrate how insignificant the phase errors can be, a scenario will be examined.

The scenario is based on the low frequency array used in Bushland, TX and considers a form of beamforming where a rectangular scan plane is created around a specific blade regardless of blade azimuth angle. The scan plane rotates with the blade when analyzing different blade azimuths. Figure 3.28 illustrates the phase errors caused by time-domain steering the array towards a point on the blade 80% along the blade span. The plot considers the errors that occur at four points along the blade, 1.8 meters, 3.6 meters, and 5.4 meters from the hub, and at the blade tip. The blade is 9 meters in length. The errors are plotted against the blade azimuth from 0 to 345°. The average phase error for all M(M-1) sensor pairs is shown along with the maximum inter-sensor phase error that occurred. Although the phase errors are not zero, they are negligible compared to the 10% wavelength criterion and can be ignored. Therefore, the phases do not need to be corrected before frequency-domain beamforming; only the Doppler

shifted frequencies need to be mixed up or down. This method reduces the amount of computing that needs to be performed at each grid point. The reason the signals still need to be mixed to the center frequency of the FFT bin under investigation is that some frequencies that lie in the k^{th} bin for one sensor's signal can be Doppler shifted out of that bin for another sensor's received signal and won't contribute properly to the total received power.

3.3.3 A Doppler Correction Example

To illustrate the effects that Doppler shifts can have on the final noise map of a rotating source, an example is provided. The scenario is a 244.14 Hz pure tone located at the tip of a blade on the Bushland, TX turbine. The rotor rotates at 55 RPM and the source travels at 51.67 m/s. The large sub-array is used and the beamforming is a hybrid of the methods described in sections 3.3.1 and 3.3.2. The array is first steered toward the hub of the machine by time shifting the signals. Then it is steered toward particular grid points around the blade at an azimuth angle of 90° using frequency-domain beamforming. For the frequency-domain beamforming, the complete Doppler correction technique is used from section 3.3.1, involving frequency shifts and phase shifts. This beamforming scenario is compared to the case where the signals are time shifted toward the turbine hub, but no further Doppler corrections are made. The beamformer simply accounts for the Doppler shift experienced at the center of the array, which is +29 Hz, by beamforming at 273.14 Hz. A comparison of the two methods is provided in figure 3.29. Surprisingly, the method that does not correct for individual frequency and phase discrepancies in the signals performs reasonably well. The complete Doppler correction technique detects the full power of the source, 84.09 dB, whereas the simpler method detects 83.12 dB, only a 0.97 dB difference.

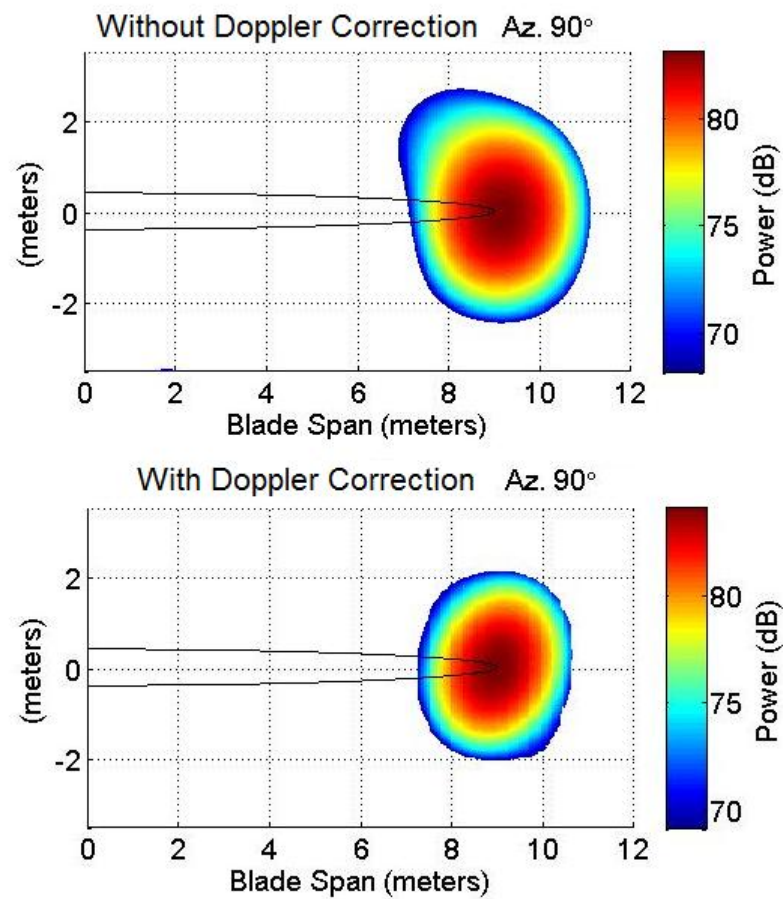


Figure 3.29: Doppler Correction Improvements

Chapter 4

Array Hardware

The array used in this research consists of 32 channels of data acquisition and 32 sensors.

Figure 4.1 illustrates the signal flow through the hardware that makes up the array. The finished product after operating the array in the field is a *Technical Data Management Streaming* (.tdms) file. The .tdms file format is a National Instruments technology designed to read and write measured data at high speeds [58]. National Instruments provides a DLL and header file as well as example MATLAB code for opening .tdms files in the MATLAB environment [59]. Therefore, the .tdms file is a logical data format to use for the storage and transfer of data from the data acquisition software, LabVIEW, to the selected data processing software, MATLAB. There are four logical divisions of the array hardware that are worth discussing. These subsystems are the microphone, the signal conditioner, the data acquisition system, and the hardware used to place microphones in the field.

4.1 Microphone Sensors

The criteria for the microphone sensor selection are that the physical size of the microphone must be small and the microphone must have a wide frequency response. The assumption that a sensor can be approximated as a point in space is the motivating factor in choosing a small microphone. To be specific, the microphone must sample the phase of the acoustic signal of interest at a single point in space. Obviously, a true volumeless point is an imaginary concept never encountered in the physical world, so a microphone will never perfectly act as a

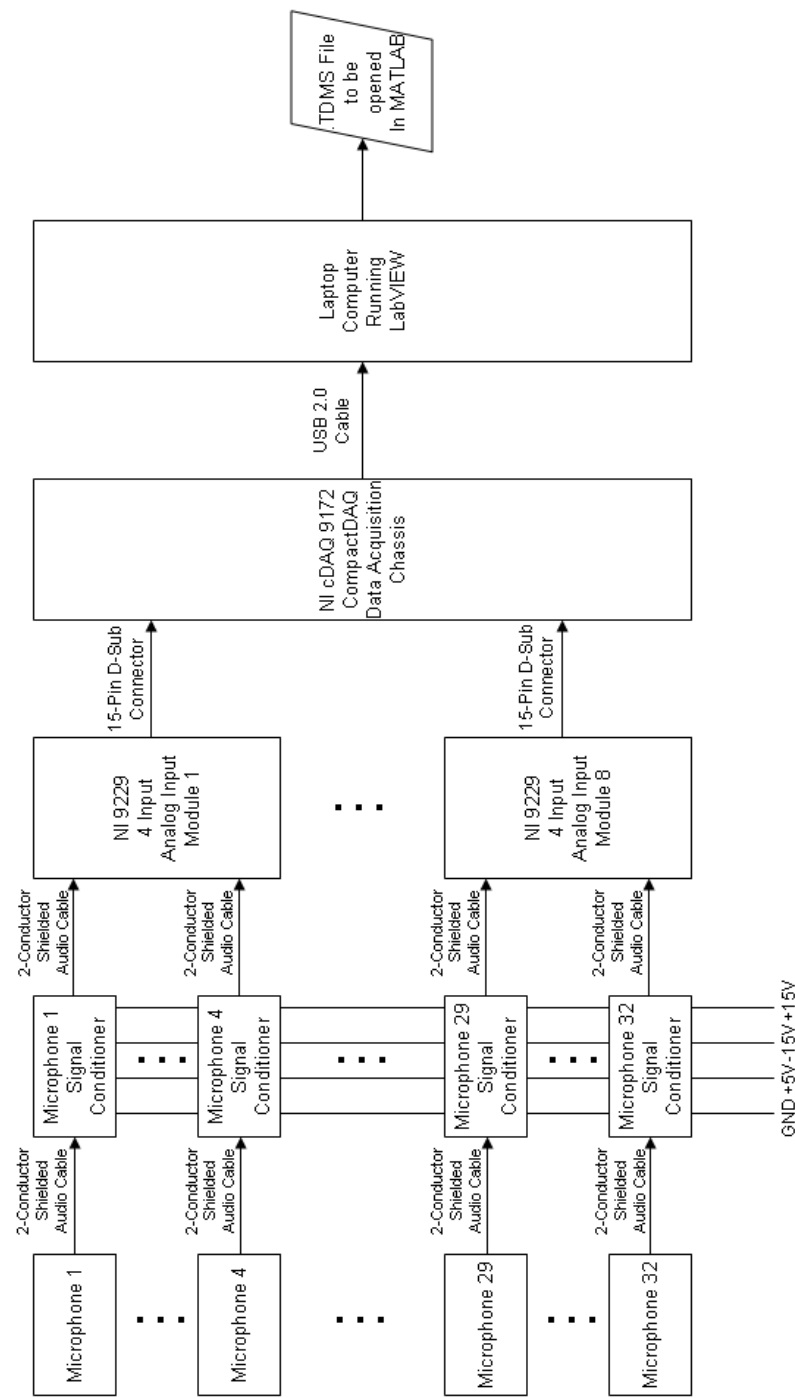


Figure 4.1: Array Hardware Flowchart

point sensor. However, as long as the diameter of the microphone is a small percentage of the smallest wavelength expected to be encountered, the sensor will sufficiently model a point. The highest frequency expected to be analyzed with the array is about 8 kHz. The wavelength for this frequency is 4.3 cm.

The second criterion for microphone selection is the wide frequency response. This must include the frequency band of interest for this research which is roughly 50 Hz-8 kHz. The microphone selected for the array was the Panasonic WM-61A, chosen by the first team assigned to this research in 2006-2007 [2], although more recently, the newer WM-64 model has been used. This microphone is a popular low-cost sensor for acoustic array processing and was used for wind turbine research by the NLR in The Netherlands [38].

The WM-61A is an electret condenser microphone with a diameter of 6 mm, a height of 3.4 mm, and a frequency range of 20 Hz-20 kHz [60]. The WM-64, which Panasonic replaced the WM-61 with, is identical to the WM-61 except that it has a height of only 2.2 mm. The wide frequency response and the small size make the WM-61/64 a good choice for the research. The 6 mm diameter is roughly 10% of the smallest wavelength of interest, making it a good approximation to a point sensor. The microphone has a typical frequency response curve that is flat with a +/- 1 dB ripple above 5 kHz [60]. To help block low frequency wind rumble, and to protect the microphones, wind screens are used on the microphones. A small, foam tie-clip microphone windscreens was chosen for use with the microphones (RadioShack model 33-4006). Later for the Bushland experiment, 90 mm Brüel and Kjaer windscreens (part number UA-0237) were added to further eliminate low frequency wind noise.

4.2 Microphone Signal Conditioners

Before the microphone signals can be sampled by the data acquisition system, power must be supplied to the microphone, the signal must be amplified, and the signal must be filtered to block DC signals. The electret condenser microphones require a bias voltage for operation. The voltage chosen for this is 5 V. An inverting amplifier is created using an operational amplifier

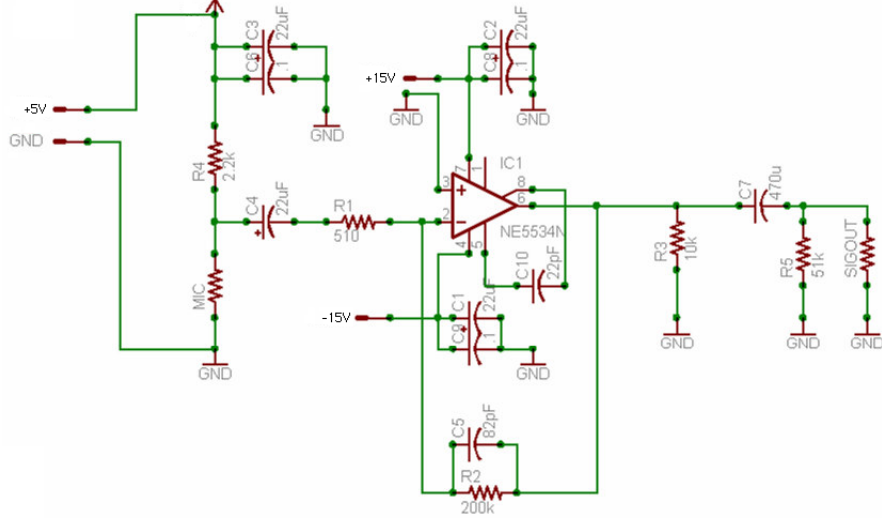


Figure 4.2: Signal Conditioning Circuit [2]

with a gain chosen to be $G = 392.17$ or $\frac{200k\Omega}{510\Omega}$. A capacitor is used to block DC signals from wind and from the bias voltage at the input to the amplifier circuit. At the output of the amplifier, a high-pass filter is attached with a corner frequency of $\frac{1}{2\pi 470\mu F \cdot 51k\Omega} = .007Hz$. The circuit for the signal conditioner is shown in figure 4.2. A modification made to this circuit is that capacitor C5 has been removed. This capacitor only adds a 1st order low-pass filter to the system which is not necessary because the data acquisition system includes an analog anti-aliasing filter. A switching power supply provides the 5 V, -15 V, and +15 V power supplied to each field deployable signal conditioner box. The operational amplifier used for the circuit is the Texas Instruments NE5534 device which is a low-noise audio amplifier.

4.3 Data Acquisition System

The data acquisition system chosen for the project was the National Instruments NI cDAQ 9172 chassis with eight NI 9229 analog input modules [3]. The NI 9229 modules are four-input modules allowing a total of 32 channels. The NI 9229 is a differential input module allowing low-crosstalk data acquisition [61]. With a dynamic range of +/- 60 V, the modules are able to sample the full range of the signals from the signal conditioners, which are limited

by the +/- 15 V power rails of the operational amplifier circuitry. To avoid aliasing, the data acquisition modules must sample at a rate at least twice the highest frequency of interest. Since this frequency is around 6-8 kHz, the system must sample at a rate of at least 16 kHz. The NI 9229 has the ability to sample with a data rate of $\frac{50kS/s}{n}$, where n can be chosen to be between 1 and 31. Possible data rates that meet the frequency requirements of the research are 50 kS/s, 25 kS/s, 16.67 kS/s, and 12.5 kS/s. A standard sampling rate of 25 kS/s is used throughout most of the research. The NI 9229 has an anti-aliasing filter at the front end with a cutoff frequency $f_C = 0.453 \cdot f_S$, where f_S is the sampling frequency. This anti-aliasing filter eliminates the need for a low pass filter in the external signal conditioning circuitry. The resolution of the NI 9229 module is 24 bits, which provides $7.15\mu V$ of analog resolution. Another important characteristic of the NI 9229 modules is that they simultaneously sample the channels every sampling period. When estimating the phase between signals detected at two channels it is necessary to know at which time the data from the channels were sampled. Simultaneous sampling makes this process easy because any two samples from the same sampling period are from exactly the same time. All of these characteristics make the NI 9172/NI 9229 data acquisition system excellent for use with the array.

4.4 Sensor and Signal Conditioner Characteristics

Characteristics of the sensor and signal conditioning stages must be known, such as the directivity, frequency response curve, and sensitivity (V/Pa). Also, the relative gain of each channel must be known to calculate the proper weight vectors for beamforming.

Experiments show that a signal propagating with an angle of incidence of 70° to the microphone sensor will produce the same power response as a signal propagating normal to the microphone. At incidence angles above 70° , the amplitude response of the microphone begins to decay, reaching an attenuation of -6 dB at 90° . The arrays used in this research do not include any sensors that form angles of incidence of more than 70° with the rotor plane. The omnidirectional nature of the WM-61A makes it easy to use with the array as no corrections

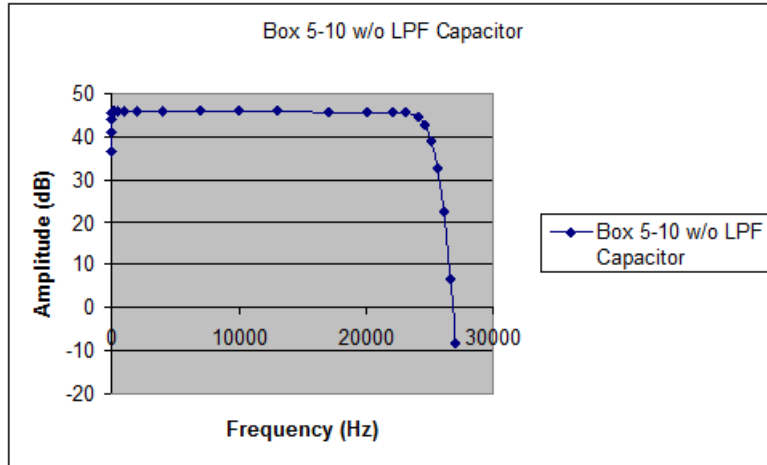


Figure 4.3: Frequency Response of the System without the Microphone

must be made for sensors forming different angles with the rotor plane.

The frequency response of the entire system without the microphones attached was determined by connecting a signal generator to the input of a signal conditioning box and sweeping the frequency range up to 30 kHz while the DAQ was configured to sample at 50 kS/s. Results from this calibration are shown in figure 4.3 revealing the flat spectrum of the entire system and the sharp roll-off before 25 kHz. Note also that the system rejects very low frequencies near DC.

To determine the sensitivity of the microphones in terms of V/Pa, a pistonphone calibrator generating a 94 dB, 1 kHz tone was placed over all microphones. The entire system, from microphone to DAQ, for the reference channel has a sensitivity of 2.2043 V/Pa or 3.1173 V/Pa (RMS). Each channel has a slightly different sensitivity, which is accounted for in the software. Since the WM-61/64 microphones are advertised as having an extremely flat frequency response curve for 30 Hz through 10 kHz, a verification of the response curve of the entire system should not be necessary but is still desired. A field calibration of the entire system's frequency response was attempted but satisfactory results were never obtained. The calibration involved sweeping a range of frequencies using strong tonal signals from a speaker and obtaining data with both a high quality microphone with known flat response and the array microphones. The ratio of the array microphone response to the reference microphone signal determines the actual response

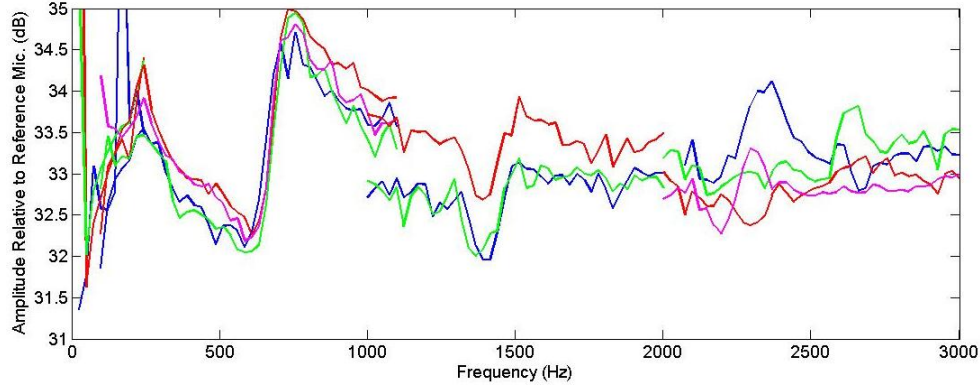


Figure 4.4: Field Microphone Frequency Response Calibration

curve of the system. During the tests, both microphones were placed in exactly the same location and data were collected once for the reference and once for the array microphone. Figure 4.4 shows the response curve of one microphone determined this way for frequencies up to 3 kHz.

The plot includes four separate calibration attempts revealing that there is some variability in the measurements and acoustic environments are difficult to measure with high precision. The results are confusing because of the very small scale variations in the curve. One would expect the system's response curve to have a general overall shape to it like the response shown in figure 4.3 instead of many local variations. Since all of the variations are within +/- 1.5 dB of the mean, they are ignored for the work in this research. While it is possible that the placement of the microphones on top of the signal conditioning boxes presents a special scenario that creates peaks and notches in the response curve, there are too many other variables in the experiment that could cause the inconsistencies such as signal multipath. Future work in frequency calibration in an anechoic environment is desired to determine the actual response.

4.5 Field Hardware

Each microphone fits inside a small project enclosure box housing the preamplifier circuitry. The sensors are positioned in the field separately, although the central sensors are

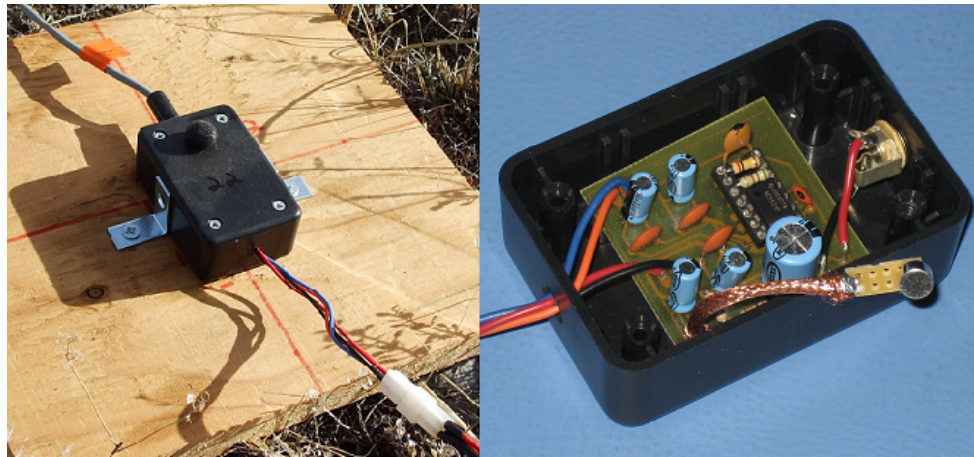


Figure 4.5: Microphone/Signal Conditioner Box [2]

mounted on a central platform for ease of field deployment. For the two arrays constructed so far, roughly half of the sensors are close enough to the center of the array to be mounted on the central platform and the other half are mounted on individual 8-10 inch square platforms. Each microphone/preamplifier box is connected to the central DAQ box by a shielded, 2-conductor audio cable as well as four 18-gauge wires for ground, +5 V, and +/- 15 V. Figure 4.5 shows one of the microphone boxes as deployed in the field on a separate platform as well as its internal circuitry.

The data acquisition, or DAQ enclosure is the central unit of the array that contains a switching power supply to convert AC power to +5 V and +/- 15 V DC and houses the data acquisition system. Each sensor channel connects to the DAQ through the front panel of the enclosure. For the first array used at the National Wind Technology Center in Boulder, a notebook computer was used in the field to control the LabVIEW data acquisition software, but for the array deployed in Bushland, Texas, a computer is able to remotely control the system. The NI 9172 chassis is controlled by a computer connected to the chassis through a USB cable. A High speed USB-to-optical fiber extender was purchased for the Bushland field tests with a range of 1,000 meters. A fiber cable connects the DAQ enclosure to a PC in the main control building. The entire DAQ enclosure is sealed and covered with a tarp to protect it from weather

in the field. A photograph of the DAQ enclosure used with the prototype array at the NWTC is shown in figure 4.6. A portion of the array as deployed in Bushland, Texas during June 2009 is shown in figure 4.7. Note the central microphones mounted on the central platform as well as a few of the separately placed sensors. Each microphone has been covered with a 3 inch diameter wind screen for further wind noise reduction. Also visible in the photograph is the conduit that houses the fiber cable that is connected to the control building.

A list of the components required for construction of the sensor units is provided in table 4.1. The major components required for the complete array are listed in table 4.2.



Figure 4.6: Data Acquisition and Power Supply Enclosure



Figure 4.7: Array as Deployed in Bushland, TX

Part	Quantity	Cost
Panasonic WM-61/64 Electret Microphone	1	\$1.82
Project Enclosure Box, Radioshack Part no. 2701801	1	\$2.29
Tie Clip Wind Screen, Radioshack Part no. 3304006	1	\$0.75
3.5 mm Audio Jack	1	\$2.99
Texas Instruments NE5534 Op-Amp	1	\$0.65
Vector Circuit Board	1	\$2.99
22 μF Electrolytic Capacitor	3	\$0.30 ea.
1 μF Electrolytic Capacitor	1	\$0.30
470 μF Electrolytic Capacitor	1	\$0.80
0.1 μF Capacitor	3	\$0.30 ea.
22 μF Capacitor	1	\$0.25
510 Ω Resistor	1	\$0.12
2.2 k Ω Resistor	1	\$0.12
10 k Ω Resistor	1	\$0.12
51 k Ω Resistor	1	\$0.12
200 k Ω Resistor	1	\$0.12
Total		\$15.24

Table 4.1: List of Microphone Sensor Components

Part	Quantity	Cost
NI cDAQ 9172 Chassis	1	\$944.00
NI 9229 Module	8	\$1,150 ea.
ThinkLogical Fiber USB Extender, KVMS.com Part no. KM-4517	1	\$895.00
SC Duplex Multi Mode 62.5 micron Fiber, 300 ft.	1	\$236.00
TRC Electronics Switching DC Power Supply	1	\$54.00
DAQ Enclosure	1	Donated
Microphone/Signal Conditioner Boxes (see table 4.1)	32	\$15.24 ea.
Brueel and Kjaer 90 mm Diameter Wind Screens, Part no. UA-0237	18	\$30 ea.
2-Conductor Shielded Audio Cable	1,140 ft.	\$22.50/100 ft.
18 ga. Spooled Wire	2,400 ft.	\$12.95/100 ft.
Power Connector: Pins, Mouser Part no. 538-39-00-0039	320	\$0.09
Power Connector: Pins, Mouser Part no. 538-39-00-0041	320	\$0.09
Power Connector: Plug Housing, Mouser Part no. 538-39-01-2041	80	\$0.45
Power Connector: Plug Connectors, Mouser Part no. 538-39-01-2040	80	\$0.30
Power Connector Branches, Mouser Part no. 517-905-BOX 50 ct.	4	\$9.25 ea.
3.5 mm Audio Plug	64	\$1.95 ea.
Assorted Lumber and Hardware		\$500.00 (est.)
Total		\$16,401.00
Cost per Channel		\$512.51

Table 4.2: List of Array Hardware Components

Chapter 5

Field Experiments

Two main arrays were designed during 2009 and 2010. The first was a 32-sensor array designed specifically for a 36.4 meter hub height, 21 meter rotor diameter turbine located at the National Wind Technology Center in Boulder. This array was designed to analyze frequencies ranging from 125 Hz to 8 kHz with resolution between 1.75 meters and 7 meters, depending on the frequency of interest. The array consisted of three “sub-arrays” containing 16 sensors each, optimized for 3.5 meter resolution at 250 Hz, 1 kHz, and 4 kHz. This array was used for testing at the NWTC between July 2008 and May 2009 [62]. A second array, exhibiting improved resolution and sidelobe rejection, was designed for application to the 22.86 meter hub height, 18 meter rotor diameter turbine/blade combination at the Agricultural Research Service site in Bushland, Texas [63]. A more strategic approach was used for the design of this second array, instead of the primarily trial-and-error method used for the design of the first array. The “Bushland” array uses 45 sensors to observe the band between 75 Hz and 8 kHz. With the 32 channel hardware limitation, the array must be configured in either the low-mid or mid-high frequency configuration. The mid-low configuration can be used for frequencies up to 2 kHz and the mid-high configuration is used for frequencies above 500 Hz. All beamforming performed in this chapter uses time samples of 41 milliseconds that are transformed into the frequency domain using the FFT. Therefore all FFT bins used are 24.41 Hz wide.

The file *FreqBeamformerPlanar.m* in appendix A contains the beamformer code used to provide the results for the NWTC array. The more advanced beamforming code used for

the Bushland array is not included in this thesis because of its length. The “complete” de-Doppler correction technique, described in section 3.3.1 has not been widely used yet because beamforming attempts employing it have resulted in less power response than the standard method. The time-shift based partial correction technique described in section 3.3.2 is very successful however and is used as part of the standard beamforming procedure.

5.1 National Wind Technology Center Prototype Array

5.1.1 Array Design

Broadband acoustic arrays usually consist of a large number of sensors, on the order of 100 [38, 39]. When a large number of sensors are used, the array is usually a circle or ellipse with high sensor density. For an array like this, the sub-array used for any given frequency is usually a circle or ellipse with radius that scales inversely with the frequency analyzed. Given a 32 sensor restriction, it is not possible to create a dense array shape that is large enough to provide necessary resolution at low frequencies. The design philosophy used for this array involved using two concentric rings of sensors, an outer ring for excellent resolution, and an inner ring of closely spaced sensors to suppress sidelobes. By adjusting the ratio of inner to outer ring radius, it was found that a ratio of 4-to-1 provided acceptable sidelobe rejection. To make efficient use of the limited number of sensors, it was decided that the outer ring of the smallest sub-array would act as the inner ring of the middle sub-array, and likewise for the middle and large sub-arrays. The size of the middle sub-array was chosen to provide a resolution of a few meters at 1 kHz, and therefore the small and large sub-arrays behave equivalently at 4 kHz and 250 Hz respectively. The array was designed to be placed one hub height away from the turbine and therefore the circular array shape was stretched to maintain a circular beam pattern when steered toward the hub as described in section 2.3.1. The array was also tilted toward the right, or downward, half of the rotor to capture the dominant aeroacoustic noise present on that half. The final array shape as deployed at the NWTC is shown in figure 5.1, illustrating its size and position relative

to the turbine. Note the concentric ellipses of sensors. Exact sensor locations are provided in appendix B.

Since the array consists of three sub-arrays that are optimized for frequencies two octaves apart from one another, a compromise must be made for frequencies other than 250 Hz, 1 kHz, and 4 kHz. Obviously any frequencies below 250 Hz are best observed using the large sub-array and the range above 4 kHz is best observed with the small sub-array. The mid sub-array is used for frequencies between 500 Hz and 2 kHz, an octave on either side of the intended center frequency. To capture the entire band from 125 Hz to 8 kHz, each sub-array is responsible for an octave below to an octave above its center frequency. For the lower octave, resolution will be adversely affected but sidelobes will be pushed farther out since the array pattern will scale larger. The opposite will be true for the upper octave. Resolution will improve but the array pattern will shrink, causing sidelobes to move closer to the mainlobe. The array's sidelobe rejection at 1 kHz is 7.5 dB when using diagonal elimination. There is a prominent sidelobe ring about 7 meters from the mainlobe.

5.1.2 Field Validation

To test the array's performance, a variety of tonal and broadband signals were broadcast through a small speaker to simulate a point monopole. Several tests were performed with a small speaker positioned at various locations near the turbine rotor using an aerial lift and results were compared with theoretical simulations to determine the level to which the array, as positioned in the field, behaved like the intended array. For the NWTC array, microphones were positioned using a laser distance meter to determine distance and a laser level to determine elevation offsets. The laser distance meter, along with staked out x and y axes, was used to triangulate the positions of the sensors in the field. Instead of positioning the smallest two ellipses of sensors individually, a 4-by-8 foot platform was used to mount these sensors on. Since the position error tolerances of the smaller ellipses are lower, it is important that they are placed with precision, and mounting them on a platform provides better accuracy than placing them in

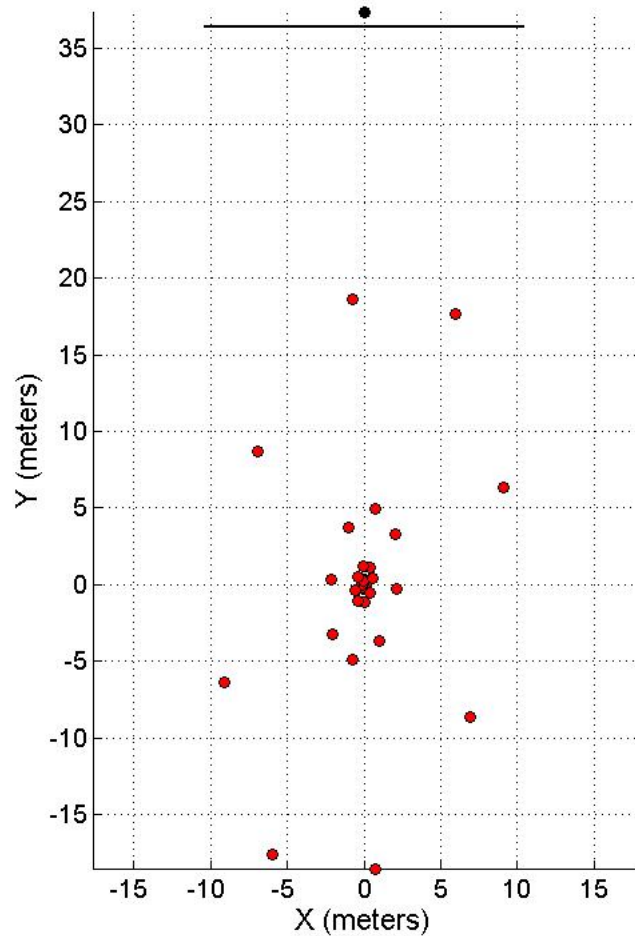


Figure 5.1: 32-Sensor Prototype Array Shape

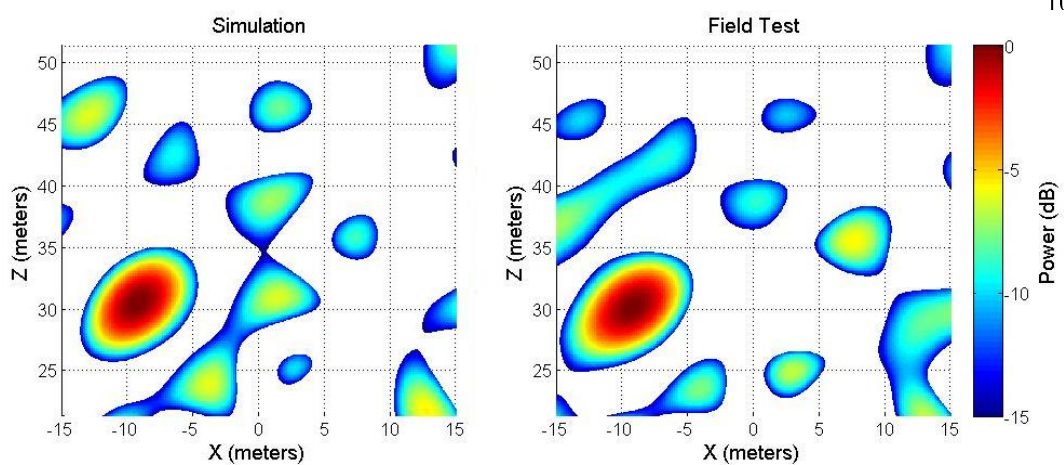


Figure 5.2: Small Sub-Array Pattern, 3 kHz Tone

the field individually. Finally, the minor elevation offsets of the individual microphones due to the rough terrain were measured with the laser level and accounted for in the software. Figure 5.2 compares the simulated array pattern with the result from field testing using a strong tonal 3 kHz signal and the small sub-array. As with all of the field verifications of array pattern, the resolution remains about the same as the simulated value and some sidelobes are higher than intended. The amount by which sidelobes are elevated during field verification is used as a metric to judge the quality of the array placement in the field. Surprisingly, for the small sub-array the array pattern in the field is about the same if not slightly improved over the theoretical pattern. The basic sidelobe structure remains but with some sidelobes at higher levels and some at lower levels.

Results for the mid sub-array are shown in figure 5.3. Here, the array pattern is also very similar to the intended pattern. The sidelobe to the lower right side of the mainlobe has increased by 1.64 dB in the field test, however.

A similar validation was performed for the large sub-array. Results are provided for a 250 Hz tone as well as a 500 Hz tone an octave higher. The comparisons between theoretical and actual array patterns are shown in figures 5.4 and 5.5. Once again, the array patterns determined through field experimentation yield roughly the same sidelobe structures as the simulations but

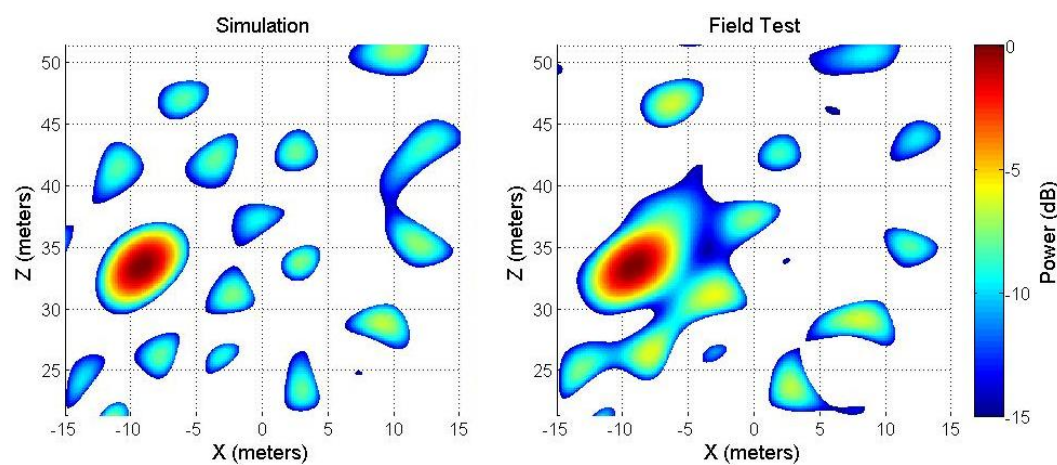


Figure 5.3: Mid Sub-Array Pattern, 1 kHz Tone

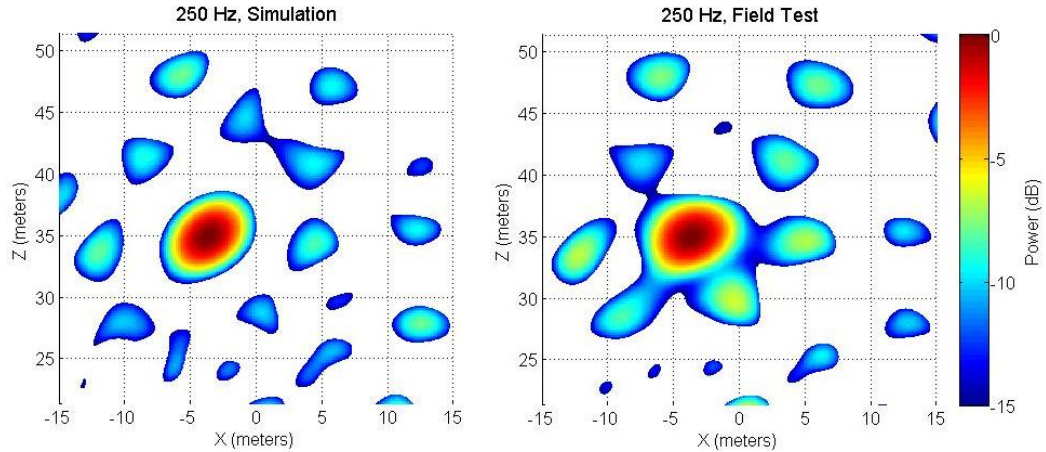


Figure 5.4: Large Sub-Array Pattern, 250 Hz Tone

with higher sidelobes. The prominent sidelobe to the right of the source in the 250 Hz pattern is 1.3 dB higher than intended. The 500 Hz field test reveals that the sub-array behaves rather poorly an octave higher than its intended frequency. The obvious prominent sidelobe on the 500 Hz field pattern is only 2 dB below the source power! The poor performance of the array at relatively high frequencies can be expected. As was shown in section 3.2, errors in beamforming parameters such as sensor position affect higher frequency, shorter wavelength signals more. For this same reason, frequencies below the array's central frequency provide excellent array pattern fidelity. Caution should be exercised when beamforming with an array size intended for lower frequencies and it may be more favorable to use the mid sub-array to examine frequencies near 500 Hz instead of the low sub-array.

Instead of just analyzing strong tonal signals in the field, it is important to test the array's ability to operate in very low SNR conditions, since that is one of the benefits of using an array in the first place. The plots in figure 5.6 demonstrate the small sub-array's abilities when observing very weak signals. For reference, the figure includes a comparison of theoretical and practical results for a 3 kHz pure tone. Three frequency bins near 3 kHz are analyzed for a white Gaussian noise signal. The signal contains a flat spectrum from DC to 12.5 kHz and the power in each bin is estimated to be 512 times lower than for the pure tone cases. Obviously

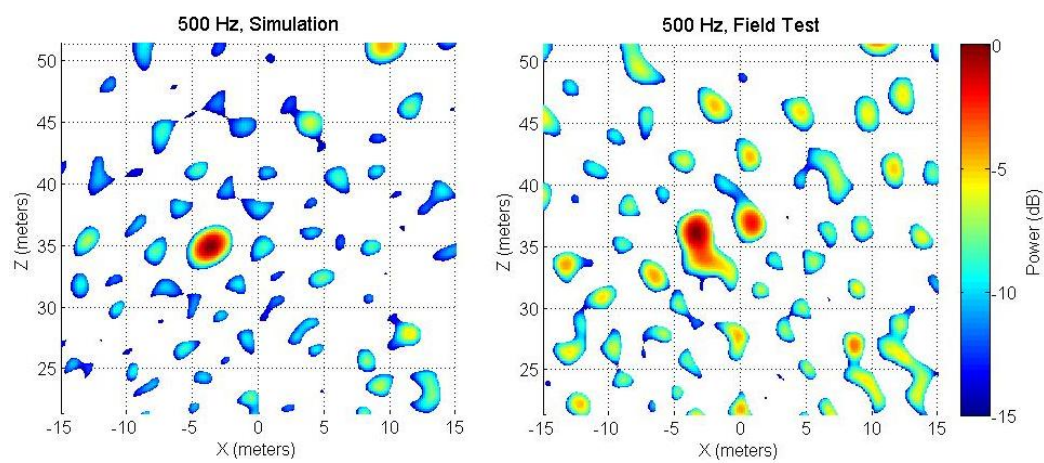


Figure 5.5: Large Sub-Array Pattern, 500 Hz Tone

the array does not perform very well when observing this very weak signal, but it *is* able to locate the speaker on the aerial lift. The fact that it can detect the presence of the source at all is testament to the array's low SNR capabilities.

5.2 Bushland, Texas Array

5.2.1 Array Design

This section will explain the design choices that led to the final array design for the 100 kW wind turbine with BSDS blades located in Bushland, Texas [40, 43, 63]. This turbine has a hub height of 22.86 meters and a rotor radius of 8.97 meters. Therefore, the array is centered 22.86 meters upwind from the rotor. The goal of the acoustic observations is to compare trailing edge noise near the blade tips to inboard flatback noise produced by the blunt trailing edge of the blade. The “flatback” section of the trailing edge that is of interest is located approximately 2-3 meters from the hub and occupies about 2-3 meters of blade before terminating 4 meters from the tip. Resolution must be good enough to separate acoustic sources located at the tip and on the flatback section. The other main acoustic sources are the generator and gearbox in the nacelle, which for this turbine are unusually loud. A design consideration is that spurious sidelobes resulting from nacelle noise near the hub should not interfere with any of the possible acoustic sources of interest.

The frequency band of interest for this experiment is from 50Hz to 8kHz. The flatback portion of the blades is expected to produce most of its acoustic energy between 50Hz and 200Hz [40]. The tip noise on the other hand is expected to contain higher frequencies in the range of 250Hz to 8kHz [1]. Rather than designing the array to observe the entire band of frequencies at once, it was decided that the array would consist of three sub-arrays, much like the NWTC array. One sub-array is for low frequencies below 500 Hz, one is for mid frequencies from 500Hz to 2kHz, and the final sub-array is optimized for frequencies from 2kHz to 8kHz and possibly higher. Also like the NWTC array, the sub-arrays are designed for 250Hz, 1kHz, and 4kHz and

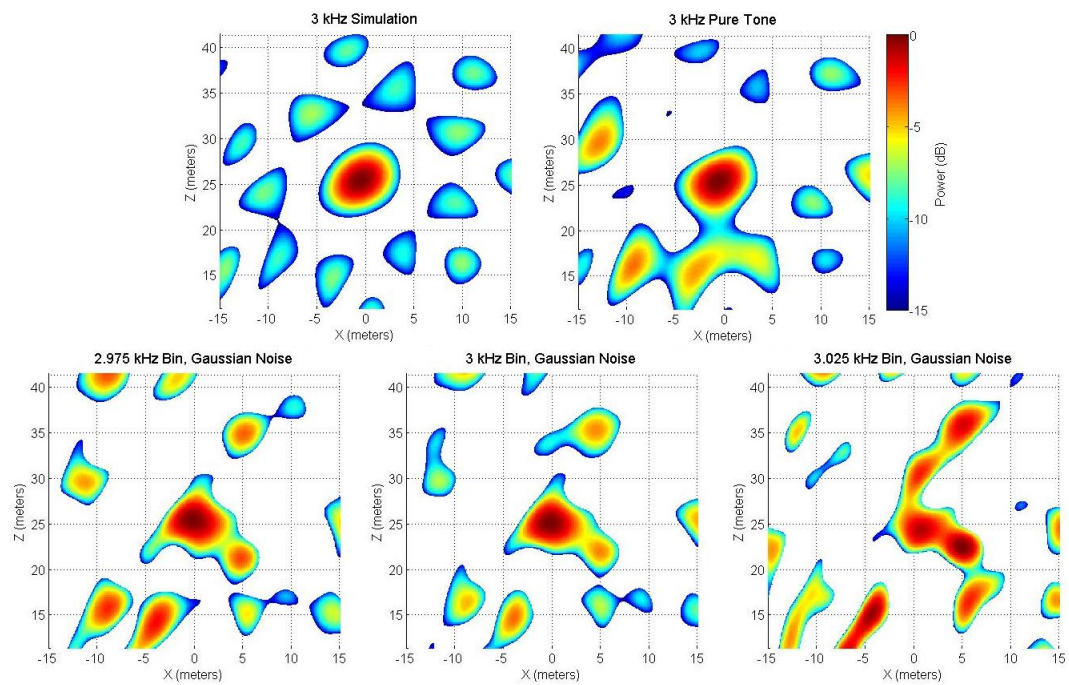


Figure 5.6: Low SNR, White Gaussian Noise 3 kHz Array Patterns

each one is responsible for observing frequencies ranging from one octave lower to one octave higher than the center frequency. Resolution will therefore be anywhere from twice to half of the original value at the center frequency and sidelobes will be located anywhere from half of to twice the original distance from the mainlobe.

The final design uses between 19 and 26 sensors for each sub-array. The array consists of two concentric ellipses per sub-array. The inner ellipse of the larger (low frequency) array is used as the outer ellipse of the mid array. Likewise the inner ellipse of the mid array is the outer ellipse of the smallest array. The final design does not allow for each of the sub-arrays to be positioned simultaneously because two sub-arrays utilize all 32 microphones. Therefore the array is either in the low-mid or mid-high configuration and 13 sensors must be manually relocated to switch between configurations. The array is therefore either configured to observe low frequency flatback and low frequency trailing edge noise near the blade tips or to observe higher frequency trailing edge noise near the blade tips.

A closer look at the theory behind the NWTC array shape led to an improved array shape based on the same concentric ellipse concept. Figure 5.7 shows the range of spatial frequencies projected onto the array center, one hub height away from the tower, caused by a 1 kHz source in the 30 meter-by-30 meter scan plane centered around the hub of the Bushland turbine. This guides the design of the array pattern, dictating the necessary width of the mainlobe and the sidelobe positions in the spatial frequency domain to meet the design requirements. The difference in $k_{p,x}$ between the hub and the right blade tip is about 5. The change in $k_{p,y}$ between the hub and the lower blade tip is about 2.5.

The methodology of designing the array involved looking at the Fourier transform of the outer ellipse and the inner ellipse separately and identifying characteristics that might contribute toward low sidelobe levels. Eventually, it was discovered that an inner ellipse of at least 6 sensors and an outer ellipse of 13 sensors scaled 3.4783 times larger than the inner ellipse yielded the best array shape using only 19 sensors for each sub-array. The size of the outer most ellipse was chosen to be the same size as the outer ellipse for the NWTC array. This way, since the Bushland

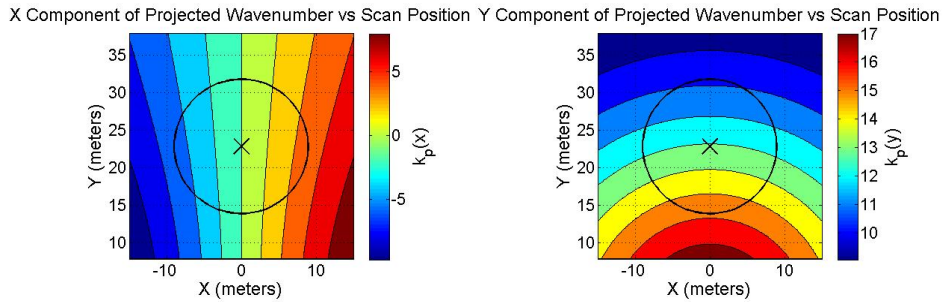


Figure 5.7: Projected Spatial Frequencies from 1kHz Source on Scan Plane of Bushland Array

turbine is smaller and the rotor is closer to the array, resolution will improve (equivalent array sizes maintain the same angular resolution and therefore spatial resolution improves the closer the array is to the scan plane). As mentioned earlier, $k_{p,y}$ changes twice as slow across the scan plane as $k_{p,x}$, which means the major axes (y direction) of the ellipses are twice the length of the minor axes, causing the resulting Fourier transform to have a mainlobe twice as wide in the $k_{p,y}$ dimension.

Furthermore, in order to optimize the array performance to the right side of the rotor plane where most acoustic noise is expected, the ellipses are tilted slightly to the right. Figure 5.8 shows the resulting Fourier transforms, or array patterns, of the inner, outer, and complete mid sub-array. The array pattern of the outer ellipse contains a mainlobe followed by alternating positive and negative sidelobe rings. The inner ellipse produces a wider mainlobe with a negative sidelobe ring surrounding it and multiple sidelobes. For a case where the sidelobes are exact copies of the mainlobe, like with the inner ellipse, they are called *grating lobes* [4]. The wide mainlobe of the inner ellipse helps cancel the first negative sidelobe ring of the outer ellipse and the negative sidelobe ring of the inner ellipse partially cancels the second positive sidelobe ring of the outer ellipse. By experimenting with different ratios between outer and inner ellipse, it was discovered that the ratio of 3.4783 provided the best sidelobe cancellation, instead of the ratio of 4 used in the NWTC array.

Another strategy used for this array shape was choosing how many sensors to include in

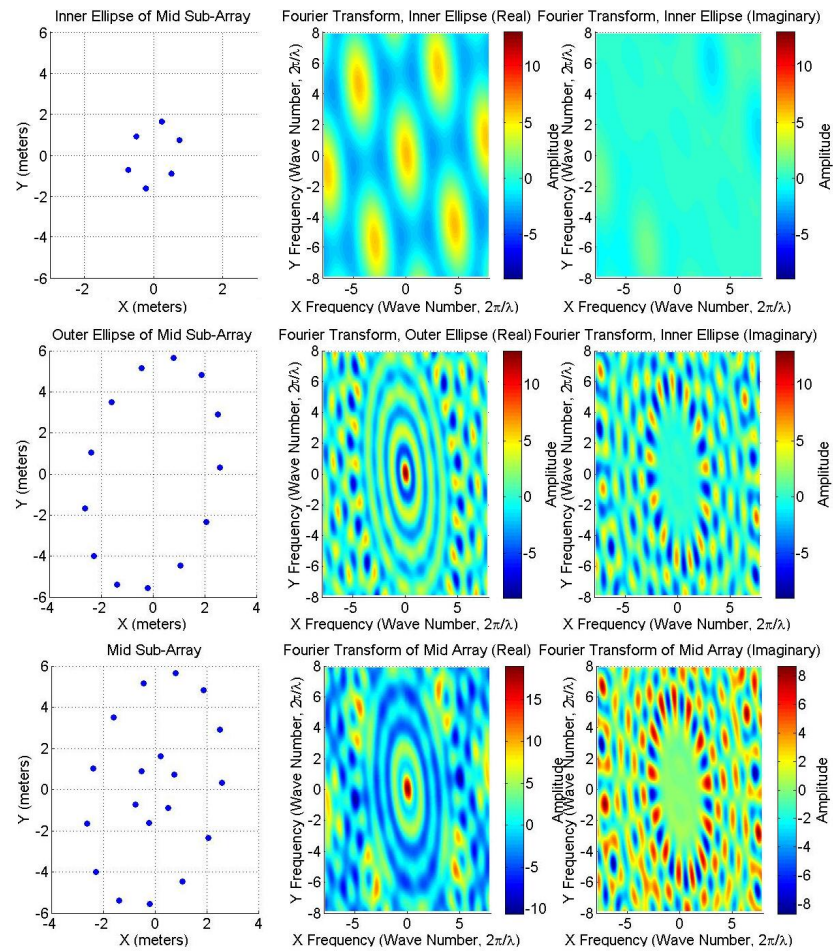


Figure 5.8: Fourier Transforms of Mid Sub-Array

the inner and outer ellipses. For the NWTC array, 8 sensors were chosen for each ellipse so that all sub-arrays could be used to collect data simultaneously. The reasoning behind choosing an odd number of sensors for the outer ring is explained in section 2.3.2 on the co-array. An even number of sensors provides too much structure in the array and coincidental phase matching leads to excessively high sidelobes. The high sidelobes near the mainlobe in the array patterns of the original NWTC array (fig. 5.2 - 5.4) are present because the sidelobe structure of the 8-element outer ellipse consists of discrete sidelobes instead of the continuous rings that can be seen in the outer ellipse pattern in figure 5.8. The discrete sidelobes do not perfectly cancel out when combined with the inner ellipse's array pattern and high sidelobes remain near the mainlobe. Smooth sidelobe rings exist when the ellipse contains a higher sensor density. It was discovered that 13 sensors provided the fewest number of sensors that were necessary to provide the “clean” region of the array pattern near the mainlobe. Increasing the number of sensors in the inner ellipse beyond 6 only slightly improves the array pattern and adversely impacts resolution.

This approach to the final array design neglected the imaginary parts of the array patterns which did not provide any useful structures that could cancel one another. Most of the major sidelobes present in the final array pattern are due to the imaginary parts of the array patterns which do not cancel each other out in a productive manner as can be seen in figure 5.9.

The final array pattern that results from the array shape after conventional beamforming is the magnitude of the real and imaginary parts of the array pattern. This array pattern is shown in figure 5.9. The resolution, or mainlobe width, of the pattern is 1 radian in the y dimension and 0.5 radians in the x dimension. The two sidelobe rings nearest to the mainlobe are suppressed by more than 10.6 dB while the third ring of sidelobes is suppressed by 7.2 dB. Larger sidelobes are present farther away from the mainlobe, but the idea is that these will not interfere with any acoustic sources of interest present on the scan plane because of their distance from the mainlobe. A design choice in this array was to leave the area immediately surrounding the mainlobe of the array pattern clear of any significant sidelobes. This allows the

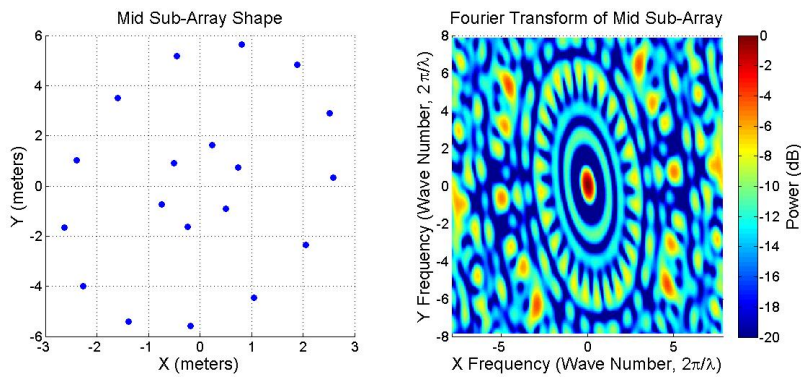


Figure 5.9: Final Array Pattern for Mid Sub-Array

total energy resulting from a close group of point sources to be integrated without including spurious sidelobes.

As mentioned before, the array can be configured in the low-mid or mid-high layouts. These two configurations are shown in figure 5.10. The sensors in the inner ellipse of the low-mid configuration are not actually evenly spaced because they are 6 out of the 13 sensors that make up the outer array of the mid-high configuration. This uneven sensor distribution does not change the array pattern significantly. An interesting result of the array configurations is that in the low-mid arrangement, the low sub-array can consist of the outer ellipse and either 6 sensors from the inner ellipse or the entire inner ellipse. When the latter option is used, more weight is placed on sensors that are closer to the center of the array, which harms resolution but increases sidelobe rejection. Another option is to weight the steering vector components of the inner ellipse by 0.5. This way the inner ellipse contributes about as much as it does when only 6 sensors are used but the advantage is that since more sensors are used, sensor placement errors and noise are averaged out better. Similarly, in the mid-high configuration, the mid sub-array can use either 19 or 26 sensors. Sensor locations for the two configurations are provided in appendix B.

The array pattern of the mid sub-array consisting of the full inner ellipse, with weight $w = 1$ for each sensor, is shown in figure 5.11 for comparison with the 19-sensor array pattern in figure 5.9. Resolution clearly increases in the 26-sensor mid sub-array, although only by a

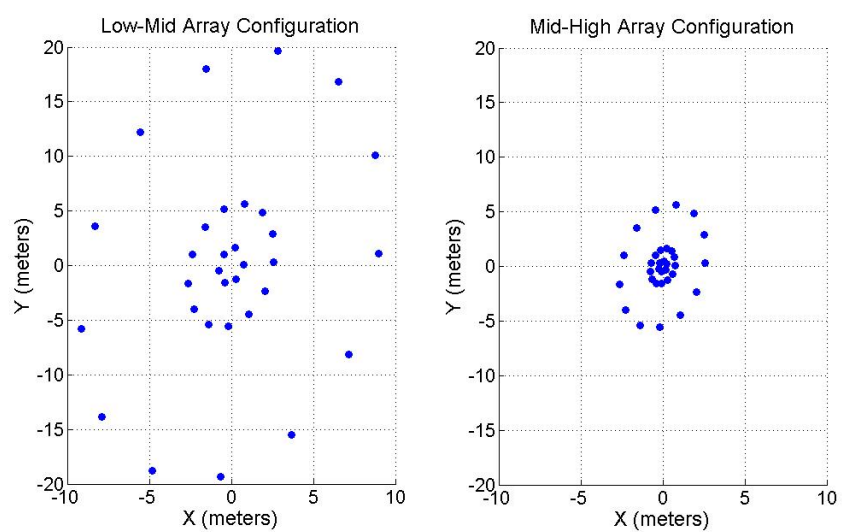


Figure 5.10: Array Shape Configurations

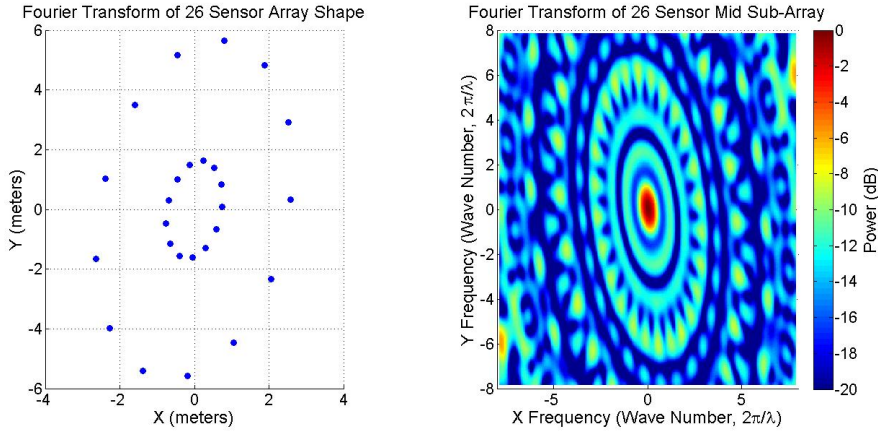


Figure 5.11: Array Pattern of 26 Sensor Mid Sub-Array

factor of 1.2. The third ring of sidelobes, which is the first significant sidelobe ring, contains levels suppressed by only 7.2 dB using the 19-sensor array but for the 26 sensor array, they are suppressed by 9.48 dB. All remaining sidelobes are suppressed by at least 9.25 dB in the 26-sensor array.

The array pattern that is actually observed in a noise map produced by beamforming is a function of scan plane location rather than projected wavenumber. Figure 5.12 presents the array patterns produced by a source at the hub for the low sub-array, mid sub-array, and high sub-array at the center frequencies and at one octave higher and lower than the center frequencies. These plots therefore illustrate the nominal array pattern as well as the array patterns that result from observing the boundaries of the two-octave band each sub-array is responsible for. Some of the plots differ noticeably from the Fourier transform based array pattern shown previously. This is due to the far field approximation that is made when treating the array pattern as the Fourier transform of the array shape. In general, even for the low sub-array which is most liberally considered to be in the far field of the source wave field, the approximation holds well. At the center frequencies, the first significant ring of sidelobes is positioned near the blade tips. At the octave higher than the center frequency, this ring of sidelobes is positioned at about half the blade span. Resolution at the center frequency for the three sub-arrays is 2.3 meters for the low array, 1.9 meters for the mid array, and 1.5 meters

for the high array, great improvements over the 3.5 meter resolution accompanying the NWTC array.

5.2.2 Field Validation

When the Bushland array was positioned in the field in summer 2009, a new method was used to measure the sensor positions. Instead of using a laser distance meter to triangulate sensor positions, the sensor positions were determined in terms of their polar coordinates. A surveying transit was used to determine the angular offset from a staked out y axis for each sensor and a tape measure was used to locate the correct radial coordinates. In the same way as for the NWTC array, the two smallest ellipses of sensors are mounted on a central platform spanning 6 feet-by-12 feet. The elevation offsets were determined by using the surveying transit as well. An array validation procedure similar to the one described earlier was used for this array. A small speaker was positioned at various locations on the rotor plane using an aerial lift. Figures 5.13 through 5.15 show comparisons of the theoretical and actual array patterns for the central and upper octave frequencies for each sub-array. An octave above each center frequency is examined because of the poor performance that was seen with the NWTC array at these frequencies (as shown in fig. 5.5). The comparisons for the small sub-array, shown in figure 5.13, reveal that the 4 kHz array pattern experiences worse performance than the simulation, with a sidelobe as high as 5.83 dB close to the source peak instead of the extremely clean region predicted in the simulation. Surprisingly, the 7.615 kHz array pattern exhibits exceptional performance compared to the simulation. The sidelobe structure remains nearly the same, with sidelobes not exceeding 7.3 dB near the peak. One explanation for the relatively strong performance at the higher frequency compared to the standard frequency is that atmospheric turbulence distorted the signals more during the 4 kHz data collection. Only 8 second datasets were used for beamforming and that may have not been long enough to average out the atmospheric turbulence.

A validation of the mid sub-array is shown in figure 5.14 for 1 kHz and 2 kHz. The 1 kHz

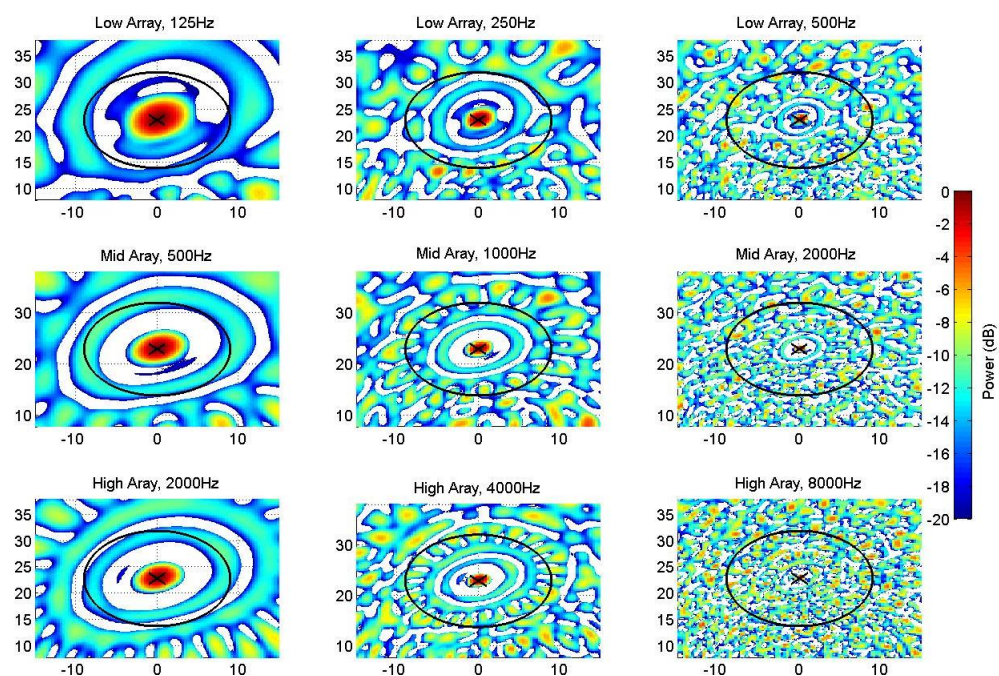


Figure 5.12: Simulation of Noise Maps Produced by Monotone Sources Located at Hub

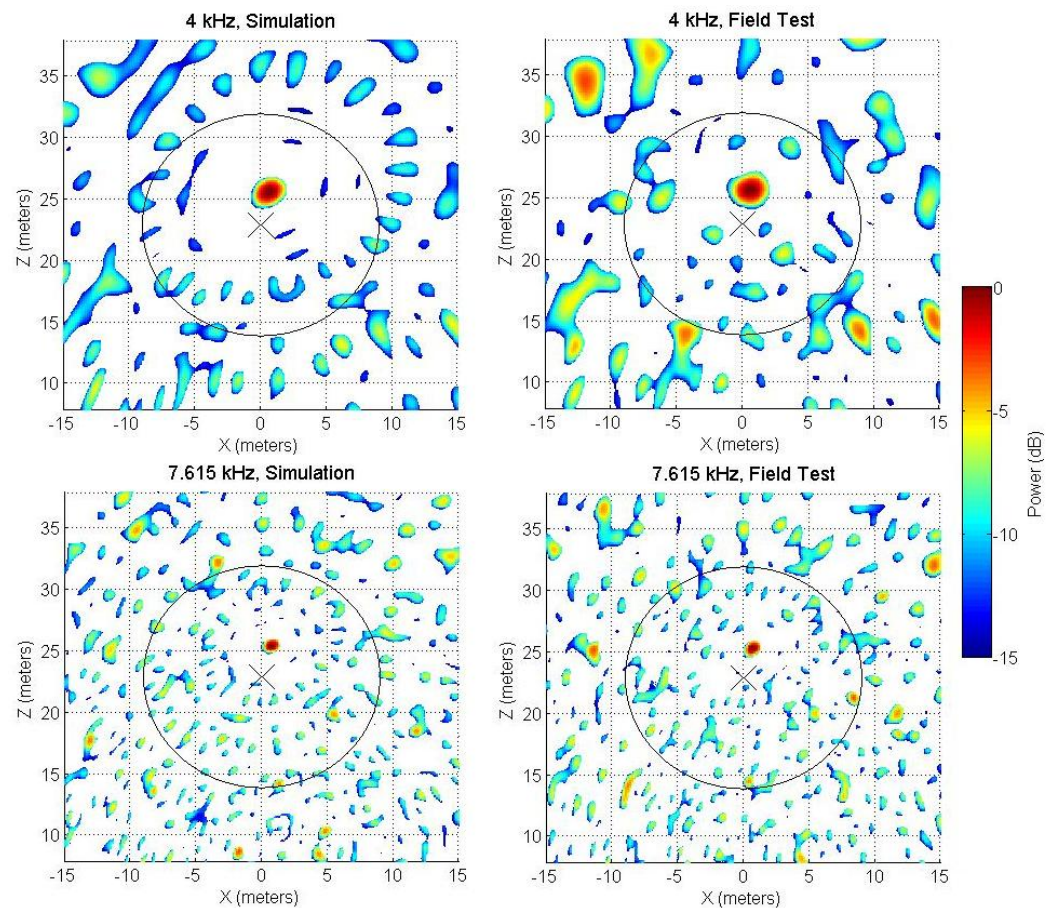


Figure 5.13: Small Sub-Array Patterns, 4 kHz and 7.615 kHz Tones

field array pattern is a drastic improvement over the 4 kHz pattern with the closest significant sidelobe being a 6.91 dB sidelobe 10 meters from the source. Worse performance is experienced for the 2 kHz array pattern, with a 4.05 dB sidelobe only 5 meters from the source. The results for the low sub-array are shown in figure 5.15 for 250 Hz and 500 Hz. At 250 Hz, the field array pattern behaves reasonably well compared to the simulation, with only a slightly distorted mainlobe raising concern. The prominent sidelobe on the lower left side of the rotor actually decreased, from 4.34 dB to 4.64 dB! At 500 Hz, the sidelobe structure is almost identical to the simulated case with the prominent sidelobe to the lower left side of the source elevated from 4.86 dB to 3.34 dB raising the most concern.

5.2.3 Field Testing and Results

During August 2009, data were collected using the low-mid configuration of the array and later analyzed. This section provides some of the initial results, demonstrating the array's performance in the wind turbine aeroacoustic application it was intended for [63]. All SPL values are reported in dB referenced to the standard $2 \cdot 10^{-5}$ Pa. Whereas the wind turbine at the NWTC used to test the first array is a direct drive model, the machine in Bushland contains a very noisy gear box. This unwanted characteristic is shown in figure 5.16, which shows overall 45-second average noise maps for a range of discrete frequencies. Clearly the noisy nacelle of the turbine dominates the overall averages for frequencies below 1 kHz. At 1 kHz, trailing edge noise near the blade tip can be seen for blade azimuth angles between 90 and 180 degrees. At 2 kHz, the trailing edge noise is dominant and the hub noise no longer interferes with aeroacoustic noise. One of the main objectives of the Bushland field experiments is to observe low frequency, inboard noise between 50 Hz and 250 Hz and the strong source at the hub interferes with this region, especially for frequencies below 250 Hz when resolution increases.

Figure 5.17 presents the results for a 60 second period of turbine operation with 9 m/s wind speeds for the 250 Hz 1/3-octave band. The results are separated by blade azimuth angle instead of displaying overall averages. The azimuth angle of the blade under investigation

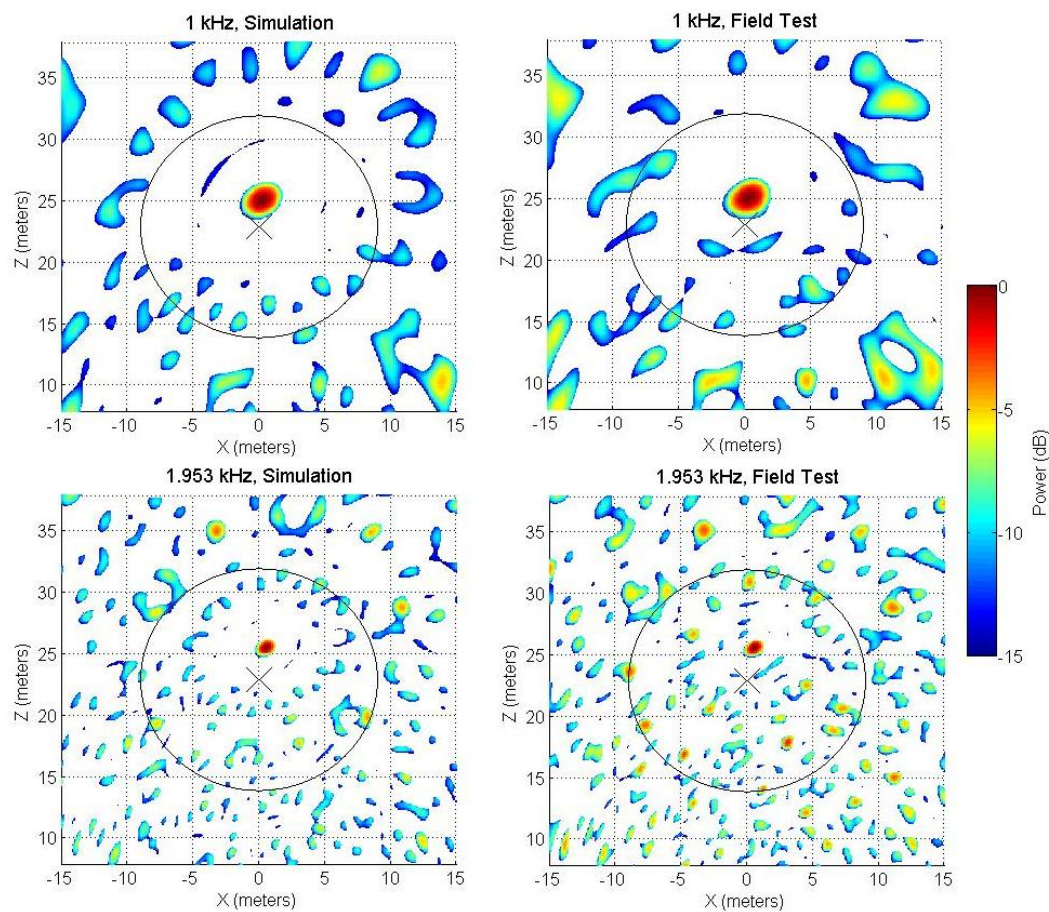


Figure 5.14: Mid Sub-Array Patterns, 1 kHz and 2 kHz Tones

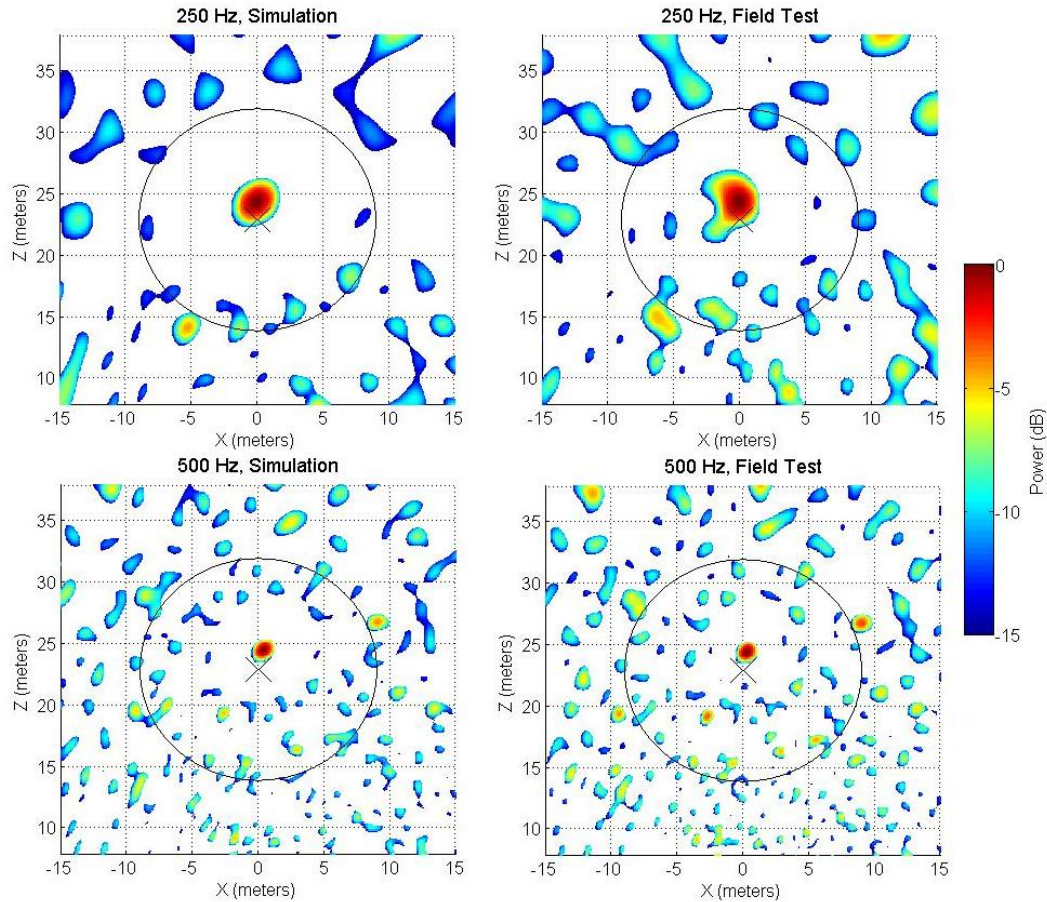


Figure 5.15: Large Sub-Array Patterns, 250 Hz and 500 Hz Tones

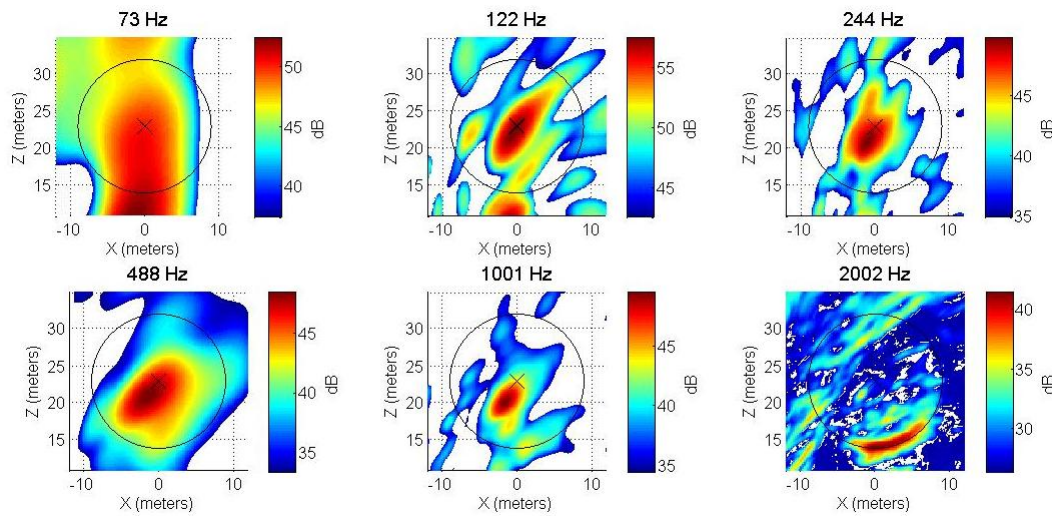


Figure 5.16: 45 Second Average Noise Maps, Mid and Large Sub-Arrays

is determined through an azimuth DAQ channel acquired from the wind turbine control and monitoring system and knowledge of the propagation time between blade and array. As described in section 3.3.2, the datasets are time-shift steered toward a point on the blade of interest before beamforming to help mitigate Doppler effects. It should also be noted that as with all results shown in the following figures the turbine rotor has a yaw angle of 25 degrees to the right of the axis between the tower and array center. This is accounted for in the software and the modified scan plane is tilted accordingly. Furthermore, the rotor has a vertical tilt angle of 4 degrees which is accounted for as well. It is difficult to determine which part of the noise maps are from inboard blade noise and which parts are from the nacelle. It is highly likely that inboard blade noise exists between 60° and 120° and again between 210° and 240°. There is possible inboard noise near 0° as well. Interestingly, noise appears to be present at a very wide range of azimuth angles instead of just the downward half of rotation where noise near the blade tips is strongest.

The mid sub-array was used to collect the 56 second, 1.25 kHz 1/3-octave band during 9 m/s wind speeds shown in figure 5.18. For these azimuthally dependent plots, the scan plane rotates with the blade under investigation and the bottom of each noise map represents the leading edge side of the blade. The plots show the averages of the three blades. The dominant source in these noise maps is the hub, present at the left side of the maps for azimuth angles of 105° through 330°. Trailing edge noise near the blade tip is visible between az. angles of 45° and 210° with peaks at 150° and 180°. It is likely that the peak at 180° is due to unsteady loading from the tower. Because of the 25° yaw angle, the peak trailing edge noise is present at 150° because that is the angle at which the blades have the highest velocity relative to the microphones. Figure 5.19 shows the trailing edge noise at the peak azimuth angles separated by blade number, revealing that each blade behaves essentially the same in the 1.25 kHz 1/3-octave band with a slightly stronger presence from blade 3.

Since an azimuth angle of 150° produced the strongest trailing edge noise, the spectra of noise near the blade tips for each blade at this azimuth angle at wind speeds of 7 m/s and 9 m/s are shown in figure 5.20. The data presented in figure 5.20 is from the same 56 second

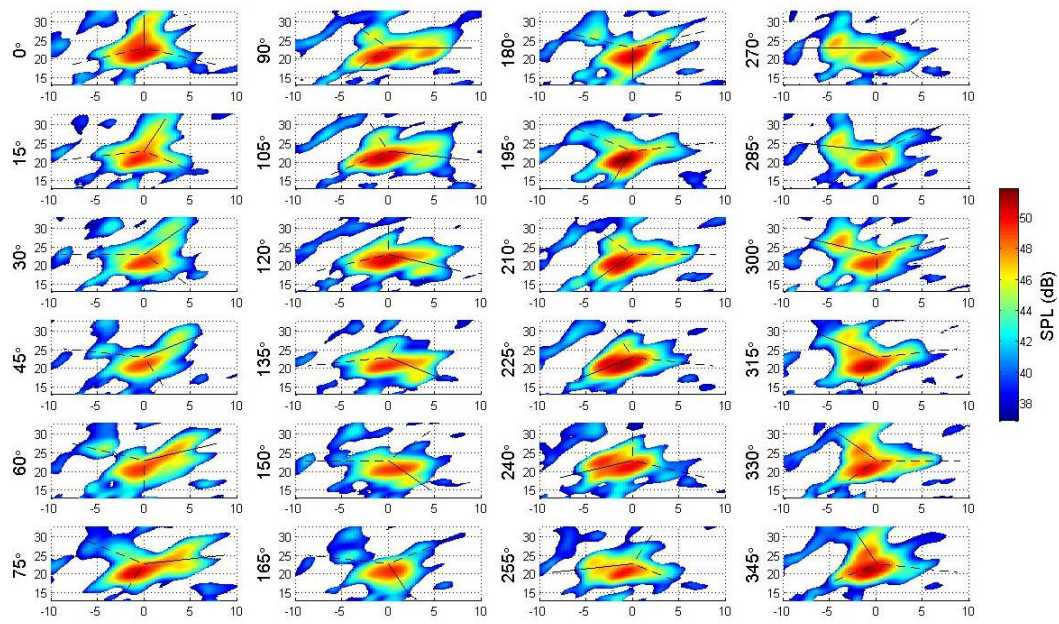


Figure 5.17: Dependence on Rotor Azimuth Angle, 250 Hz 1/3-Octave Band, 60 Second Avg.

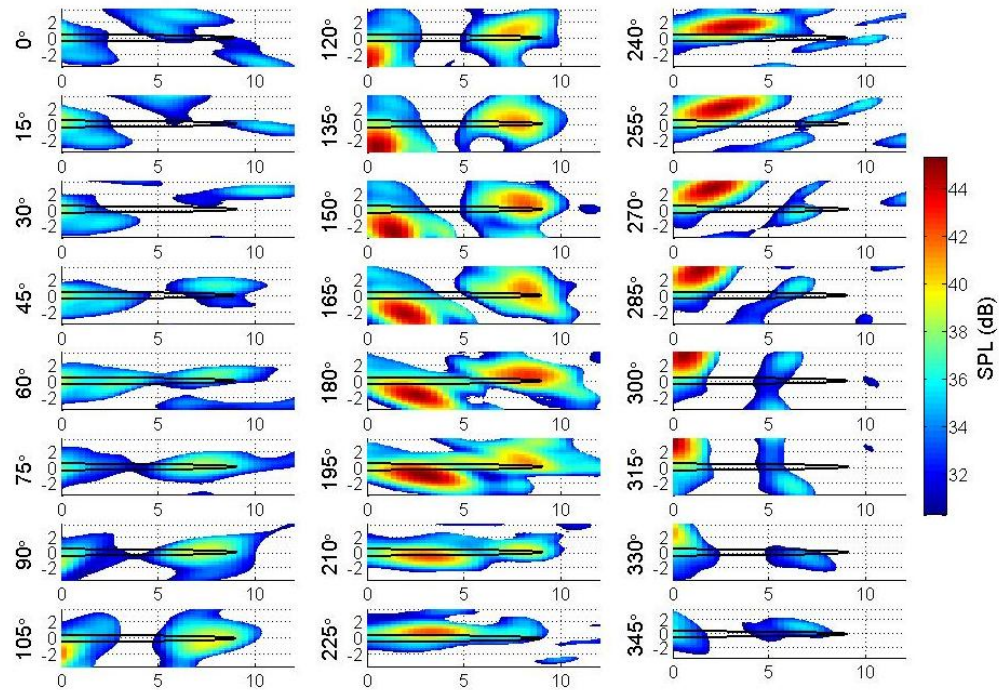


Figure 5.18: Rotating Scan Plane, 1.25 kHz 1/3-Octave Band, 56 Second Avg. of All Blades

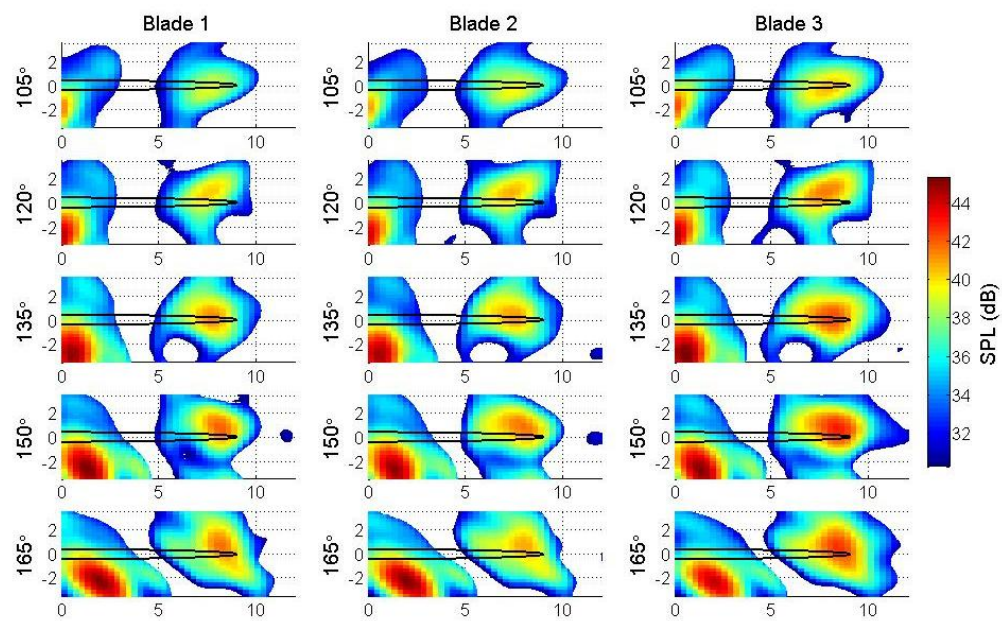


Figure 5.19: Peak Noise Positions, 1.25 kHz 1/3-Octave Band, 56 Second Avg. of Individual Blades

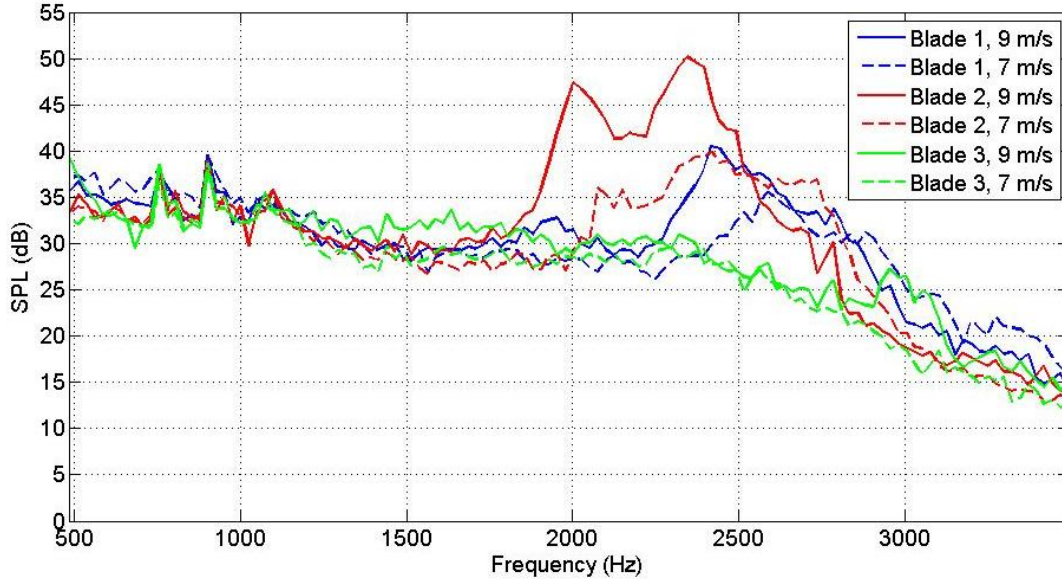


Figure 5.20: 150 degree Azimuth Angle Tip Region Spectrum, Mid Sub-Array

dataset that is shown in figures 5.18 and 5.19, spanning about 51 complete revolutions. There are several interesting trends in this plot. First of all, it appears that there is still a strong noise presence around 500 Hz, although analysis has shown that the noise sources move closer to the inboard part of the blade for these lower frequencies. Second, there appear to be two strong tonal peaks at 756.8 Hz and 903.3 Hz present at both wind speeds for all blades. Third, there are very distinct peak regions for two of the blades between 2 kHz and 3 kHz. Blade 2 exhibits the strongest signature here between 1880 Hz and 2808 Hz. Blade 1 also shows a strong signature between 2271 Hz and 3003 Hz. Blade 3 reveals no peak in this region, instead decaying around 2300 Hz. It is interesting that the high frequency peak regions are very dependent on wind speed. The peak bands for blades 1 and 2 agree with field observations that two of the blades exhibit a loud swishing sound while one of them is relatively quiet.

5.2.3.1 Application of Advanced Beamforming Techniques

The Robust Adaptive Beamforming (RABF) and MUSIC algorithms, described in sections 2.4.2 and 2.4.3, have been applied to some of the field data collected in August 2009. Both

techniques help tremendously with improving resolution and RABF may be able to be used to determine source power as well. MUSIC, which relies on determining where noise sources are *not* located and inverting the final noise map, does not provide any useful information about the power of the signal propagating from a particular direction, but does an excellent job resolving closely spaced source positions. An application of MUSIC is provided in figure 5.21 for the mid sub-array at 400 Hz and 500 Hz using the same dataset shown in figures 5.18 through 5.20. For the 500 Hz 1/3-octave band noise map, the conventional beamformer is able to resolve the source at the hub and the source about half way out on the blade. MUSIC is applied to the same data with $L = 2$ because of the assumption that there are two sources present, one at the hub and one on the blade. The result is a very clear separation of the two sources. Note that MUSIC predicts a power of 92 dB instead of the 48-49 dB from conventional beamforming, revealing that MUSIC should only be used to determine the locations of sources and their relative strengths to some extent, not their power. A more interesting scenario is the 400 Hz 1/3-octave band noise map where conventional beamforming cannot resolve hub and blade contributions. MUSIC, on the other hand, clearly reveals the existence of the blade source. Interestingly, the noise floor for these MUSIC examples is only 3-4 dB below the peaks, but the contrast is still very apparent.

An application of Robust Adaptive Beamforming to the 400 Hz 1/3-octave band from the same dataset reveals that RABF can be nearly as effective as MUSIC but can also be used to detect power if used properly. The CSM diagonal noise injection term, ε , must be varied to find the right balance between robustness and the ability to adapt. Figure 5.22 compares RABF to the conventional beamformer for two different values of ε . Results using the ideal value of ε are presented in the last plot. Here, the two sources can clearly be resolved. Note that the peak power in the noise map is reduced from 50 dB to 45 dB however. It is likely that the blade source is approximately 45 dB and is buried in the mainlobe structure of the hub noise in the conventional plot, but since noise maps produced using RABF resulted in reduced hub noise power for this particular case, it is possible that RABF could reduce the aeroacoustic noise as

well. In fact, values of ε less than the value used in the last plot reduce the power even more. It is possible that for noise injection values that enable RABF to resolve sources that appear combined in conventional maps, useful power information cannot be obtained.

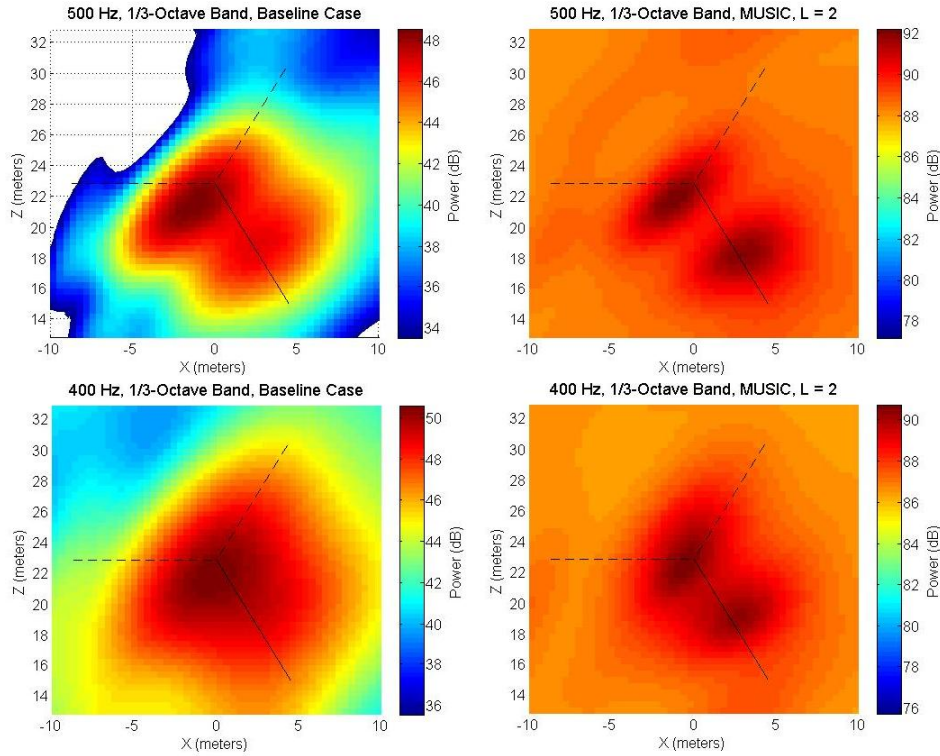


Figure 5.21: A Comparison of Conventional Beamforming (left) and MUSIC (right) Applied to a Poor Resolution Scenario

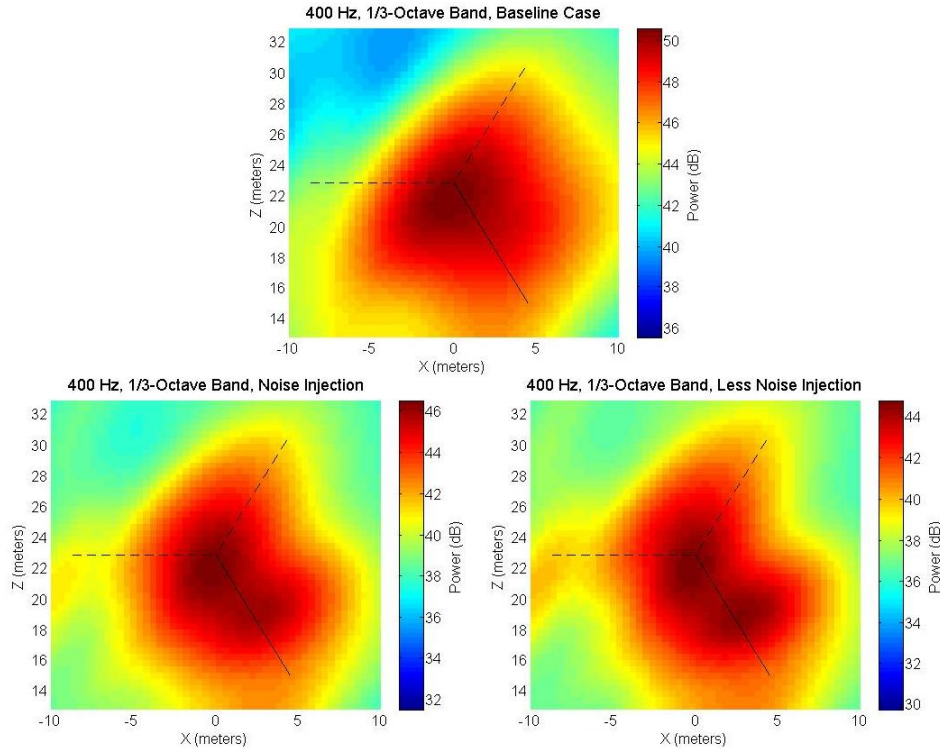


Figure 5.22: Application of Robust Adaptive Beamforming to Poor Resolution Scenario

Chapter 6

Conclusions and Future Work

The research described in this thesis includes work conducted between May 2008 and December 2009 on the design and application of an acoustic array for wind turbine aeroacoustics analysis. Currently, the theory behind beamforming and the relationship between the array shape and the array pattern are well understood. Some powerful advanced beamforming techniques have been analyzed as well and incorporated into the beamforming code. Specific challenges regarding the application of an array to the analysis of a rotating wind turbine in the field have been examined. The effects of wind noise have been thoroughly analyzed and have been shown to be negligible to beamformer performance. A brief look at the impact of atmospheric turbulence on the array performance has been taken and it has been shown that it is necessary to beamform using long periods of data, on the order of one minute, to average out atmospheric distortion. Sensor location errors have been analyzed and an upper bound on beamforming SPL error as a function of the percentage of an acoustic wavelength the sensors may be positioned from their intended locations has been derived. The effects of beamforming with imperfect knowledge of the distance from the array to the source and the wavelength being analyzed have been shown. A qualitative description of how the array pattern shifts within the scan plane with errors in these parameters was provided. Quantitative results for the specific example of the Bushland, TX array were provided to give an idea of the importance of these errors. An analysis of how Doppler shifts produced by a rotating source harm array performance was provided as well as a couple of beamformer correction techniques. In general, it was shown

that most of the sources of errors encountered when beamforming in the field increase with the size of the array, even if the product of array size and frequency analyzed remains the same. More specifically, as the solid angle formed between the source and the array increases, the effects of atmospheric turbulence, scan plane y -distance errors, wavelength errors, and Doppler shifts become more drastic. When using an array with a relatively small turbine it is sometimes necessary to design a large solid angle array to provide the necessary resolution however.

A brief description of the array hardware was provided, mostly proving that the hardware parameters work well for the array's application. The design methodology used to create the arrays for the NWTC and Bushland, TX turbines was explained. The designs yielded array shapes that could observe five octaves of acoustic signals, from 125 Hz to 8 kHz using only 32 and 45 sensors for the NWTC and Bushland tests respectively. A description of the field verification procedures for the array was given. It was found that for the central frequencies of each sub-array, using strong, tonal test sources, the array patterns closely resembled the theoretical patterns, while some sidelobe levels increased by roughly 1.5 dB. Resolution remained the same for field and simulation results however. When using an array for frequencies higher than the frequency designed for, the array pattern quality worsened, which can be expected after analyzing the theory behind beamformer errors. Some initial field tests performed in Bushland, TX during August 2009 were included. It was shown that the array is able to locate trailing edge noise near the blade tips very well. When attempting to observe low frequency inboard noise, it was found that the strong sources in the turbine nacelle interfered with blade noise. Somewhat ambiguous low frequency inboard noise plots were provided. The application of advanced "super-resolution" beamforming techniques proved able to resolve this blade noise however, and future work in this area is planned.

There are many possible areas of future work involving the array. One immediate concern is to model the effects of wind shear, or at the very least the effects of a constant wind speed, on beamforming performance. Specifically, the potential errors caused by wind altering the effective speed of sound for paths between sources and sensors need to be quantified. If the errors prove

to be significant enough, beamforming modifications to account for wind and wind shear effects need to be developed.

Beyond Robust Adaptive Beamforming and MUSIC, there are several other advanced beamforming techniques that need to be explored. A technique developed by Peter Sijtsma at NLR in The Netherlands called CLEAN-SC, or CLEAN based on spatial Source Coherence, has been proven to increase the resolution and dynamic range of the array used in Bushland [64]. CLEAN-SC is an iterative technique where the peak noise source and all sidelobes that are coherent with it are removed from the noise map, revealing the next strongest source. This process is repeated until it is likely that all significant sources have been revealed. Although slower than conventional beamforming, this technique has already allowed the identification of inboard blade sources at 500 Hz and should be explored in more depth. While CLEAN-SC is a very powerful tool, one shortcoming is its inability to resolve two sources that are within the -3 dB beamwidth of the array. The algorithm simply locates the peak of the noise map and therefore if two equally strong sources are within the classical resolution of the array, the algorithm will assume a source is located directly between the actual sources. A technique that may be more powerful is DAMAS, or a Deconvolution Approach for the Mapping of Acoustic Sources, developed by Thomas Brooks and William Humphreys at NASA Langley [65]. This computationally expensive approach is able to resolve two sources of equal strength within the classical resolution limit in simulation. With such excellent resolution, the technique may prove to be very helpful in resolving inboard blade sources from hub noise and needs to be pursued.

Much effort was made in trying to field calibrate the array microphones by broadcasting a sequence of strong tonal signals using a computer speaker and comparing the response of the array microphones to a high-quality microphone with known frequency response. These tests provided the confusing results shown in figure 4.4. A more careful experiment involving an anechoic chamber is desired. Although the system excluding the microphone has a flat frequency response and the microphones have a flat advertised frequency response it is possible that the way the microphone is positioned in the signal conditioner enclosure provides some

additional frequency shaping. A similar desired calibration procedure would be to use the array to predict the power of a strong tonal acoustic source located in the rotor plane. This power could be compared to the power detected by a high-quality calibrated microphone to determine the array's accuracy. Tests have been performed in this area, but results have shown that the array's response can differ by +/- 6 dB compared to the reference microphone, depending on frequency. It is highly likely that multipath can cause the signal received at the reference microphone to differ from the actual value, so it would be desirable to use several reference microphones to average out the received power.

Another calibration technique that is of interest is to use field sources to deduce the actual positions of the microphones in the field. Rather than trying to place the sensors with high precision and hoping for the best, a technique that can determine the actual positions using inter-sensor phase information would be more useful. One method that is described by Dougherty [47] involves the relationship between the eigenvectors of the CSM and the steering vectors. If only one strong source is present in the acoustic scene, then the correct steering vector for that location will be an eigenvector of the CSM. This vector can be compared to the steering vector that locates the peak power during beamforming to find the phase correction terms necessary for the actual array geometry.

The complete de-Doppler correction technique derived in section 3.3 has been successfully applied to simulated rotating source cases, but has not been successfully applied in the field on the rotating turbine. An acoustic source has been built that could potentially be placed near the tip of one of the blades to create a strong, tonal source. The de-Doppler technique could easily be validated by comparing the different beamforming techniques to this strong tonal rotating source. A broadband source is more difficult to test with because each microphone will experience a different Doppler shift and some frequency bins might contain more power than others, making the comparisons difficult. Hopefully this source can be attached to a blade for a short period of time to validate or correct the de-Doppler technique.

During the spring of 2010, the array will be used for further aeroacoustic observations of

the BSDS blades in Bushland, TX. More wind speed bins and different rotor yaw angles will be included in the tests. Blade modifications such as the sharpening of the trailing edge of the outboard region and the attachment of a splitter plate to the flatback inboard section are also planned. Comparisons will be made between the baseline blades and the modified blades. Hopefully acoustic shielding of the nacelle can be implemented to reduce gearbox noise and help resolve the hub and inboard blade noise. If shielding cannot be implemented, then more careful analysis of the low frequency datasets will be necessary.

Also during spring 2010, a new array design is planned. An improved data acquisition system that will allow for more channels will be purchased. An array shape consisting of 64 sensors will be designed. It is possible that the very popular multi-arm spiral array shape [29], capable of yielding low sidelobe levels, will be the array shape of choice. With only 32 channels of data acquisition, it was thought that a multi-arm spiral array shape would not simultaneously provide a large aperture and high enough sensor density. 64 channels might be enough to produce a spiral array large enough to provide good low-frequency resolution but with high enough sensor density to allow for high frequency analysis as well. Of course, the concentric ellipse design philosophy can be used with additional ellipses between the existing sensors for the Bushland array. This way each sub-array will only be used for a smaller band of frequencies and won't have to observe two octaves. Simulations will be performed to determine a better array shape for 64 sensors. Sensor hardware improvements are planned as well. For example, a system involving only one coaxial cable connected to each microphone enclosure will be designed that provides DC power and carries the AC microphone signal on the same wire. This will allow for a more robust array in the field.

Bibliography

- [1] Wagner, S., Bareiss, R., and Guidati, G., *Wind Turbine Noise*, Springer-Verlag, New York, NY, 1996.
- [2] Benson, J., Bray, W., Calderwood, B., Simons, M., and Young, A., "NREL Acoustic Array for Measurement of Wind Turbine Noise," *University of Colorado at Boulder Mechanical Engineering Final Senior Design Report*, May 2007.
- [3] Tse, I. and Bonilha, C., "Acoustic Array for Wind Turbine Noise Analysis," *Department of Energy Science Undergraduate Laboratory Internship and Math Engineering Science Achievement Internship Final Report*, Golden, CO, August, 10, 2007.
- [4] Johnson, D. H. and Dudgeon, D. G., *Array Signal Processing: Concepts and Techniques*. Prentice Hall, Englewood Cliffs, NJ, 1993.
- [5] Michel, U., "History of Acoustic Beamforming," *Berlin Beamforming Conference*, Berlin, Germany, November 21-22, 2006.
- [6] Kneipfer, R. R., "Sonar Beamforming - An Overview Of Its History and Status," NUWC-NL Technical Report 10,003, *Naval Undersea Warfare Center Detachment*, New London, CT, April 1992.
- [7] "Sound Lab Scientist and Partner Get Patent on Electronic Scanning Tube," *The New London Conn. Evening Day*, pp. 18, July 27, 1953.
- [8] Grosche, F. R., Stiewitt, H., and Binder, B., "Acoustic Wind-Tunnel Measurements with a Highly Directional Microphone," *AIAA Journal*, Vol. 15, No. 11, pp. 1590-1596, 1977.
- [9] Schlinker, R. H., "Airfoil Trailing Edge Noise Measurements with a Directional Microphone," *AIAA Paper 77-1269, 4th AIAA Aeroacoustics Conference*, Atlanta, GA, October 3-5, 1977.
- [10] Laufer, J., Kaplan, R. E., and Schlinker, R., "Experiments on Supersonic Jet Noise," *AIAA Journal*, Vol. 14, No. 4, pp. 489-497, 1976.
- [11] Soderman P. T. and Noble, S. C., "Directional Microphone Array for Acoustic Studies of Wind Tunnel Models," *Journal of Aircraft*, Vol. 12, No. 3, pp. 168-173, 1975.
- [12] Billingsley, J. and Kinns, R., "The Acoustic Telescope," *Journal of Sound and Vibration*, Vol. 48, No. 4, pp. 485-510, 1976.
- [13] Barsikow, B., King, W. F., and Pfizenmaier, III E., "Wheel/Rail Noise Generated By a Highspeed Train Investigated with a Line Array of Microphones," *Journal of Sound and Vibration*, Vol. 118, pp. 99-122, 1987.

- [14] Howell, G. P., Bradley, A. J., McCormick, M. A., and Brown, J. D., "De-dopplerization and Acoustic Imaging of Aircraft Flyover Noise Measurements," *Journal of Sound and Vibration*, Vol. 105, pp. 151-167, 1986.
- [15] Brooks, T. F., Marcolini, and Pope, D. S., "A Directional Array Approach for the Measurement of Rotor Noise Source Distributions with Controlled Spatial Resolution," *Journal of Sound and Vibration*, Vol. 112, No. 1, pp. 192-197, 1987.
- [16] Blacodon, D., Caplot, M., and Elias, G., "A Source Localization Technique for Helicopter Rotor Noise," *11th AIAA Aeroacoustics Conference*, Sunnyvale, CA, October 19-21, 1987.
- [17] Watts, M. E., Mosher, M., and Barnes, M., "The Microphone Array Phased Processing System (MAPPS)," AIAA Paper 96-1714, *2nd AIAA/CEAS Aeroacoustics Conference*, State College, PA, May 6-8, 1996.
- [18] Mosher, M., "Phased Arrays for Aeroacoustic Testing: Theoretical Development," AIAA Paper 96-1713, *2nd AIAA/CEAS Aeroacoustics Conference*, State College, PA, May 6-8, 1996.
- [19] Mosher, M., Watts, M. E., Jovic, S., and Jaeger, S. M., "Calibration of Microphone Arrays for Phased Array Processing," AIAA Paper 1997-1678, *3rd AIAA/CEAS Aeroacoustics Conference*, Atlanta, GA, May 12-14, 1997.
- [20] Humphreys, W. H., Brooks, T. F., Hunter, W. W., and Meadows, K. R., "Design and Use of Microphone Directional Arrays for Aeroacoustic Measurements," AIAA Paper 98-0471, *36th AIAA Aerospace Sciences Meeting*, Reno, NV, January 12-15, 1998.
- [21] Brooks, T. F. and Humphreys, W. M., "Effect of Directional Array Size on the Measurements of Airframe Noise Components," AIAA Paper 99-1958, *5th AIAA/CEAS Aeroacoustics Conference*, Bellevue, WA, May 10-12, 1999.
- [22] Humphreys, W. M., Shams, Q. A., Graves, S. S., Sealey, B. S., Bartram, S. M., and Comeaux, T., "Application of MEMS Microphone Array Technology to Airframe Noise Measurements," AIAA Paper 2005-3004, *11th AIAA/CEAS Aeroacoustics Conference*, Monterey, CA, May 23-25, 2005.
- [23] Underbrink, J. R. and Dougherty, R. P., "Array Design for Non-Intrusive Measurements of Noise Sources," *National Conference on Noise Control Engineering*, Seattle, WA, September - October, 1996.
- [24] Stoker, R. W. and Sen, R., "An Experimental Investigation of Airframe Noise Using a Model-Scale Boeing 777," AIAA Paper 2001-0987, *36th AIAA Aerospace Sciences Meeting*, Reno, NV, January 12-15, 1998.
- [25] Dougherty, R. P. and Stoker, R. W., "Sidelobe Suppression for Phased Array Aeroacoustic Measurements," *4th AIAA/CEAS Aeroacoustics Conference*, Toulouse, France, AIAA Paper 98-2242, June 2-4, 1998.
- [26] Sijtsma, P. and Holthusen, H., "Source Location by Phased Array Measurements in Closed Wind Tunnel Test Sections," AIAA Paper 99-1814, *5th AIAA/CEAS Aeroacoustics Conference*, Seattle, WA, May 10-12, 1999.
- [27] Michel, U., Barsikow, B., Haverich, B., and Schüttelpelz, M., "Investigation of Airframe and Jet Noise in High-Speed Flight with a Microphone Array," *3rd AIAA/CEAS Aeroacoustics Conference*, Atlanta, GA, May 12-14, 1997.
- [28] Michel, U., Barsikow, B., Helbig, J., Hellmig, M., and Schüttelpelz, M., "Flyover Noise Measurements on Landing Aircraft with a Microphone Array," *4th AIAA/CEAS Aeroacoustics Conference*, Toulouse, France, June 2-4, 1998.

- [29] Underbrink, J. R., "Aeroacoustic Phased Array Testing in Low Speed Wind Tunnels," in *Aeroacoustic Measurements*, Mueller, T. J., Ed., Springer, Berlin, 2002.
- [30] Dougherty, R. P., *Spiral-Shaped Array for Broadband Imaging*, U. S. Patent No. 5,838,284, 1989.
- [31] Élias, G., "Source Localization with a Two-Dimensional Focused Array: Optimal Signal Processing for a Cross-Shaped Array," *Inter-Noise 95*, Newport Beach, CA, July 10-12, 1995.
- [32] Gramann, R. A. and Mocio, J., "Aero-acoustic Measurements in Wind Tunnels using Conventional and Adaptive Beamforming Methods," AIAA Paper 93-4341, 15th *AIAA Aeroacoustics Conference*, Long Beach, CA, October 25-27, 1993.
- [33] Sijtsma, P. and Stoker, R. W., "Determination of Absolute Contributions of Aircraft Noise Components using Fly-Over Array Measurements," AIAA Paper 2004-2958, 10th *AIAA/CEAS Aeroacoustics Conference*, Manchester, UK, May 10-12, 2004.
- [34] "Boeing Quiet Noise Technology Initiatives," Backgrounder, *Boeing Commercial Airplanes Communications*, April 2007.
- [35] Stoker, R. W., "From Technology to the Airplane: Technology Demonstrators," *Aviation and the Environment: A Primer for North American Stakeholders*, Washington, D. C., March 19, 2008.
- [36] Sijtsma, P., Oerlemans, S., and Holthusen, H., "Location of Rotating Sources by Phased Array Measurements," *AIAA Paper 2001-2167*, 2001.
- [37] Oerlemans, S. and Migliore, P., "Aeroacoustic Wind Tunnel Tests of Wind Turbine Airfoils," *AIAA Paper 2004-3042*, 2004.
- [38] Oerlemans, S. and Méndez López, B., "Acoustic Array Measurements on a Full Scale Wind Turbine," AIAA Paper 2005-2963, 11th *AIAA/CEAS Aeroacoustics Conference*, Monterey, CA, May 23-25, 2005.
- [39] Oerlemans, S., Fisher, M., and Maeder, T., "Reduction of Wind Turbine Noise using Optimized Airfoils and Trailing-Edge Serrations," AIAA Paper 2008-2819, 14th *AIAA/CEAS Aeroacoustics Conference*, Vancouver, British Columbia, May 5-7, 2008.
- [40] Berg, D. and Barone, M., "Aerodynamic and Aeroacoustic Properties of a Flatback Airfoil (Will it Rumble or Whisper?)," *WINDPOWER 2008*, Houston, TX, June 2-4, 2008.
- [41] IEC/TC88, 61400-11 "Wind turbine generator systems-part 11: Acoustic Noise Measurement Techniques," 88/67/FDIS, *International Electrotechnical Commission (IEC)*, 1998.
- [42] Hubbard, H. H. and Shepherd, K. P., "Wind Turbine Acoustics," *NASA Technical Paper 3057 DOE/NASA/20320-77*, 1990.
- [43] Ashwill, T., "Blade Technology Innovations for Utility-Scale Turbines," *American Wind Energy Association Windpower 2006*, Pittsburg, PA, June 2006.
- [44] Lawson, M. V., "Assessment and Prediction of Wind Turbine Noise," ETSU W/13/00284/REP Flow Solutions Report 92/19, *Flow Solutions Ltd.*, Bristol, England, December, 1992.
- [45] "Silent Rotors by Acoustic Optimization," Final Report, ECN-E-08-015, *Energy Research Centre of the Netherlands ECN*, September 2007.

- [46] Arnold, D. P., "A MEMS-Based Directional Acoustic Array for Aeroacoustic Measurements," M. S. Thesis, *University of Florida*, Gainesville, FL, 2001.
- [47] Dougherty, R. P., "Beamforming in Acoustic Testing," in *Aeroacoustic Measurements*, Mueller, T. J., Ed., Springer, Berlin, 2002.
- [48] Sijtsma, P., "Experimental Techniques for Identification and Characterisation of Noise Sources," NLR-TP-2004-165, *NLR*, The Netherlands, 2004.
- [49] Hoctor, R. T. and Kassam, S. A., "The Unifying Role of the Coarray in Aperture Synthesis for Coherent and Incoherent Imaging," *Proceedings of the IEEE*, Vol. 78, No. 4, April 1990.
- [50] Cox, H., Zeskind, R. M., and Owen, M. M., "Robust Adaptive Beamforming," *IEEE Transactions on Acoustics, Speech, and Signal Processing ASSP-35* (10), pp. 1365-1367, 1987.
- [51] Schmidt, R. O., "Multiple Emitter Location and Signal Parameter Estimation," *Proceedings of the RADC Spectral Estimation Workshop*, pp. 243-258, Rome, NY, 1979.
- [52] Stark, H. and Woods, J. W., *Probability and Random Processes with Applications to Signal Processing*, 3rd Edition, Prentice Hall, Upper Saddle River, NJ, 2001.
- [53] Tatarski, V. I., *Wave Propagation in a Turbulent Medium*, Translated by R. A. Silverman, McGraw-Hill, New York, NY, 1961.
- [54] Dougherty, R. P., "Turbulent Decorrelation of Aeroacoustic Phased Arrays: Lessons from Atmospheric Science and Astronomy," AIAA Paper 2003-3200, 9th *AIAA/CEAS Aeroacoustics Conference*, Hilton Head, SC, May 12-14, 2003.
- [55] Oerlemans, S., Broersma, L., and Sijtsma, P., "Quantification of Airframe Noise using Microphone Arrays in Open and Closed Wind Tunnels," *International Journal of Aeroacoustics*, Vol. 6, No. 4, 2007.
- [56] Yardibi, T., Bahr, C., Zawodny, N. S., Liu, F., Cattafesta III, L. N., and Li, J., "Uncertainty Analysis in the Standard Delay-and-Sum Beamformer and Array Calibration," AIAA Paper 2009-3120, 15th *AIAA/CEAS Aeroacoustics Conference*, Miami, FL, May 11-13, 2009.
- [57] Kuttruff, H., *Acoustics: An Introduction*, Taylor and Francis, London, UK, 2007.
- [58] "TDMS File Format Internal Structure," Tutorial, *National Instruments Corp.*, February 2009.
- [59] "Reading TDM/TDMS Files with The MathWorks, Inc. MATLAB Software", Report, *National Instruments Corp.*, May 2007.
- [60] "Omnidirectional Back Electret Condenser Microphone Cartridge," Product Data Sheet, *Panasonic*.
- [61] "NI 9229/9239 Specifications," Product Data Sheet, *National Instruments Corp.*, March 2007.
- [62] Huskey, A., Simley, E., and Moriarty, P., "An Overview of the Acoustical Activities at the National Renewable Energy Laboratory," *157th Meeting of the Acoustical Society of America*, Portland, OR, May 18 - 22, 2009.
- [63] Simley, E., Moriarty, P., and Palo, S., "Aeroacoustic Noise Measurements of a Wind Turbine with BSDS Blades using an Acoustic Array," AIAA Paper 2010-0642, 48th *AIAA Aerospace Sciences Meeting*, Orlando, FL, January 3-7, 2010.
- [64] Sijtsma, P., "CLEAN Based on Spatial Source Coherence," AIAA Paper 2007-3436, 13th *AIAA/CEAS Aeroacoustics Conference*, Rome, Italy, May 21-23, 2007.

- [65] Brooks, T. F. and Humphreys, W. M., "A Deconvolution Approach for the Mapping of Acoustic Sources (DAMAS) Determined from Phased Microphone Arrays," AIAA Paper 2004-2954, 10th *AIAA/CEAS Aeroacoustics Conference*, Manchester, UK, May 10-12, 2004.

Appendix A

MATLAB Code

FreqBeamformerPlanar.m

```
function [ X_cor, Z_cor, receive_array1, Yk ] = FreqBeamformerPlanar(phases,
fs, err, robad, diagelim)
%%%%%%%
%phases is a matrix with row vectors containing the sampled time signals
%from the microphones

%fs is the temporal frequency of the source

%err contains the diagonal noise injection term used for Robust Adaptive
%Beamforming

%robad = 0 for conventional beamforming
%           1 for Robust Adaptive Beamforming
%           2 for MUSIC

%diagelim = 1 for diagonal elimination
%%%%%%%
%tilt is the difference between the supposed angle and actual angle of rotor
%plane (in degrees)
tilt = 0;

%rotor_protrusion is how far the rotor plane is from the yaw pivot point
%(in meters)
rotor_protrusion = 1.3;

%T is the ambient air temperature in celsius
T = 19;

%cs is the speed of sound in m/s
cs = sqrt(1.4*287.0897*(T+273.15));
```

```

%M is the number of sensors
M = 16;

%block_len is the length in samples that the fft is performed on
block_len = 2*1024;

%total_len is how many samples to average to get Yk
total_len = 6*2*24*1024;

%lower and upper frequencies of the band to be analyzed
%freqs = [fs/(2^(1/6)) fs*(2^(1/6))];
freqs = [fs fs];%

%f_samp is the sampling frequency
f_samp = 50000;

%N is the number of sources (for MUSIC)
N = 1;

%scan span x
xspan = [-15 15];

%scan distance y
ydistance = 36.4;

%scan span z
zspan = [36.4-25 36.4+5];

%num_step is the number of discrete steps to scan
num_step = 201;

%sens_array is a collection of cartesian points describing sensor locations
%sens_array = zeros(M,2);

sens_array = 5*[0 0;

%%%This is the actual prototype array%%%%%
%.11/4)*[sin((0/8)*2*pi) cos((0/8)*2*pi);
%sin((1/8)*2*pi) cos((1/8)*2*pi);
%sin((2/8)*2*pi) cos((2/8)*2*pi);
%sin((3/8)*2*pi) cos((3/8)*2*pi);
%sin((4/8)*2*pi) cos((4/8)*2*pi);
%sin((5/8)*2*pi) cos((5/8)*2*pi);
%sin((6/8)*2*pi) cos((6/8)*2*pi);
%sin((7/8)*2*pi) cos((7/8)*2*pi);]
(.11)*[sin((1/8 - 1/16)*2*pi) cos((1/8 - 1/16)*2*pi);
sin((2/8 - 1/16)*2*pi) cos((2/8 - 1/16)*2*pi);
sin((3/8 - 1/16)*2*pi) cos((3/8 - 1/16)*2*pi);
sin((4/8 - 1/16)*2*pi) cos((4/8 - 1/16)*2*pi);
sin((5/8 - 1/16)*2*pi) cos((5/8 - 1/16)*2*pi);
sin((6/8 - 1/16)*2*pi) cos((6/8 - 1/16)*2*pi);

```

```

sin((7/8 - 1/16)*2*pi) cos((7/8 - 1/16)*2*pi);
sin((0/8 - 1/16)*2*pi) cos((0/8 - 1/16)*2*pi);]
(.11*4)*[sin((0/8)*2*pi) cos((0/8)*2*pi);
sin((1/8)*2*pi) cos((1/8)*2*pi);
sin((2/8)*2*pi) cos((2/8)*2*pi);
sin((3/8)*2*pi) cos((3/8)*2*pi);
sin((4/8)*2*pi) cos((4/8)*2*pi);
sin((5/8)*2*pi) cos((5/8)*2*pi);
sin((6/8)*2*pi) cos((6/8)*2*pi);
sin((7/8)*2*pi) cos((7/8)*2*pi);]
%(.11*4*4)*[ sin((1/8 - 1/16)*2*pi) cos((1/8 - 1/16)*2*pi);
%sin((2/8 - 1/16)*2*pi) cos((2/8 - 1/16)*2*pi);
%sin((3/8 - 1/16)*2*pi) cos((3/8 - 1/16)*2*pi);
%sin((4/8 - 1/16)*2*pi) cos((4/8 - 1/16)*2*pi);
%sin((5/8 - 1/16)*2*pi) cos((5/8 - 1/16)*2*pi);
%sin((6/8 - 1/16)*2*pi) cos((6/8 - 1/16)*2*pi);
%sin((7/8 - 1/16)*2*pi) cos((7/8 - 1/16)*2*pi);
%sin((0/8 - 1/16)*2*pi) cos((0/8 - 1/16)*2*pi);]

];

%%%%% stretch y axis and rotate coordinate system%%%%%
%%%%% This steers the array toward the point of interest
%%%%% on the blade plane %%%%
sens_array(:,2) = sens_array(:,2)/sin(atan(.5*36.4/sqrt((36.4).^2 + (5.225).^2)));

for l = 1:M
r = sqrt(sens_array(l,1).^2 + sens_array(l,2).^2);
theta = atan2(sens_array(l,2), sens_array(l,1));
rotation = atan(5.225/36.4);
theta_final = theta - rotation;

sens_array(l,1) = r*cos(theta_final);
sens_array(l,2) = r*sin(theta_final);
end

%%%%z_offsets contains the relative offsets of the sensors compared to some
%%%%reference point (mic 1)

%%%%for west array 4/09
% for 9-24
z_offsets = [9 7.2 5.4 3.3 3.6 4.9 6.7 8.4 34.9 32.5 25.7 12.9 8.6 11.1 24.2 31.5];
%z_offsets = [34.9 32.5 25.7 12.9 8.6 11.1 24.2 31.5 44.9-2.9 28.1 0.4-2.9
%-0.25-(2.9+4.4+8.3+4.3+4.3) 10.9-(2.9+4.4+8.3) 13.7 35.6 51.7-2.9];% for 17-32

z_offsets = (z_offsets(1) - z_offsets)/100;%reference on 1st sensor in array

received_sig = phases(:,1:total_len);

```

```

fftarray = zeros(M,total_len/block_len,block_len);

%begin beamforming

%%%%%%%%%%%%%%%
%%%%%Frequency Domain Beamforming%%%%%
%%%%%
%%%%%first calculate the fft for all of the sensors%%%%%
num_bins = round((freqs(2)/f_samp)*block_len) - round((freqs(1)/f_samp)*block_len) + 1;

for f = 1:M
    for g = 1:(total_len/block_len)
        %%scaling factor of window factor * 2 (two sided fft) / number of samples
        fftarray(f,g,:) = (2/block_len)*fft(received_sig(f,(g-1)*block_len+1:g*block_len));
    end
end

clear received_sig;
clear phases;

if (diagelim)
mask_array = ones(M) - eye(M);
else
%keep diagonal
mask_array = ones(M);
end

receive_array = zeros(num_bins,num_step,num_step);

angles = zeros(1,M);

bins = [round((freqs(1)/f_samp)*block_len)+1:round((freqs(2)/f_samp)*block_len)+1];

for k = 1:num_bins
    %%create cross-spectral matrix%%

Yk = zeros(M);

for d = 1:(total_len/block_len)
    angles(1,:) = fftarray(:,d,bins(k));
    Yk = Yk + mask_array.*((conj(angles'))*conj(angles));
end

Yk = Yk./(total_len/block_len);

Yk_inv = inv(Yk + err*eye(M)); %%for RABF

%%%optional array shading shading
% % %      shade_vec = [.5*ones(1,8), 1*ones(1,8)];
% % %
% % %      Yk = (shade_vec'*shade_vec).*Yk;

```

```

[EVCT,EVAL] = eig(Yk, 'nobalance');

REVinv = zeros(M);

%%%% for MUSIC
for kl = 1:M-N
    REVinv = REVinv + EVCT(:,kl)*EVCT(:,kl)';
end

eks = zeros(M,num_step*num_step);

f_observe = round(bins(k)-1)*f_samp/block_len;

for i = 1:num_step%x coordinates

    for l = 1:num_step%z coordinates
        %calculate x, y, and z coordinates for supposed source position

        x_orig = (i-1)/(num_step-1)*(xspan(2) - xspan(1)) + xspan(1); %x
        y_orig = ydistance; %y
        z = (l-1)/(num_step-1)*(zspan(2) - zspan(1)) + zspan(1); %z

        %To correct for Yaw tilt in the rotor plane

        x = rotor_protrusion*sin(tilt*pi/180) + x_orig*cos(tilt*pi/180);
        y = y_orig - (rotor_protrusion - rotor_protrusion*cos(tilt*pi/180))
        + x_orig*sin(tilt*pi/180);

        %%  

        %%%%%%create the steering vector%%%%%
        ek = zeros(M,1);
        for g = 1:M%for each sensor
            %delta_d is the distance the plane wave travels between the
            %origin and the sensor under investigation, this a
            %projection of the sensor vector onto the supposed source
            %vector
            delta_d = (sqrt(x^2 + y^2 + z^2) - sqrt((x - sens_array(g,1))^2
            + (y - sens_array(g,2))^2 + (z - z_offsets(g))^2))/(cs/f_observe);
            ek(g) = exp(j*2*pi*delta_d);
        end

        eks(:,(i-1)*num_step + 1) = ek;

        wk = (Yk_inv*ek)/(ek'*Yk_inv*ek);

        if (robad == 1)
            receive_array(k,i,1) = wk'*Yk*wk;
        elseif (robad == 0)

```

```

        receive_array(k,i,l) = ek'*Yk*ek;
    elseif (robad == 2)
        receive_array(k,i,l) = inv(ek'*REVinv*ek);
    end

    end
end
end

%%%%%%%%%%%%%%%
%%%correct for negative values encountered in diagonal elimination
ixn = find(receive_array < 0);
receive_array(ixn) = .00000001;

%%%Begin Plotting

X_cor = [0:num_step-1]/(num_step-1)*(xspan(2) - xspan(1)) + xspan(1);
Z_cor = [0:num_step-1]/(num_step-1)*(zspan(2) - zspan(1)) + zspan(1);

[X,Z] = meshgrid(X_cor,Z_cor);

receive_array2 = double(zeros(1,num_step,num_step));
%%%%%%%%%%%%%%
for ik = 1:num_bins
    receive_array2(1,:,:,:) = receive_array2(1,:,:,:) + abs(receive_array(ik,:,:,:));
end
%%%%%%%%%%%%%

receive_array1 = double(zeros(num_step,num_step));
for i = 1:num_step
    for k = 1:num_step
        receive_array1(i,k) = receive_array2(1,i,k);
    end
end
receive_array1 = receive_array1';

%%%normalize to give actual power detected in terms of V^2
receive_array1 = receive_array1/(M^2);

%%%Find the peak location
loc_found = [0 0];

[max_rec1 ix_rec1] = max(receive_array1.^2);
[max_rec2 ix_rec2] = max(max(receive_array1.^2));

```

```

loc_found(1) = ix_rec1(ix_rec2);
loc_found(2) = ix_rec2;

figure
surf(X,Z,10*log10(receive_array1)-max(max(10*log10(receive_array1))));

xlabel('X (meters)');
ylabel('Z (meters)');
zlabel('Power (dB)');
title( strcat('Source at x = ', num2str(X_cor(loc_found(2))), ', y = ',
num2str(ydistance), ', z = ', num2str(Z_cor(loc_found(1))), ', along the plane of ',
num2str(ydistance), ' (meters)'));

view(0,90)

shading flat

hold

%%%Plot rotor outline
t = [0:99]/99;
x = (18/2)*cos(2*pi*t);
y = (18/2)*sin(2*pi*t) + 25;
a = 2*t - 1;
b = 2*t - 1 + 25;
c = -(2*t - 1) + 25;

plot(x,y,'k',a,b,'k',a,c,'k')

zlim([-15 0])
caxis([-15 0])

h1 = colorbar;
ylabel(h1,'Power (dB)')

hold

end

```

Appendix B

Array Sensor Locations

NWTC Array Shape

x position (meters)	y position (meters)	x position (meters)	y position (meters)
0.044 (high)	0.307 (high)	0.705 (mid, low)	4.909 (mid, low)
0.127 (high)	0.203 (high)	2.038 (mid, low)	3.250 (mid, low)
0.136 (high)	-0.020 (high)	2.178 (mid, low)	-0.313 (mid, low)
0.065 (high)	-0.231 (high)	1.042 (mid, low)	-3.693 (mid, low)
-0.044 (high)	-0.307 (high)	-0.705 (mid, low)	-4.909 (mid, low)
-0.127 (high)	-0.203 (high)	-2.038 (mid, low)	-3.250 (mid, low)
-0.136 (high)	0.020 (high)	-2.178 (mid, low)	0.313 (mid, low)
-0.065 (high)	0.231 (high)	-1.042 (mid, low)	3.693 (mid, low)
0.371 (mid, high)	1.104 (mid, high)	5.938 (low)	17.664 (low)
0.570 (mid, high)	0.398 (mid, high)	9.126 (low)	6.360 (low)
0.436 (mid, high)	-0.542 (mid, high)	6.969 (low)	-8.670 (low)
0.046 (mid, high)	-1.164 (mid, high)	0.729 (low)	-18.621 (low)
-0.371 (mid, high)	-1.104 (mid, high)	-5.938 (low)	-17.664 (low)
-0.570 (mid, high)	-0.398 (mid, high)	-9.126 (low)	-6.360 (low)
-0.436 (mid, high)	0.542 (mid, high)	-6.969 (low)	8.670 (low)
-0.046 (mid, high)	1.164 (mid, high)	-0.729 (low)	18.621 (low)

Bushland, TX Array, Low-Mid Configuration

<i>x</i> position (meters)	<i>y</i> position (meters)	<i>x</i> position (meters)	<i>y</i> position (meters)
0.233 (mid)	1.623 (mid)	-2.388 (mid)	1.037 (mid)
0.743 (mid)	0.093 (mid)	-1.601 (low, mid)	3.503 (low, mid)
0.303 (mid)	-1.284 (mid)	-1.446 (mid)	5.166 (mid)
-0.399 (mid)	-1.551 (mid)	2.819 (low)	19.638 (low)
-0.756 (mid)	-0.479 (mid)	6.544 (low)	16.807 (low)
-0.460 (mid)	1.007 (mid)	8.770 (low)	10.126 (low)
0.810 (low, mid)	5.646 (low, mid)	8.987 (low)	1.126 (low)
1.881 (mid)	4.832 (mid)	7.145 (low)	-8.133 (low)
2.521 (mid)	2.911 (mid)	3.666 (low)	-15.528 (low)
2.584 (low, mid)	0.324 (low, mid)	-0.652 (low)	-19.366 (low)
2.054 (mid)	-2.338 (mid)	-4.822 (low)	-18.768 (low)
1.054 (low, mid)	-4.464 (low, mid)	-7.886 (low)	-13.870 (low)
-0.188 (mid)	-5.568 (mid)	-9.144 (low)	-5.795 (low)
-1.386 (low, mid)	-5.396 (low, mid)	-8.307 (low)	3.608 (low)
-2.267 (mid)	-3.988 (mid)	-5.568 (low)	12.185 (low)
-2.629 (low, mid)	-1.666 (low, mid)	-1.552 (low)	17.969 (low)

Bushland, TX Array, Mid-High Configuration

x position (meters)	y position (meters)	x position (meters)	y position (meters)
0.073 (high)	0.507 (high)	-0.687 (high)	0.298 (high)
0.231 (high)	0.226 (high)	-0.460 (mid, high)	1.007 (mid, high)
0.158 (high)	-0.282 (high)	-0.128 (high)	1.485 (high)
-0.073 (high)	-0.507 (high)	0.810 (mid)	5.646 (mid)
-0.231 (high)	-0.226 (high)	1.881 (mid)	4.832 (mid)
-0.158 (high)	0.282 (high)	2.521 (mid)	2.911 (mid)
0.233 (mid, high)	1.623 (mid, high)	2.584 (mid)	0.324 (mid)
0.541 (high)	1.389 (high)	2.054 (mid)	-2.338 (mid)
0.725 (high)	0.837 (high)	1.054 (mid)	-4.464 (mid)
0.743 (mid, high)	0.093 (mid, high)	-0.188 (mid)	-5.568 (mid)
0.591 (high)	-0.672 (high)	-1.386 (mid)	-5.396 (mid)
0.303 (mid, high)	-1.284 (mid, high)	-2.267 (mid)	-3.988 (mid)
-0.054 (high)	-1.601 (high)	-2.629 (mid)	-1.666 (mid)
-0.399 (mid, high)	-1.551 (mid, high)	-2.388 (mid)	1.037 (mid)
-0.652 (high)	-1.146 (high)	-1.601 (mid)	3.503 (mid)
-0.756 (mid, high)	-0.479 (mid, high)	-1.446 (mid)	5.166 (mid)